University of Alberta

CMOS Cantilever Microresonator

By

Tiansheng Zhou

A thesis submitted to Faculty of Graduate Studies and Research in partial fulfillment of the requirements for the degree of Master of Science

Department of Electrical and Computer Engineering

Edmonton, Alberta

Spring 2000

National Library of Canada

Bibliothèque nationale du Canada

Acquisitions and Bibliographic Services

Acquisitions et services bibliographiques

395 Wellington Street
Ottawa ON K1A 0N4
Canada

395, rue Wellington
Ottawa ON K1A 0N4
Canada

Your file Votre référence

Our file Notre référence

The author has granted a non-exclusive licence allowing the National Library of Canada to reproduce, loan, distribute or sell copies of this thesis in microform, paper or electronic formats.

L'auteur a accordé une licence non exclusive permettant à la Bibliothèque nationale du Canada de reproduire, prêter, distribuer ou vendre des copies de cette thèse sous la forme de microfiche/film, de reproduction sur papier ou sur format électronique.

The author retains ownership of the copyright in this thesis. Neither the thesis nor substantial extracts from it may be printed or otherwise reproduced without the author's permission.

L'auteur conserve la propriété du droit d'auteur qui protège cette thèse. Ni la thèse ni des extraits substantiels de celle-ci ne doivent être imprimés ou autrement reproduits sans son autorisation.

0-612-60201-X

Canada

CMOS Cantilever Microresonator

ABSTRACT

A simple CMOS resonant microcantilever is designed and fabricated. Design principles and considerations about cantilever arms, releasing the structure, piezoresistive detection, bonding pads and etch opening are given. The resultant piezoresistor has very large response, requiring no signal amplification. Combinational silicon etching is proposed and developed. The silicon-doped TMAH anisotropic etching produces excellent results.

The dynamic properties of a resonant microcantilever in air, vacuum and liquids are investigated. The changes in fundamental resonant frequency and response amplitude with pressure, mass, magnetic fields, and different vicious liquids are successfully characterized. The possible applications such as liquid viscosity detection, band pass filter, and biochip mixer are demonstrated.

The effects of temperature-dependent residual stress on the device dynamic and static behavior are studied. Nonlinear ANSYS simulation results have good agreement with the experimental data. The interaction between water and the cantilever structure is also simulated, with good agreement.

ACKNOWLEDGEMENTS

I would like to express my most sincere thanks to my supervisor Dr. A.M. Robinson for facilitating, guiding and encouraging this work throughout its duration. I would also like to thank Dr. W. Allegretto and Dr. R. P. W. Lawson for their steady willingness to discuss scientific matters of all kinds.

I thank the staff of the Alberta Microelectronic Corporation, in particular Mr. Graham McKinnon, Dr. Jim Broughton, Mr. Tran Tran, Dr. Kevin Kornelsen and Mr. Lorin Mabbott for their considerable assistance and guidance. I also thank Dr. Ken Westra, Microfabrication Lab, University of Alberta, for his help.

I gratefully acknowledge the assistance and encouragement of Keith Brown, Yuan Ma, Bing Yu, Derek Strembicke and Albert Chan.

It is also my wish to acknowledge the support of the Canadian Microelectronics Corporation (CMC), without which this research could not have been accomplished.

Finally, I thank my parents and family for their patience, support and encouragement over the years. Their devotion has made this work, as all my endeavors, possible.

CONTENTS

CHAPTER 1 INTRODUCTION 1

1.1 Motivation 1

1.2 Organization 4

CHAPTER 2 THE DEVICE DESIGN 5

2.1 Introduction 5

2.2 Principles of Structure Design 6

2.3 Design of the Cantilever Arms 11

2.4 Control Structure for Post-process Release 18

2.5 Piezoresistor Design 24

2.6 Design of the Bonding Pads 27

2.7 Design of the Etching Openings to the Silicon Substrate 30

CHAPTER 3 POST-PROCESSING OF CMOS CANTILEVER 32

3.1 Introduction 32

3.1.1 Silicon anisotropic etching 33

3.1.2 Silicon isotropic etching 36

3.1.3 Silicon combinational etching 38

3.2. TMAH Anisotropic Etching 41

3.2.1 Etching method 41

3.2.2 Etching procedure 51

3.3 XeF_2 Isotropic Etch 52

CHAPTER 4 DEVICE CHARACTERIZATION

4.1 Experimental Set-up 58

4.2 Cantilever in Air 60

4.3 Cantilever in Vacuum 66

4.4 Fine Tuning of the Resonant Frequency 70
4.5 Band Pass Filter 71
4.6 Cantilever in Liquids 74
4.7 Hysteresis 77

CHAPTER 5 DEVICE MODELING 80
5.1 Cantilever Deflection Caused by Thermal Stress 80
5.2 Finite Element Model for Cantilever Device 86
5.3 The Effects of Geometry on Bending 92
5.4 The Effects of Mass on the Resonant Frequency 94
5.5 ANSYS Simulation of Band Pass Filter 96
5.6 ANSYS Simulation of DC Current Tuning of Resonant Frequency 96
5.7 ANSYS Simulation of Cantilever in Water 101

CHAPTER 6 CONCLUSIONS AND FUTURE WORK 110

REFERENCES 113

APPENDICES
Appendix A: The Preparation of the TMAH Etch Bath 124
Appendix B: Input File for Cantilever ANSYS Simulation 125

List of Tables

Table		Page
2.1	ANSYS analysis of the residual deflections for the different cantilever configurations	15
4.1	Measurement results of DC current on the resonant frequency at a pressure of 18 Torr	70
4.2	Measurement results of cantilever in liquids	76
5.1	Cantilever combinations for parameter extraction	85
5.2 (a)	Cantilever tip bending and first resonant frequency	87
5.2 (b)	Material properties of the cantilever device	87
5.3	Summary of ANSYS simulations	92
5.4	ANSYS results of mass effects on resonant frequency	96
5.5	The simulation results of band pass filter	97
5.6	Calculated and measured first resonant frequency for the cantilever in vacuum and in water	106

List of Figures

Figure *Page*

2.1 Cross section of wafer of a typical MITEL 1.5 μm CMOS micromachining fabrication 5

2.2 A cantilever device 7

2.3 Schematic diagram of a single-degree-of-freedom system acted on by an external force $F(t)$ 8

2.4 The plot of the normalized magnitude $\frac{A_0 k}{F_0}$ of the steady-state response of a damped system versus the frequency ratio for several different values of the damping ratio ζ 10

2.5 Modal analysis of the cantilever structure 11

2.6 Cross section of a supporting arm of the cantilever device 13

2.7 ANSYS analysis of the residual deflections for three different cantilever configurations 15

2.8 Anisotropic etching of <110> SiO_2 strip in 40 wt. % KOH at 80 °C 16

2.9 Anisotropic etching of SiO_2 strip parallel to <110> silicon crystal direction in 40 wt. % KOH at 80 °C 17

2.10 Sketch of crystalline planes revealed as the cantilever beam is etched and freed from the underlying crystalline silicon 19

2.11 An example of crack damage in a cantilever structure fabricated in Mitel 1.5 μm CMOS process 19

2.12 Schematic design of cantilever structure with/without connection bars 20

2.13 Device after 25 min. etching in 5 % TMAH at 85 °C 21

2.14 Flat cantilever structure after release 22

2.15 Connection bars cut by laser beam to separate two cantilevers. The cut was near the tip of the right hand cantilever 23

2.16 Connection bars cut by laser beam to separate two cantilevers. The cut was near the center of the connection bars 23

2.17 Stress distribution in the supporting arm when the cantilever is actuated 25

2.18 The optimum design location of polysilicon resistor 26

2.19 The response of polysilicon resistor when cantilever vibrates in air (without using amplifier) 27

2.20 Special design of bonding pads 29

2.21 Bonding pad of cantilever device 29

2.22 Design of opening to the silicon substrate 30

2.23 The cantilever device fabricated by the Mitel 1.5 μm process 31

3.1 Silicon anisotropic etching 34

3.2 Silicon isotropic etching 37

3.3 Combination of anisotropic etch and isotropic etch 41

3.4 Etch results of bonding pad after being etched in 5 wt. % and 25 wt. % TMAH at 85 °C for 60 minutes 42

3.5 Etched (100) surface after 20 minutes of etching in 5 wt. % TMAH with 44 g/L silicic acid doping at 80 °C 44

3.6 Schematic diagram to show the initiation of hillock formation 45

3.7 Etched (100) surface after 20 minutes etching at 80 °C in 5 wt.% TMAH with 44 g/L silicic acid and 3 g/L potassium persulfate added 46

3.8 The surface of the bonding pad before the etch 47

3.9 The protection of the bonding pad by Lepage epoxy 47

3.10 The surface of bonding pad after 15 min etching at 80 °C in 5 wt.% TMAH without silicic acid and oxidizer $K_2S_2O_8$ added 48

3.11 The surface of bonding pad after 15 min etching at 80 °C in 5 wt.% TMAH with 44g/L silicic acid and 3g/L $K_2S_2O_8$ added 49

3.12 The cantilever device after 40 min etching at 80 °C in 5 wt.% TMAH with 44 g/L silicic acid and 3 g/L $K_2S_2O_8$ added 50

3.13 The setup for 5 wt. % TMAH etch 51

3.14 Schematic drawing of XeF_2 etching system 53

3.15 Packaged cantilever device for XeF_2 etching 55

3.16 Released cantilever device by XeF_2 etching 56

3.17 The smooth etched surface 56

3.18 Connection bars cut by laser beam to separate two cantilevers. The cut was near the tip of the bottom cantilever 57

4.1 Experimental setup 59

4.2 Signal conditioning circuit 60

4.3 Frequency response of cantilever device with 200-μm-long stubs 61

4.4 Frequency response of cantilever device with no stubs 61

4.5 Frequency responses of cantilever devices with different lengths of stubs 62

4.6 Measurement set-up for the relationship between response and magnetic field 64

4.7 The frequency response of cantilever at a distance of 60 mm 64

4.8 The relationship between response and distance 65

4.9 The relationship between magnetic field and response 65

4.10 Bell jar experimental set-up 66

4.11 Frequency response of one cantilever device at pressures of 100 Torr and 300 Torr at constant actuation 67

4.12 The response versus pressure for cantilever device at constant actuation 67

4.13 The first resonant frequency versus pressure for cantilever device at constant actuation 69

4.14 The quality factor versus pressure for cantilever device at constant actuation 69

4.15 An illustration of realization of band pass filter 72

4.16 The response of the cantilever #11 under 2 mA current actuation 72

4.17 The response of the cantilever #14 under 2 mA current actuation 73

4.18 The response of cantilevers #11 and #14 in series connection under 2 mA current actuation 73

4.19 The response of cantilever #1 in DI water 75

4.20 The response of cantilever #1 in IPA 76

4.21 Response of cantilever #5 in air with 22 mA of actuation current 78

4.22 Response of cantilever #5 in air with 36 mA of actuation current 79

4.23 Response of cantilever #5 at 300 Torr pressure with 6 mA of actuation current 79

5.1 A CMOS cantilever beam 81

5.2 ANSYS finite element model for cantilever 88

5.3 ANSYS analysis of the cantilever at room temperature due to residual stress 89

5.4 ANSYS modal analysis of cantilever at room temperature (considering thermal residual stresses) 90

5.5 ANSYS modal analysis of cantilever at room temperature (without thermal residual stresses) 91

5.6 ANSYS results of mass effects on resonant frequency 95

5.7 Finite element model for band pass filter 96

5.8 The amplitude response of the filter 98

5.9 The phase response of the filter 98

5.10 ANSYS simulation results of DC current tuning of the resonant frequency in air at 18 Torr 100

5.11 Multi-lever laminating mixer 101

5.12 ANSYS finite element model for cantilever 103

5.13 ANSYS model for acoustics analysis of cantilever in water 104

5.14 Modal analyses for cantilever in vacuum and in water 105

5.15 Part of acoustics analysis model 106

5.16 Displacement of node B of the cantilever tip in water 107

5.17 Average pressure at node A in water, 76 μm from the cantilever tip 107

5.18 Average pressure distribution in water 108

5.19 Velocity distribution of water particles at a frequency of 5150 Hz 108

5.20 Displacement distribution of water particles at a frequency of 5150 Hz 109

List of Abbreviations and Symbols

$\vec{B}$	Magnetic field vector
BOE	Buffered oxide etchant
CIC	Cantilever-in-cantilever
CMC	Canadian Microelectronics Corporation
CMOS	Complementary Metal Oxide Semiconductor
DOF	Degree of freedom
DI	De-ionized water
DIP	Dual In-line Package
EDP	Ethylene diamine pyrocatechol
FEA	Finite element analysis
ξ	Damping ratio
f_0	Resonant frequency
IC	Integrated circuit
ID	Internal diameter
IPA	Isopropyl alcohol
KOH	Potassium hydroxide
$\vec{L}$	Length vector along current path
MEMS	Microelectromechanical systems
TMAH	Tetramethylammonium hydroxide
TMAHW	Tetramethylammonium hydroxide water
XeF_2	Xenon Difluoride
ZIF	Zero Insertion Force

CHAPTER 1

INTRODUCTION

1.1 Motivation

The frequency of a mechanical resonator is a highly sensitive probe for parameters that alter its potential or kinetic energy. A major class of measurement devices, termed resonant sensors, makes use of this phenomenon. Physical or chemical parameters can be sensed either by coupling loads to the resonator or by coating it with sensitive films [121]. Resonant sensors are attractive because of their high sensitivity of frequency shift. Over the past two decades, quartz mechanical resonators, quartz bulk-wave resonators, and surface acoustic wave oscillators have been investigated extensively for precision sensing applications [9,10].

Recently, silicon microfabrication technology has been enhanced with a collection of chemical etching processes for micromachining of mechanical structures. Resonant microsensors promise better reproducibility through well-controlled material properties and precise matching of micromachined structures. CMOS resonant sensors, that is, resonant sensors fabricated with CMOS technology in combination with compatible micromachining steps, have special advantages of inexpensive batch fabrication and on-chip amplifier and signal-processing circuitry, which should reduce system manufacturing cost. Different resonant sensor principles, using micromachining techniques applicable to CMOS resonant sensors have been proposed and demonstrated by MEMS researchers.

Westberg *et al.* [2] reported a CMOS resonant sensor to measure the density of fluids. The device was fabricated using a standard CMOS process followed by simple

post-processing consisting of sacrificial aluminum etching and silicon bulk micromachining.

Eyre and Pister [3] developed a magnetic field sensor fabricated in standard CMOS followed by xenon difluoride etching of the silicon substrate. The field is detected by measuring the vibration amplitude of a mechanical Lorentz-force oscillator. The oscillator consists of a current loop on a silicon dioxide plate. Amplitude is detected with a polysilicon piezoresistor Wheatstone bridge.

Ghodsian *et al.* [4] developed silicon CMOS-compatible micromachining resonant structures for mass measurement. The mass-measurement system can measure mass in the range of nanograms, in liquid and gaseous environments, using commercially available CMOS-compatible micromachining technology.

The influence of air pressure on resonating and thermoelectric microstructures was studied by Brand *et al.* [5] and Brown [74]. The resonant devices were realized with industrial CMOS technology followed by silicon etching. The influence of the air pressure on the fundamental resonance frequency and quality factor was studied.

Resonant humidity sensors using industrial CMOS-technology combined with postprocessing were reported by Boltshauser *et al.* [6]. They are based on silicon-dioxide resonators coated with thin polyimide films. The resonators are excited electrothermally with polysilicon resistors; their vibrations are detected by the piezoresistive effect of the same material. The moisture uptake of the polyimide increases linearly the mass of the resonant system and lowers its resonance frequency. A sensitivity of 270 Hz/100% RH has been obtained for a resonating beam at 16 kHz.

Baglio [7] developed resonant magnetic-field microsensors in standard CMOS technology. Different mechanical structures have been realized for the estimation of magnetic field.

Magnetically actuated CMOS-compatible CIC devices were first developed in our Micromachining Applications and Development Lab (MAD Lab) at the University of Alberta and reported in 1996 [72]. Characterization of static deflection and exploration of resonant vibration features were undertaken in 1997 [73]. The novel application of these devices as pressure sensors and humidity sensors were studied [74,121].

For all these CMOS microresonators studied before, pre-amplification of piezo-resistance was almost always needed to obtain a reasonably large output signal. The residual stress effects which change the device's static and dynamic properties were neglected by most researchers. And also, no studies were reported about the case of microcantilevers to measure liquid viscosity or to mix the samples in micro-fluidic systems.

Based on the work done in the MAD Lab [72,73,74,121], a simple resonant microcantilever is developed in this thesis. The major objectives of the thesis are to study possible applications such as liquid viscosity sensors, band pass filters and micro-fluidic mixers. Special design considerations are taken to achieve large piezoresistive output without any pre-amplification. The effects of residual stress on the device dynamic and static performances are also addressed. At the same time, the changes in fundamental resonant frequency and response amplitude with pressure, mass, and magnetic fields are characterized. In order to improve structural integrity and yield of the

microcantilever, a combinational silicon etching method, including silicon-doped TMAH anisotropic etching, is proposed and developed.

1.2 Organisation

The device design principles and considerations are given in Chapter 2. Details about designing cantilever arms, releasing the structure, piezoresistors for detecting deflection, bonding pads and etching openings are discussed.

Chapter 3 deals with post-processing of the cantilever resonators. Combinational silicon etching is proposed, and the specific details silicon-doped TMAH anisotropic etching is provided.

The dynamic properties of resonant cantilevers in air, vacuum and liquids are reported in Chapter 4. The changes in first resonant frequency with pressure, mass, magnetic field and different viscous liquids are investigated.

ANSYS, a commercial finite element software package available from Swanson Software, is used to simulate the dynamic behavior of the cantilevers and is discussed in Chapter 5. The residual stress effect is included in the simulation as a temperature loading.

Finally, conclusions and future work are described in Chapter 6.

Chapter 2

DEVICE DESIGN

2.1 Introduction

The device in this study was fabricated by the MITEL Corporation with its 1.5 μm CMOS process [111]. This process provides two metal layers (aluminum) and two polysilicon layers (see Figure 2.1). Nine square millimeters of fabrication space were sponsored by the Canadian Microelectronics Corporation (CMC). The mask layout file was submitted to the industrial foundry via CMC. Once the CMOS process was done, post-processing was conducted in-house to make a functional device.

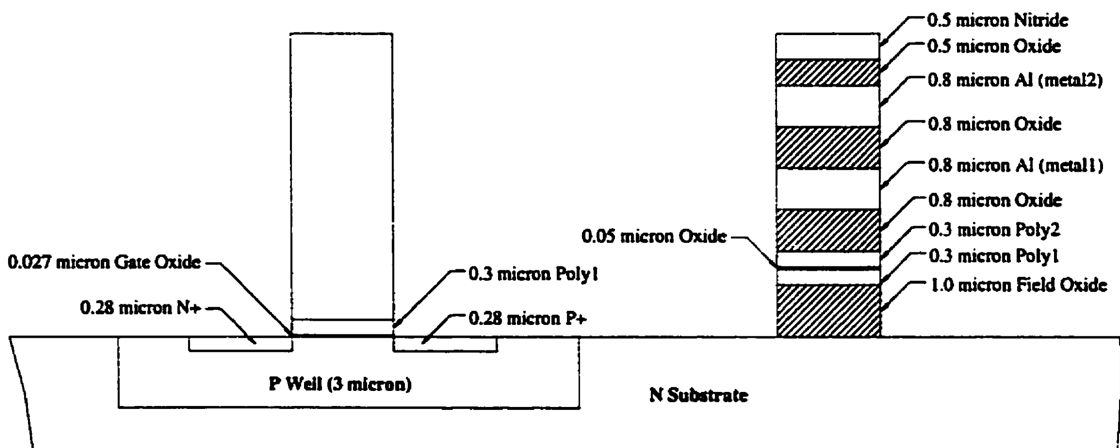

Figure 2.1 Cross section of a wafer of a typical MITEL 1.5 μm CMOS micromachining fabrication

Based on the specific features of the MITEL 1.5 μm CMOS micromachining processes, several design considerations have to be taken into account in order to obtain fully functional devices with better performance and maximum yield.

2.2 Principles of Structure Design

A mechanical structure has certain natural frequencies that present one of its very important dynamic properties. When a suitably shaped mechanical structure is vibrating in gas or liquid, its natural frequencies and corresponding parameters such as the quality factor Q and vibration amplitude will be influenced by the properties of the gas or liquid, such properties as pressure, density and viscosity, because of damping effects. For example, the low frequency damping of small vibrating objects in a motionless gas is proportional to gas viscosity and density. If the composition of a gas is fixed, that is, its density and viscosity are fixed, then the damping of a calibrated vibrator can be used to sense absolute gas pressure.

The device structure we selected was a double-armed cantilever, which combines two arms to support a cross bar at the end. It is simple in structure and easy to design. Figure 2.2 shows the shape of the cantilever. In its first resonant mode, the end exhibits a maximum displacement, which can be detected by piezoresistors located in the supporting arms. Due to the two supporting arms, the cantilever can vibrate in a longitudinal direction (up and down) while greatly suppressing torsional movement. The actuation of the device is produced by Lorentz forces arising from the interaction between an external magnetic field and the current flowing in the cantilever (see Figure 2.2). If the magnetic field B is applied in the plane of the substrate and perpendicular to the cross bar, Lorentz forces will occur on the supporting arms and cross bar. The actuation is either up or down depending on the direction of the current.

When a periodic force is applied to the cantilever, it will vibrate in the surrounding medium such as gas or liquid. If the cantilever is considered as a vibrational

system with one degree of freedom, then the linear elastic resonant theory for damped systems can be used (see Figure 2.3)

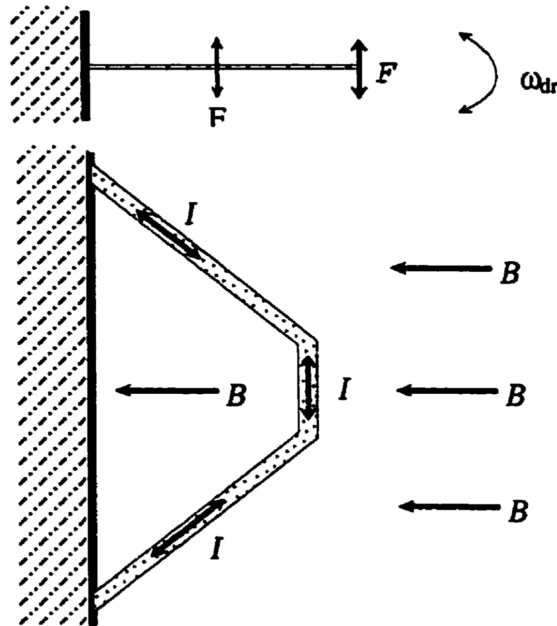

Figure 2.2 A cantilever device

The equation governing the deflection of our damped, driven harmonic oscillating system can be written as [85,113]:

$$m\ddot{x} + c\dot{x} + kx = F_0 \cos\omega_{dr} t \tag{2.1}$$

where m is the mass, k is the stiffness of the spring, c is the damping coefficient and x is the amount of device deflection out of the plane of the chip. Dividing the above equation by m yields

$$\ddot{x} + 2\zeta\omega\dot{x} + \omega^2 x = f_0 \cos\omega_{dr} t \tag{2.2}$$

where,

$$\omega=\sqrt{\frac{k}{m}},\ \zeta=\frac{c}{2m\omega}\ \text{and}\ f_0=\frac{F_0}{m}$$

The particular solution of equation (2.2) is

$$x(t)=A_0\cos(\omega_{dr}t-\Phi) \tag{2.3}$$

where the magnitude A_0 and phase Φ are:

$$A_0=\frac{f_0}{\sqrt{(\omega^2-\omega_{dr}^2)^2+(2\zeta\omega\omega_{dr})^2}} \tag{2.4}$$

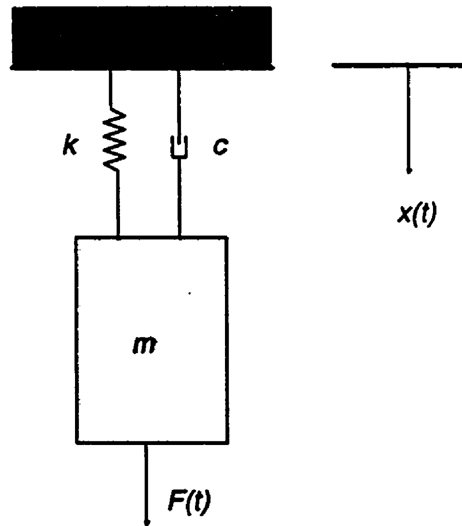

Figure 2.3 Schematic diagram of a single-degree-of-freedom system acted on by an external force $F(t)$

$$\Phi=\tan^{-1}\left(\frac{2\zeta\omega\omega_{dr}}{\omega^2-\omega_{dr}^2}\right) \tag{2.5}$$

After some manipulation, the expression for the magnitude and phase can be rewritten as:

$$\frac{A_0k}{F_0}=\frac{A_0\omega^2}{f_0}=\frac{1}{\sqrt{(1-r^2)^2+(2\zeta r)^2}} \tag{2.6}$$

$$\Phi = \tan^{-1}\frac{2\zeta r}{1-r^2} \quad (2.7)$$

where r is the frequency ratio $r = \frac{\omega_{dr}}{\omega}$, a dimensionless quantity. The plot of the normalized magnitude $\frac{A_0 k}{F_0}$ of the steady-state response of a damped system versus the frequency ratio for several different values of the damping ratio ζ is shown in Figure 2.4. The maximum value of A_0 will occur where the first derivative of $\frac{A_0 k}{F_0}$ vanishes, that is,

$$\frac{d}{dr}\left(\frac{A_0 k}{F_0}\right) = \frac{d}{dr}\{[(1-r^2)^2 + (2\zeta r)^2]^{-1/2}\} = 0 \quad (2.8)$$

Thus,

$$r_{peak} = \sqrt{1-2\zeta^2} = \frac{\omega_{dr}}{\omega} \quad (2.9)$$

That is, when

$$\omega_{dr0} = \sqrt{\frac{k}{m} - \frac{c^2}{2m^2}} \quad (2.10)$$

where, ω_{dr0} is the resonant frequency at which the deflection A_0 is maximum, with value

$$A_0 = \frac{F_0}{c}\sqrt{\frac{m}{k}} \quad (2.11)$$

Equations (2.10) and (2.3) as well as Figure 2.4 imply that the maximum deflection, quality factor and resonance frequency relate to structure mass m, structure stiffness k, external driving force F_0 and damping coefficient c.

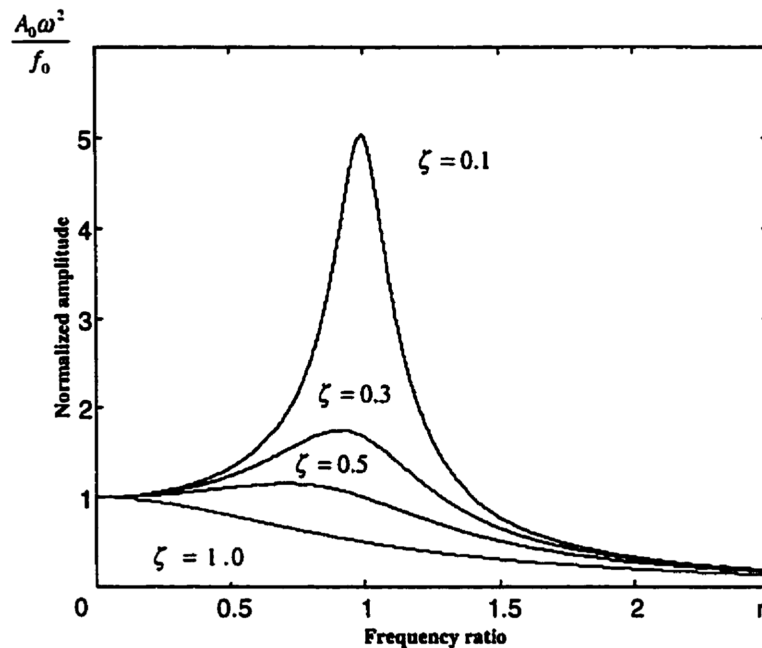

Figure 2.4 The plot of the normalized magnitude $\frac{A_0 k}{F_0}$ of the steady-state response of a damped system versus the frequency ratio for several different values of the damping ratio ζ

Based on this theory, we designed a cantilever device to measure such quantities as the viscosity of different liquids, air pressure and magnetic field strength. Considering the lower frequency (1-20 kHz) that is required to operate the device in the liquids, which more closely mimic conventional resonant viscometers [120], an FEA (finite element analysis) modal analysis was conducted during the device mask design. The modal analysis was critical at this stage because it determined the resonant frequency of the final structure. The FEA modal analysis shows that our device has the first resonant frequency of 12.665 kHz which is in the range of 1 – 20 kHz (see Figure 2.5). Figure 2.5 shows the cantilever in the positions of at rest and maximum deflection.

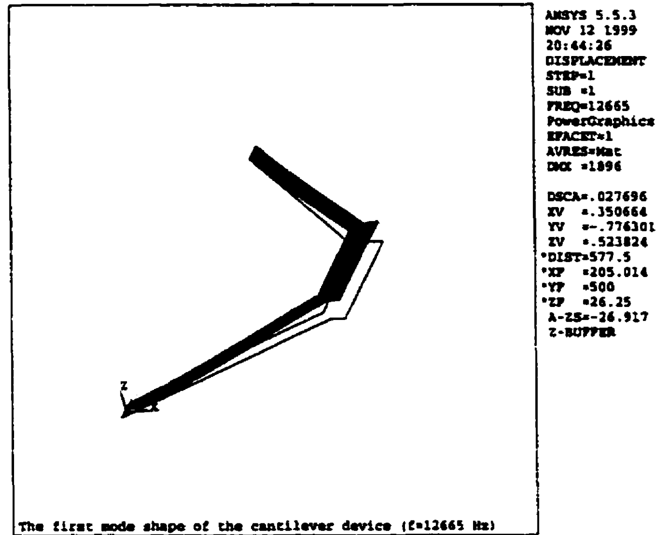

Figure 2.5 Modal analysis of the cantilever structure

2.3 Design of the Cantilever Arms

The actuation of the cantilever device is the result of the Lorentz force produced by the interaction of a time–varying current with a magnetic field. The Lorentz force is defined as:

$$\vec{F}_L = i(\vec{L} \times \vec{B}) \qquad (2.12)$$

where,

$\vec{F}_L$: the resulting force on current element of length L,

i: the time-varying electrical current in the metal loop of the cantilever,

$\vec{L}$: the length of the straight conducting element carrying current i,

$\vec{B}$: the uniform magnetic field in which $\vec{L}$ is located.

An alternating current flowing through the metal loop will cause the device to oscillate at the applied frequency. The largest oscillating movement can be achieved when the applied current has the same frequency as device's first resonant frequency.

This study is focused on the dynamic properties of the device in vacuum, air and liquid at its first resonant frequency. In the case of liquid, which presents significant damping to the cantilever, the device needs to be designed strong enough and to produce sufficient driving force in that liquid. We can provide sufficient structural strength by using almost all the layers in the MITEL 1.5 μm CMOS process. The cross section of a supporting arm of the cantilever device is shown in Figure 2.6. The test results in Chapter 3 and calculation results in Chapter 5 show the structure is sufficiently strong to vibrate in liquids such as de-ionized water and isopropyl alcohol.

The important step in the design is how to maximize the driving force based on the limited space available. We assume that an external magnet of fixed strength provides the actuation magnetic field. Then to obtain a larger driving force, we increase the effective length L of the cantilever in the magnetic field according to equation (2.12). The effective length means the length of the metal loop that can produce a driving force. Our idea is to try to make every part of the device acted on by a driving force. Based on this thinking, the supporting arm of the cantilever device was designed 45° to the fixed wall (see Figure 2.2).

There are two other reasons for designing 45° supporting arms. The first is to significantly reduce the device deflection caused by the residual stress. Residual bending of cantilever devices is often pronounced if the device is fabricated from a CMOS process. Thermal effects provide important contributions to film stress. In the CMOS

process, films and coatings prepared at elevated temperatures and then cooled to room temperature will be thermally stressed due to mismatch of their coefficients of thermal expansion. The cantilever structure with multi-layered CMOS thin films will bend upwards upon structure release because of this internal or residual stress. Severe residual bending could change the mechanical properties of the device. For example, the residual stress will change the resonant frequencies of the device for most, if not all, CMOS structures.

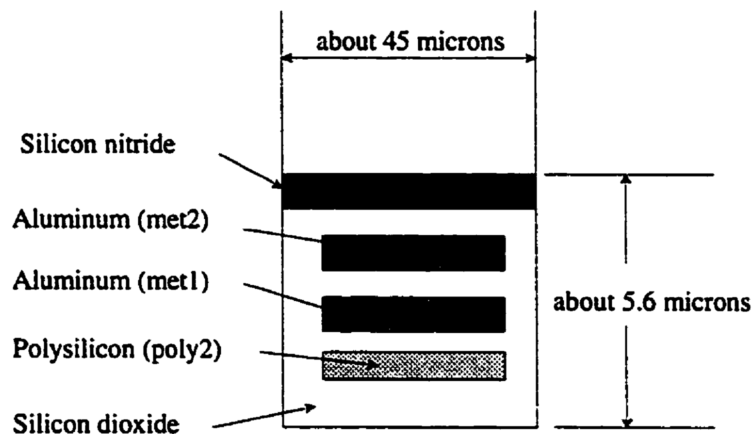

Figure 2.6 Cross section of a supporting arm of the cantilever device

In Chapter 5, we will show using ANSYS that if the arms are designed at 90° to the fixed wall, the device tip will have a larger deflection due to residual stress. Well-designed structure geometry greatly minimizes the residual deflection. Figure 2.7 shows the tip deflections of three different arm configurations. We can observe from Figure 2.7 and Table 2.1 that the device with 45° arms has smaller residual deflection than the 90° devices with equal length of or even shorter supporting arms do.

Another reason for the 45° arm design is to speed up the structure release process. The rule of the thumb for improving the etching release process is to increase

the etching selectivity. For CMOS micromachining devices, conventional etchants like KOH and TMAH have limited etching selectivity between silicon and aluminum, silicon dioxide and nitride. One solution to this problem is to reduce the etching time.

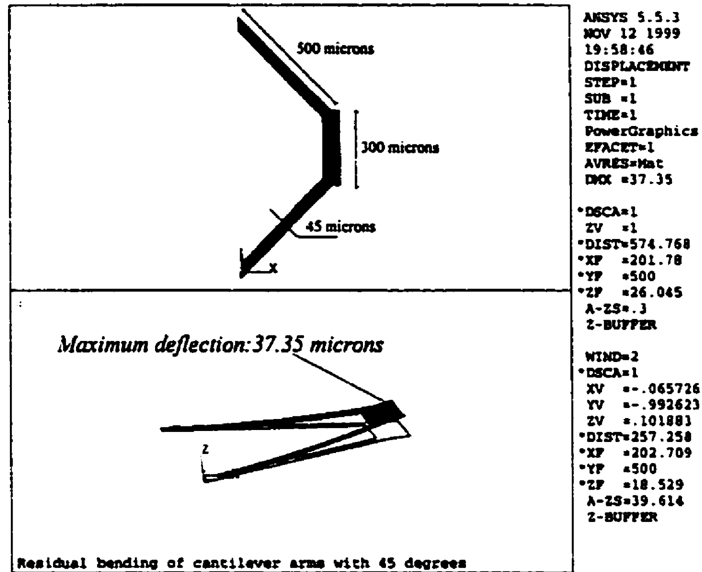

(a) The supporting arms (500 μm long) at 45°

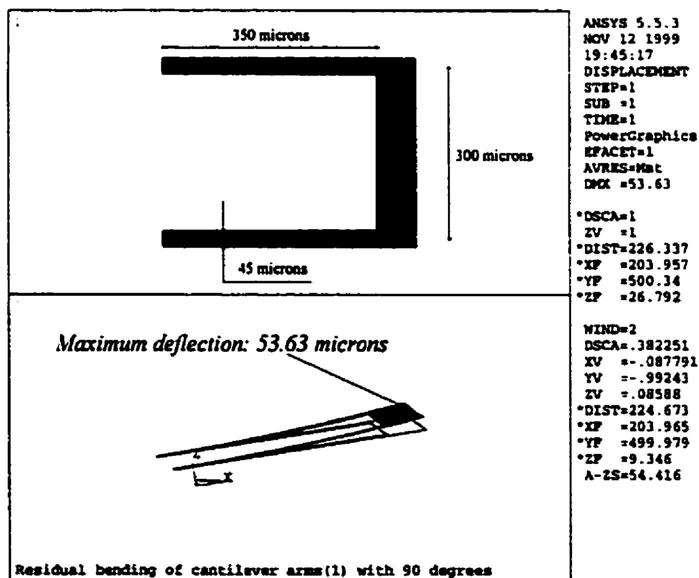

(b) Shorter (350 μm long) supporting arms at 90°

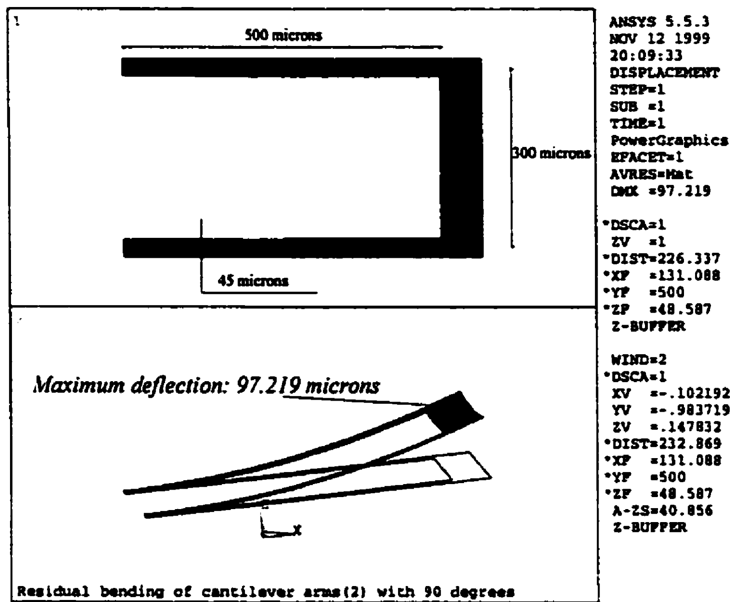

(c) Longer supporting arms (500 μm long) at 90°

Figure 2.7 ANSYS analysis of the residual deflections for three different cantilever configurations

Table 2.1 ANSYS analysis of the residual deflections for the different cantilever configurations

	Supporting arm orientation	**Length of the supporting arm (μm)**	**Length of cross bar (μm)**	**Maximum residual deflection (μm)**
Cantilever #1	45^0	500	300	37.35
Cantilever #2	90^0	350	300	53.63
Cantilever #3	90^0	500	300	97.219

Traditionally, people design the supporting arms of a cantilever parallel to the <110> silicon crystal direction for reasons of saving design space. If such a cantilever is

etched in conventional anisotropic etchants, the release procedure starts from the end of the cantilever and then moves along the arm towards the base because the etch rate of the (111) silicon crystal planes underneath the arms is very slow (see Figure 2.8). In this case, the release time depends on the length of the arm and etch rate of the (411) plane in the anisotropic etchant. We can see from Figure 2.8 that more than 50 μm etch occurs on the (411) plane while no obvious etching is observed on (111) plane.

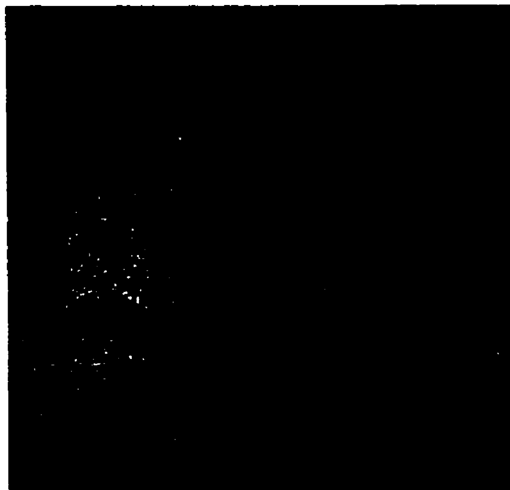

Figure 2.8 Anisotropic etching of <110> SiO_2 strip in 40 wt.% KOH at 80 °C

For our 45° cantilever arm design, the etch starts from both the cantilever tip along (411) planes and the sides of the arms along vertical (100) planes (Figure 2.9). For most etchants such as, KOH and TMAH, the etching rate of the (100) plane is faster than that of the (411) plane. For instance, the etching ratio of the (100) to the (411) plane in a 35% KOH etchant at 80 °C is about 1.45:1. Therefore, the anisotropic etching release

time for the cantilever with 45° arms depends on the width of the arm and etch rate of the (100) plane.

The device width is most often shorter than the device length, plus the etch rate of the (100) planes is faster than that of the (411) planes. It is easy to understand that the anisotropic release time should be dramatically reduced for our cantilever device since it has 500 μm-long and 45 μm-wide supporting arms orientated 45° to the <110> silicon crystal direction. If we etch our device in 35 wt. % KOH at 80 °C, the release time for a supporting arm with 45° orientation is 25 minutes while we estimate that 712 minutes will be needed for releasing the arm which is parallel to <110> silicon crystal direction.

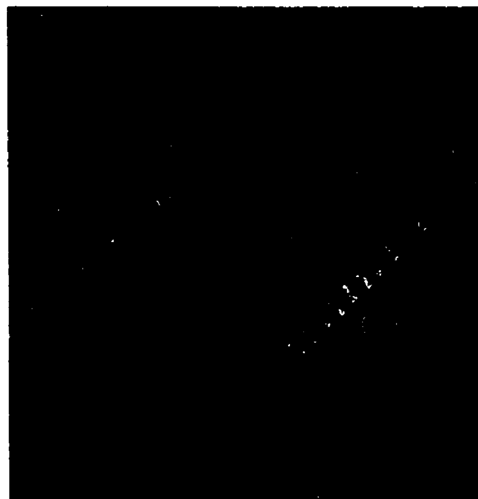

Figure 2.9 Anisotropic etching of SiO_2 strip parallel to <110> silicon crystal direction in 40 wt.% KOH at 80 °C

The (100) crystal plane cannot be seen in Figure 2.9 because the picture is a plan view. However the etching front can be clearly seen. The mechanical ripple on the released SiO_2 is caused by the residual stress.

2.4 Control Structure for Post-process Release

In a typical CMOS process, a high degree of internal (residual) stress can be developed due to the variation in thermal expansion coefficients of materials and the thermal cycling which the wafer undergoes during processing, as well as other process-induced effects. For the MEMS designer, this stress can have a significant impact on the dynamic properties of mechanical structures. In Chapter 5, we will see a certain amount of resonant frequency shift caused by this residual stress. Other examples include buckling or breaking of diaphragms and bridges, and deformation of cantilever beams [25].

Upward bending is more common with multi-layered film structures. During the release process from the substrate, the multi-layered film stress redistributes and larger stresses occur at the etch release front. The associated deformation can cause the device to fail, such as catastrophic rupture or fracture, fracture-related long-term fatigue and out-of-specification deformation [11].

During anisotropic etching of Mitel CMOS–processed chips, crystal planes (411) revealed by the etchant can form acute angles of 37°. Stress concentration at these points can exceed the critical stress for plastic deformation so that the film will crack locally to release this stress. These cracks can lead to a rupturing of the encapsulation of the polysilicon and aluminum lines. Figure 2.10 shows a sketch of crystalline planes revealed as the cantilever beam is etched and freed from the underlying crystalline silicon. Figure 2.11 shows an example of crack damage in a cantilever structure fabricated in the Mitel 1.5 μm CMOS process [111]. The cantilever tip is out of plane because of residual deflection.

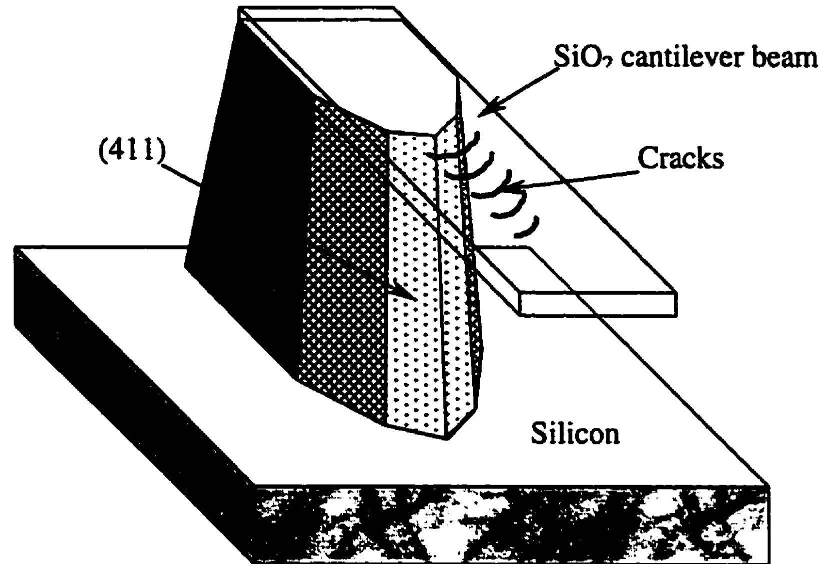

Figure 2.10 Sketch of crystalline planes revealed as the cantilever beam is etched and freed from the underlying crystalline silicon

Figure 2.11 An example of crack damage in a cantilever structure fabricated in Mitel 1.5 μm CMOS process.

In order to minimize any damage caused by the residual stress effects, the cantilever design in this study avoids placing sensing-element polysilicon lines close to

the beam center where cracks can lead to open-circuits. As well, specially designed connection bars are used to prevent deflection due to the residual stress during etching.

The device we need for our objective is presented in Figure 2.12 (a). We started with two bars, consisting of the same material as the cantilever (Figure 2.12 (b)), connected between the tips of two cantilevers in order to eliminate the residual stress effect during structure release. In addition, we wanted cantilever devices with different resonant frequencies for the realization of a band pass filter. After structure release, a laser beam was used to cut the connection bars to separate two connected cantilevers (Figure. 2.15).

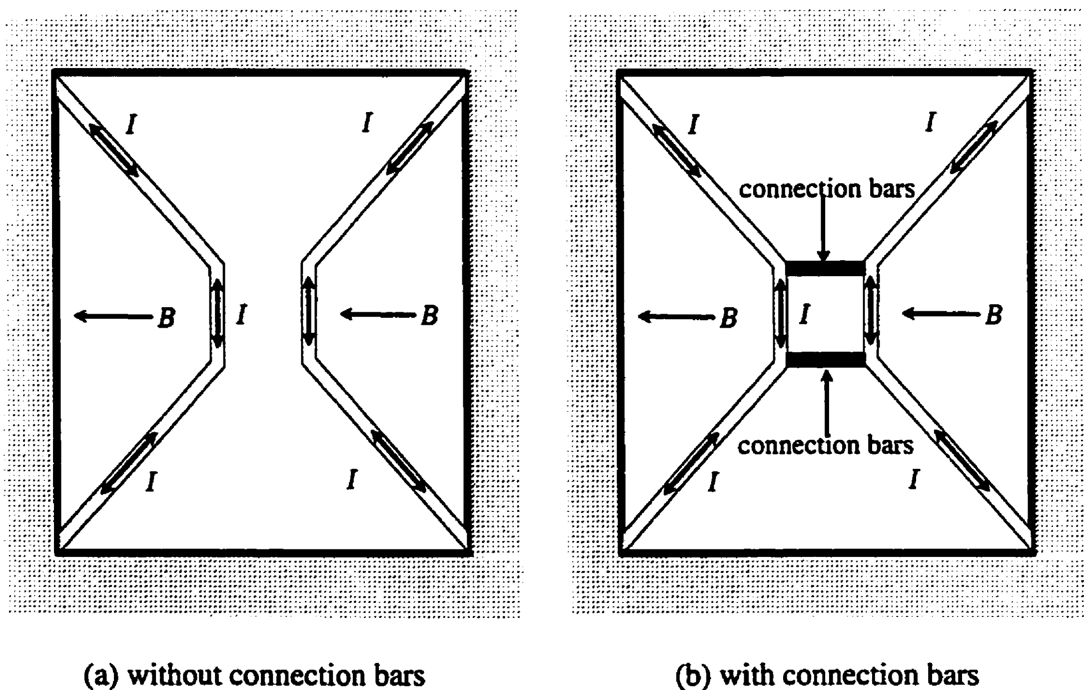

(a) without connection bars (b) with connection bars

Figure. 2.12 Schematic design of cantilever structure with/without connection bars

The connection bars not only change the geometry of the cantilever tip, but also change the etching release pattern. This etching pattern change causes longer tip etching release time. This etching time change ensures that the arm parts are always released earlier than the tip is. When we etched the device in 5% TMAH at 85 °C for 25 minutes, the supporting arms were released, but the cantilever tip was still anchored on the silicon substrate (Figure 2.13). This result was exactly what we expected. And also, the connection bars remain through all the etching process until the laser cutting process. Hence, the cantilever device does not bend upwards during etching. Stress concentration points in the arms are effectively avoided. Figure 2.14 shows the cantilever structure is flat after release because all the parts are in focus. Here we can see that the connection bars play a very important role in preventing release bending and damage.

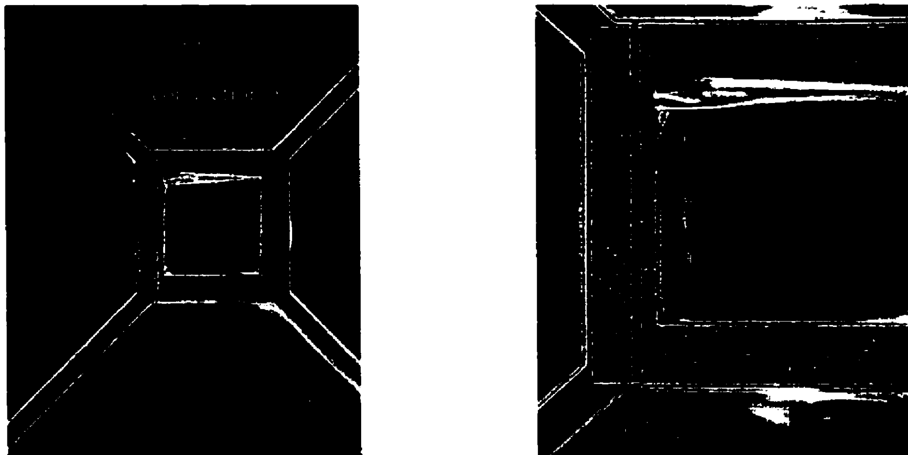

Figure 2.13 Device after 25 min. etching in 5% TMAH at 85 °C

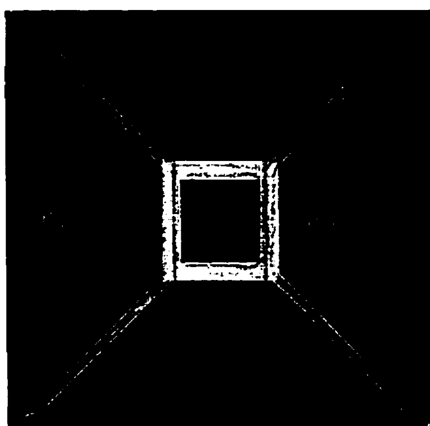

Figure 2.14 Flat cantilever structure after release

From Figure. 2.15, we can see the shining bars that were reflecting incident light from the microscope. The shining suggested a large amount of upward bending of the connection bars because of residual stress. Our measurements showed the cross bar of the cantilever had only about 35 μm upward displacement while the free end of the connection bar in Figure 2.15 had a displacement of 150 μm. These results again strongly proved the positive role of connection bars in balancing residual stress (see Table 2.1).

As mentioned earlier, one important benefit of using connection bars is that the segment of the bars remaining after laser cutting contributes to the proof mass on each cantilever. Hence, different cutting positions can change the natural frequencies of the cantilever. In this study, the first resonant frequency can shift from about 9 kHz to 13 kHz, depending on the cutting position (compare Figures 2.15 and 2.16). This crude design procedure appears to be effective for product prototyping in the research and development phase, saving time, labor and money.

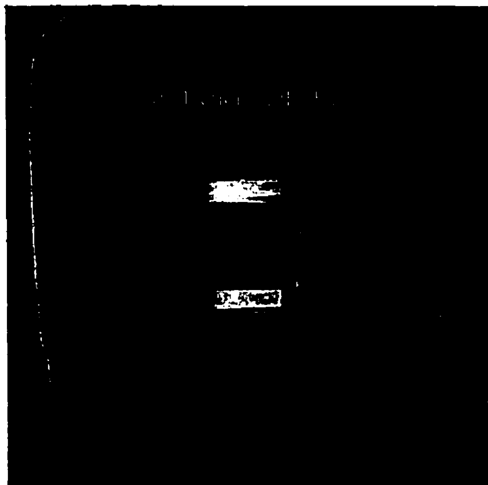

Figure. 2.15 Connection bars cut by laser beam to separate two cantilevers. The cut was near the tip of the right hand cantilever

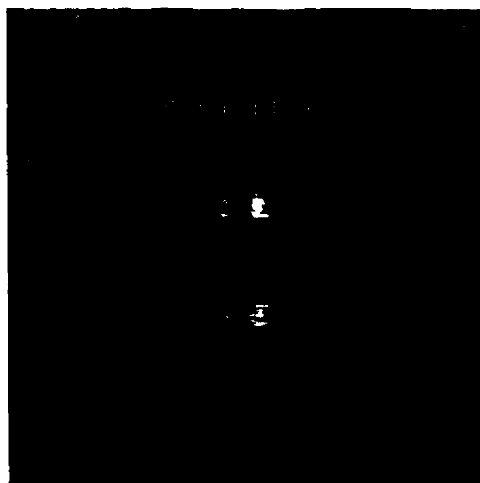

Figure 2.16 Connection bars cut by laser beam to separate two cantilevers. The cut was near the center of the connection bars

2.5 Piezoresistor Design

The placement of a segment of polysilicon within the cantilever arms will permit the measurement of cantilever deflection by measuring the resistance change of the polysilicon. Normally, a small constant current flows through the polysilicon and the voltage across it is measured. Any cantilever deflection can be detected by monitoring the voltage change. In the Mitel 1.5 μm regular process, poly1 and poly 2 are doped with phosphorous. Poly 2 has a smaller temperature coefficient of resistance. We chose poly 2 as the piezoresistor to minimize the temperature effects caused by heating due to either the constant current passed through the piezoresistor or the AC current in the cantilever structure.

The resistance change of the resistor due to small mechanical stress is expressed as [67,121]:

$$\frac{\Delta R}{R} = \pi_L \cdot \Delta\sigma_L + \pi_T \cdot \Delta\sigma_T \qquad (2.13)$$

where σ_L and σ_T are stress components parallel and perpendicular to the current flow of the piezoresistor and π_L and π_T are the longitudinal and transversal piezoresistive coefficients.

Equation (2.13) suggests that the polysilicon resistor should be placed in the location of highest stress in order to produce maximum resistance change. When the simple cantilever is actuated by an alternating current in the magnetic field, the higher stress occurs at the clamped ends and nearby (Figure 2.17). It is at these areas in which we should place the polysilicon resistor.

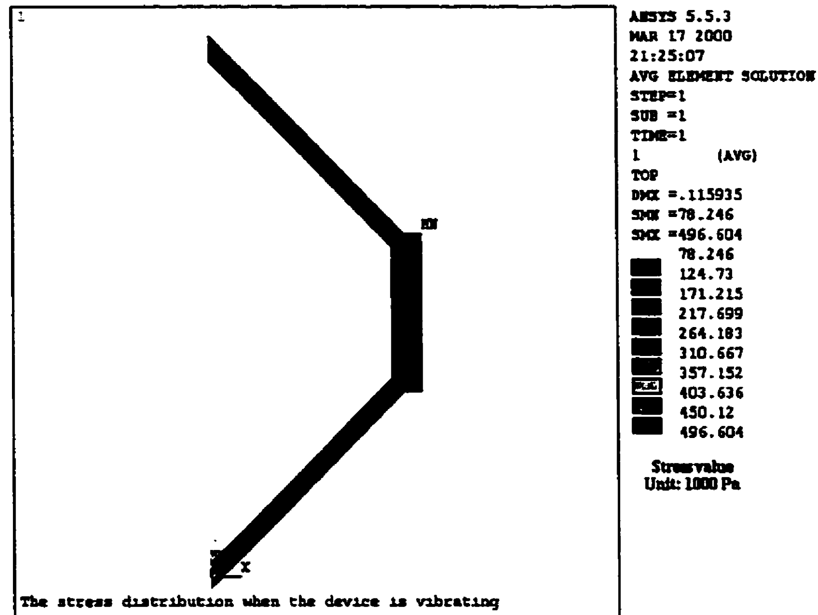

Figure 2.17 Stress distribution in the supporting arm when the cantilever is actuated

Usually, the polysilicon resistor forms a loop in the cantilever arm that is fairly narrow (Figure 2.18). That is, the dimension of piezoresistor in the direction of σ_T is very small (less than 20 μm). Accordingly, the item σ_T is approximated as zero. The resistance change is then:

$$\frac{\Delta R}{R} = \pi_L \cdot \Delta\sigma_L \tag{2.14}$$

In the case of linear and small vibration, the induced stress change $\Delta\sigma_L$ in the cantilever arms is proportional to the actuating current $I_m \cos\omega t$ that flows through the metal loop. When the polysilicon resistors are driven with a constant small DC current I_p, the voltage change ΔV across the resistor is:

$$\Delta V = \Delta R \cdot I_p = \frac{\Delta R}{R} \cdot R \cdot I_p = t \cdot \pi_L \cdot I_m \cos\omega t \cdot R \cdot I_p \tag{2.15}$$

where t is a coefficient determined by the specific CMOS process run and location of polysilicon in the arms. For the given run and polysilicon resistor design, the value of t is fixed. The higher voltage change ΔV can be achieved by increasing the currents I_p and I_m. However, increasing these currents will introduce problems of polysilicon heating effects. To avoid this problem, larger piezoresistances were designed on the arm to gain a higher voltage change ΔV.

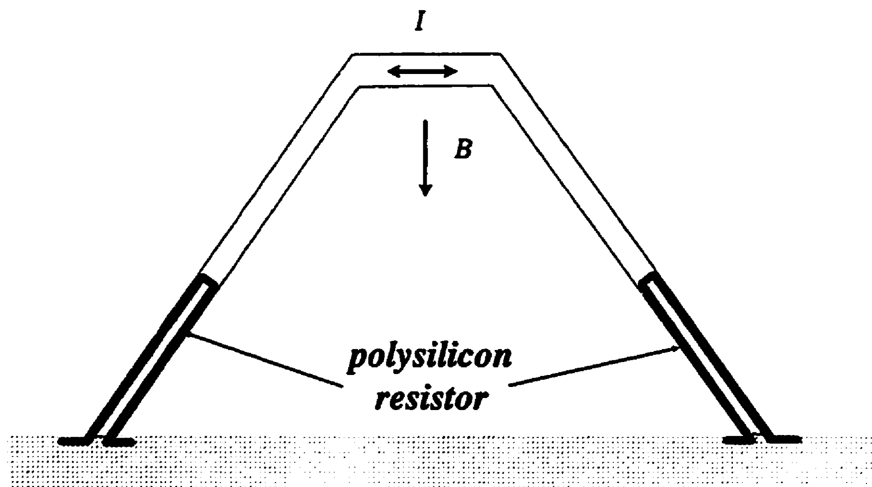

Figure 2.18 The optimum design location of polysilicon resistor

For our cantilever design, the stress caused by cantilever bending distributes over most of the cantilever arms according to the stress analysis (see Figure 2.17). This allows us to obtain larger voltage change according to equation (2.14) by designing a larger resistance R. That is, we place thin polysilicon resistors which extend along almost the entire length of supporting arms to fully take advantage of bending stress.

The measured value of the resistance of the fabricated resistor is about 9 kΩ. When the cantilever is vibrating at its resonant frequency, the measured voltage signal

from a polysilicon resistor was large enough to measure without an amplifier, as reported elsewhere [74,106,121] (see Figure 2.19).

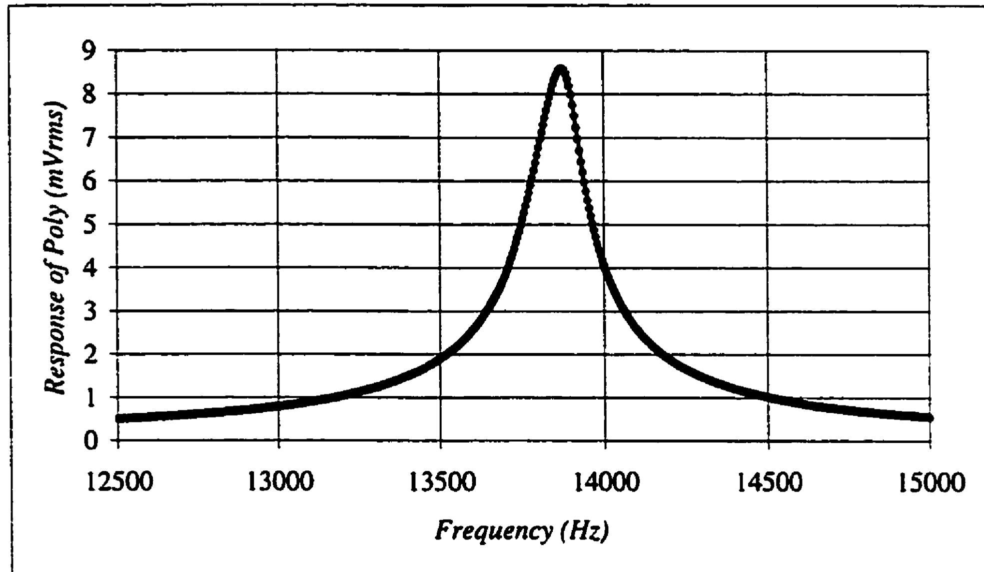

Figure. 2.19 The response of polysilicon resistor when cantilever vibrates in air (without using amplifier)

2.6 Design of the Bonding Pads

The bonding pad provides electrical connection to the cantilever device; it consists of the aluminum metal layer. Most of the standard etchants like EDP, KOH and TMAH will attack aluminum. To preserve the bonding pads, researchers have tried several approaches.

The best approach would probably be to add post-processing steps to the standard CMOS process to provide pad protection. The PAS (passivation) layer from the CMOS process is intentionally left on the pad area. After etching the device, lithography and RIE can selectively remove the PAS layer on the pad area. However, this post

process needs certain facilities that are not available to some researchers. From the viewpoint of production, it will add time and cost.

Other approaches, such as plating the bonding pads, have been successful in some cases. Electroless plating of nickel can be used to protect the bonding pads against attack from EDP [111]. First, the exposed aluminum pads should be zincated and a layer of nickel is deposited as seed layer using an electroless plating technique, and then a thicker gold layer is coated on the top of nickel layer.

We used two techniques to protect bonding pads from TMAH etching. One is to modify the TMAH solution to reduce the aluminum etching rate in TMAH. The other is to make a special design for the bonding pads.

Our bonding pads design (see Figure 2.20) is made using both the metal layers available in the CMOS process with the inter-metal dielectric isolation between. The two metal layers are electrically connected by using the VIA layer. On the bonding area, only the top aluminum is exposed. The rest of area is covered with the PAS layer. During the anisotropic etching only the top metal layer is attacked and the bottom metal layer will be protected by the dielectric.

When we used modified 5% TMAH to release the cantilever device, the top aluminum was rarely attacked. Bonding of the pad was easy using the normal operation procedure for the bonding machine.

If the top aluminum layer is totally etched in the normal 5% TMAH, the aluminum layer below the dielectric is still available for bonding. To bond to this aluminum the bonding machine has to break through the dielectric layer. Hence, a

slightly higher power and longer contact time should be applied to the bonder-tip in order to break through the dielectric layer (see Figure 2.21).

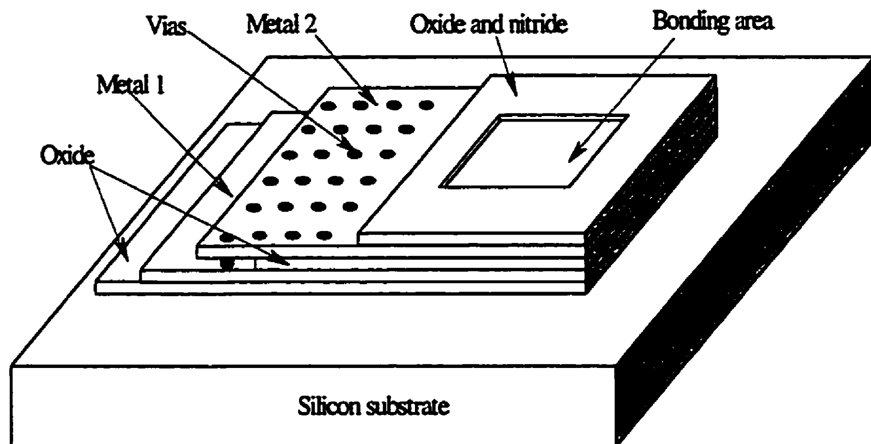

Figure 2.20 Special design of bonding pads

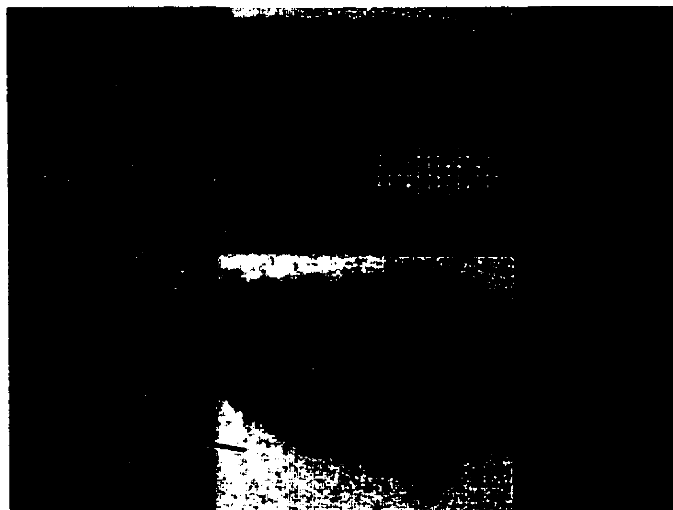

Figure 2.21 Bonding pad of cantilever device

2.7 Design of the Etching Openings to the Silicon Substrate

One CMOS MEMS layout design issue is the design of etching windows. Our past experience shows that inappropriate design of the etching window could significantly reduce the etching yield. Sometimes it can result in totally inoperable devices, due to broken metal traces from post-processing etching.

During the post-processing etching, the cantilever structure was formed by immersing the entire die in a corrosive gaseous (XeF_2) or liquid (TMAH) etchant. As a result, if materials like the polysilicon resistor or the aluminum metal lines are susceptible to attack by the etchant, and are not encapsulated in a protective layer on every side, they can be etched away and cause failed devices. For the purposes of protection from silicon etchants, the FOX (field) oxide, CON (contact) oxide, VIA (via) oxide and the PAS (passivation) overglass layer should be used.

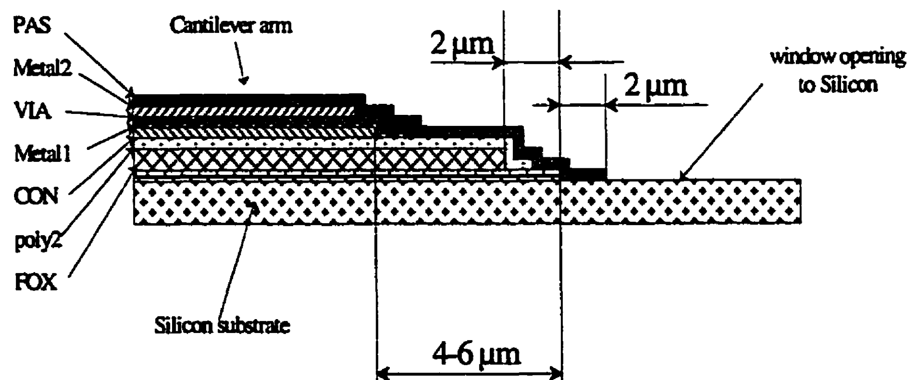

Figure 2.22 Design of opening to the silicon substrate

An opening through all layers to bare silicon is necessary in order to form an etch window for releasing the cantilever device. When multi-dielectric layers are used, an opening straight through to the silicon can result in a large step several microns high. This leads to severe coverage problems with lithography as well as PVD/CVD coating due to steep exposed layer edges at the opening. To minimize this, openings through multiple layers to the bare silicon should be staggered as shown in Figure 2.22. The final cantilever fabricated by the Mitel 1.5 μm process is showed in Figure 2.23. The stacked layers cannot be seen in the Figure 2.33 because of the dimension scale. Some small residual material on the corner areas can be seen due to the coverage problem.

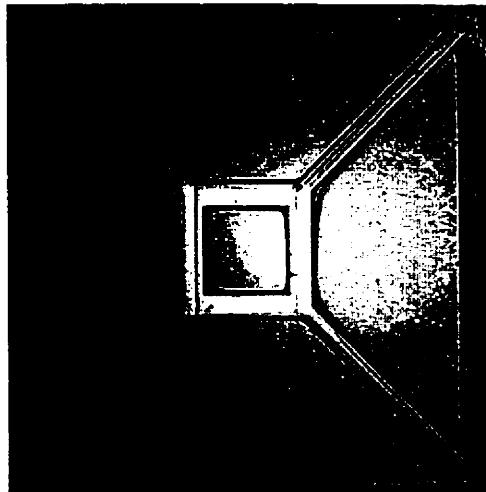

Figure 2.23 The cantilever device fabricated by the Mitel 1.5 μm process

Chapter 3

POST-PROCESSING OF A CMOS CANTILEVER

3.1 Introduction

Microelectromechanical Systems, or MEMS, are integrated micro-devices or systems combining electrical and mechanical components. Most are fabricated using integrated circuit (IC) batch processing techniques and can range in size from micrometers to millimeters. These systems can sense, control and actuate on the micro-scale, and function individually or in arrays to generate effects on the macro-scale. The significant progress made in recent years with microelectromechanical systems is due to advances in micromachining technology. Micromachining technology includes a variety of basic techniques which produces mechanical structures with very small dimensions (in the micrometer range). Generally, micromachining technology can be classified as either surface micromachining or bulk micromachining. Surface micromachining is the fabrication of micromechanical structures from deposited thin films, whereas bulk micromachining technology is typically based on single crystal silicon etching. The micromechanical structures developed with this technology are made of either silicon crystal or deposited or grown layers on the top of the substrate to fabricate micromechanical devices. Based on this point, the micromachining technique for CMOS devices is a form of bulk micromachining. The techniques for the crystal silicon etching fall into two broad categories: isotropic etching and anisotropic etching.

3.1.1 Silicon anisotropic etching

Silicon wafers are slices that have been cut from a large ingot of silicon that was grown from a single seed crystal. The silicon atoms are all arranged in a crystalline structure, so the wafer is monocrystalline silicon. When purchasing silicon wafers it is possible to specify the surface orientation to be parallel to a particular crystal plane. The silicon wafers used in standard CMOS process are <100>-oriented wafers. Anisotropic wet etching is a process of preferential directional etching of material using liquid etchants. As a consequence of anisotropy, it is possible to develop unique structures not otherwise feasible. For example, consider a <100>-oriented silicon wafer with an etched rectangular hole in a layer of silicon dioxide that covers the surface. When exposed to an anisotropic etchant this will create a truncated pyramidal shaped pit as shown in Fig 3.1. The pit is bounded by <111> crystallographic planes that exhibit a very low etch rate. The <111> planes have an inclination of 54.7°. Numerous anisotropic etchants are used for silicon, such as EDP (ethylene diamine pyrocatechol), KOH (potassium hydroxide) and TMAH (tetramethyl ammonium hydroxide).

EDP has been a widely used silicon anisotropic etchant for a number of years, although its popularity has been declining recently due to its high level of toxicity. The EDP etch is usually performed at around 110-120 °C, with an etch rate of about 1.3 μm/min in the silicon <100> direction. EDP does not attack gold, chromium, silver or tantalum and the etch rate of silicon dioxide and silicon nitride is very low compared to silicon. The main advantage of EDP is its high etch selectivity between SiO_2 and silicon, and the smoothness of the etched surface. The selectivity can be as high as 5000:1 which makes SiO_2 an ideal etch mask. The drawbacks are its toxicity and relatively low

stability. The ethylenediamine in EDP reportedly causes allergic respiratory sensitization, and pyrocathechol is described as a toxic corrosive. The material is also optically opaque, making it difficult to determining the end point of etching. It ages quickly; if the etchant reacts with oxygen, the liquid turns to a red-brown color. It needs to be replaced after just a few etches to maintain a good etch quality. It is easy to precipitate when cooled down or even during etching. All of these make the EDP etching process hard to handle.

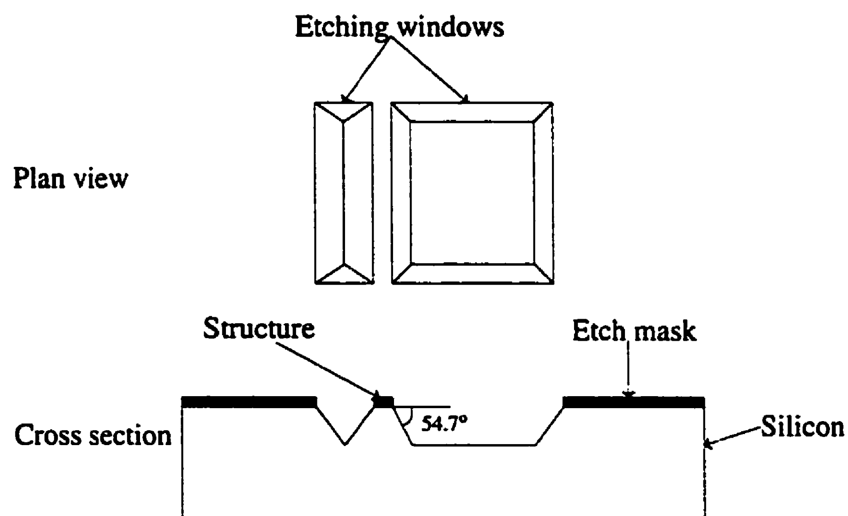

Figure 3.1 Silicon anisotropic etching

The KOH water system is simple and easy to use, and yields an etch rate of 1.0-1.2 μm/min at 80 °C with 37 wt.% concentration for the (100) plane of Si. The etch rate displays only a slight dependence of the KOH concentration in the range of 10-40 wt.%. At higher concentrations (above 35 wt. %) the KOH etch exhibits better etch uniformity and surface smoothness which can be critical for certain applications. The main

drawback with the KOH water etch system is its poor etch selectivity between Si and SiO_2, as it etches SiO_2 too fast. At 80 °C, KOH of 40 wt. % has an etch rate of as high as 35 Å/min for thermally grown SiO_2. Instead, Si_3N_4 is used as an alternative etch mask material which has virtually zero etch rate in KOH and can be grown by PECVD and LPCVD systems. Black wax like Apeizon wax can also be used as a mask layer for a KOH etchant. A KOH-etched Si (100) surface often has higher a degree of roughness compared with EDP, possibly due to the presence of the large amount of H_2 bubbles during the etch. Vigorous agitation of the etchant and addition of certain additives such as surfactant are effective in removing the H_2 bubbles absorbed on the Si surface, and significantly improve the etch surface smoothness. KOH is also incompatible with the IC fabrication process because of its metal ion K^+ contamination.

TMAH is a relatively new anisotropic Si etchant that has been used more and more by various MEMS groups. It is non-toxic, simple to use, and exhibits an excellent etch selectivity to silicon dioxide and silicon nitride. If properly prepared, it can be selective to aluminum. More importantly, TMAH is also IC compatible as it is free of alkaline metals, which is critical to fabrication of on-board electronic circuitry for various micromachined sensors. The main disadvantage of TMAH is its slower etch rate for (100) Si, and lower etch selectivity between (100) and (111) silicon surfaces. At a solution temperature of 90 °C and 22 wt% TMAH, a maximum (100) silicon etch rate of 1.0 μm/min is observed, 1.4 μm/min for (110) planes. This is slower than those observed for KOH, and its anisotropical-etching ratio between the (100) plane and the (111) plane is between 12.5 and 50. Lower concentrations give a higher etch rate. Unfortunately, the etched surface becomes extremely rough and many hillocks are formed. When the

concentration is above 20 wt. %, the etched surfaces become quite smooth. The decrease in the etching rate due to the increase in concentration can be counterbalanced by an increase in temperature. The etch rates of TMAH are comparable to those of KOH. For example, at 95 °C and 20 wt. % TMAH, the Si (100) etch rate is around 64 μm/hr. TMAH solutions do not decompose at temperatures below 130 °C, they are non-toxic and can be handled easily. Tabata [20] also studied the etching characteristics of pH-controlled TMAH. To obtain a low aluminum etch rate of 0.01 μm/min, pH values below 12 for 22 wt.% TMAHW were required. At those pH values the Si (100) etching rate is 0.7 μm/min.

3.1.2 Silicon isotropic etching

With an isotropic etching process, the etch rate is identical in every direction and does not depend on the crystal plane orientation of a silicon wafer. As a result of such an etch characteristic, the etched feature size will grow with the etch depth (Figure.3.2). The final etched feature width is determined by etching rate of mask material, ability of etchant replenishment with the presence of the etch mask overhang, agitation style and temperature. HNA and XeF_2 are two silicon isotropic etchants.

For isotropic etching of silicon, the most commonly used etchant is HNA, which is a mixture of nitric acid (HNO_3) and hydrofluoric acid (HF). Water can be used as a diluent, but acetic acid (CH_3COOH) is preferred because it prevents the dissociation of the nitric acid better and so preserves the oxidizing power of HNO_3. There are several problems associated with HNA isotropic etching of Si. First, it is difficult to mask with high precision using a desirable and simple mask such as SiO_2. Chromium and gold have

to be used as an etch mask for deep etches. Second, the etch rate is very sensitive to agitation and temperature. This makes it difficult to control lateral as well as vertical geometries. In order to obtain a smoother etched surface, the HNA etchant should have low HF and high HNO_3 concentration. An etch rate of a few microns per minute at room temperature is usually convenient for process control and efficiency. For example, an HNA ($HF:HNO_3:CH_3COOH$) system with a volume mixing ratio of 8:74:16 yields a silicon etch rate of 5 µm/min with a smooth surface. Such an etch system is ideally suited for relatively simple structures.

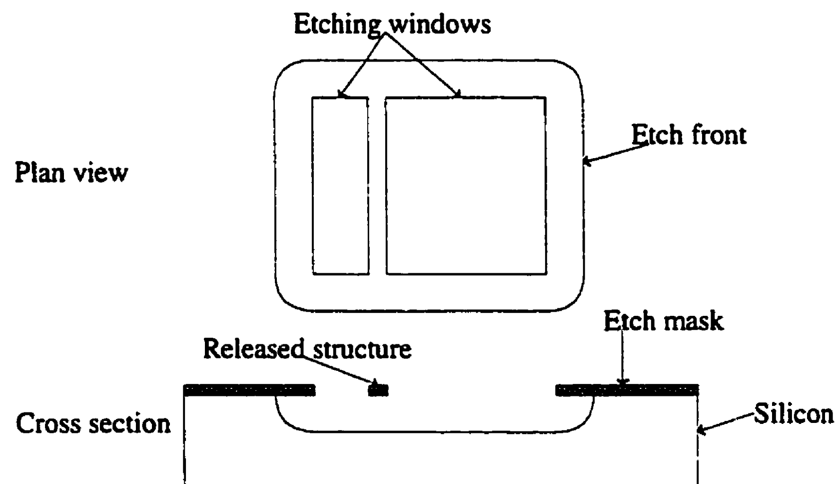

Figure 3.2 Silicon isotropic etching

A new silicon isotropic etchant, xenon difluoride (XeF_2), has come into use very recently [109,110,115]. It is a white solid at room temperature and pressure. At room temperature, XeF_2 has a sublimation pressure of about 4 Torr. Xenon difluoride vapor is an isotropic silicon etchant with extremely high selectivity to many materials commonly

used in microelectromechanical systems, including photoresists, aluminum, silicon dioxide and silicon nitride, making it easy to integrate with other processes, such as CMOS. Being a vapor phase etchant, XeF_2 avoids many of the problems associated with wet processes such as stiction. This etchant has been used as a post-CMOS etchant in place of EDP or TMAH. The gas will form HF in the presence of water vapor, which is a safety hazard, as well as being SiO2 etchant. The etch rate, profile and roughness are strongly related to the sizes of etching windows, etch pressure and duration.

3.1.3. Silicon combinational etching

Most often, standard IC process steps are combined with special micromachining steps, for example, anisotropic or isotropic silicon etching, which are compatible with the standard industrial CMOS processes.

In the past several years, our laboratory has used EDP, TMAH and XeF_2 to release mechanical structures on CMOS chips isotropically or anisotropically. We found that each etchant has specific drawbacks for certain device designs. For example, the anisotropic etchant TMAH does not have very good selectivity for etching CMOS chips; it attacks silicon dioxide and aluminum. Therefore, a long etching time often causes failed devices with broken SiO_2 structures and etched aluminum pads.

For the isotropic etchant XeF_2, we found undercutting is a big issue. Large mask overhang caused by undercutting severely changes the mechanical properties of the MEMS device. This is especially true for some bigger devices which need a longer etching time.

In this chapter, we propose a new post-processing technique which combines anisotropic and isotropic etching. In reference [26], Tea *et al.* proposed a similar method, but they used a different process procedure to release a stationary device. From the discussion in the previous section, we know that an anisotropic etchant like TMAH has very good geometry control, but is poor in etching selectivity; an isotropic etchant like XeF_2 has excellent etching selectivity, but is lacking in geometry control. By using combinational etching, each etchant is used to compensate the drawbacks of the other. This combinational etching technique is illustrated in Figure 3.3. The resulting device has much smaller undercut compared with XeF_2 etching only. First, an anisotropic etch forms pits with well-controlled boundaries with a certain etch depth. Then, an isotropic etching undercuts the etching masks to release all the structure in a shorter time. In this way, the total etching time is significantly reduced, especially for larger microstructures. With this combinational etching process, the layout design for CMOS MEMS device is becoming more flexible because the releasing etching is short and isotropic.

The etchants chosen for the cantilever device are TMAH and XeF_2. We picked TMAH out of the many strong bases because it is less toxic than the other ones, and once it is doped with silicon, it does not attack aluminum. In the next section appreciably, we will discuss how to modify the TMAH solution to reduce its aluminum etch rate.

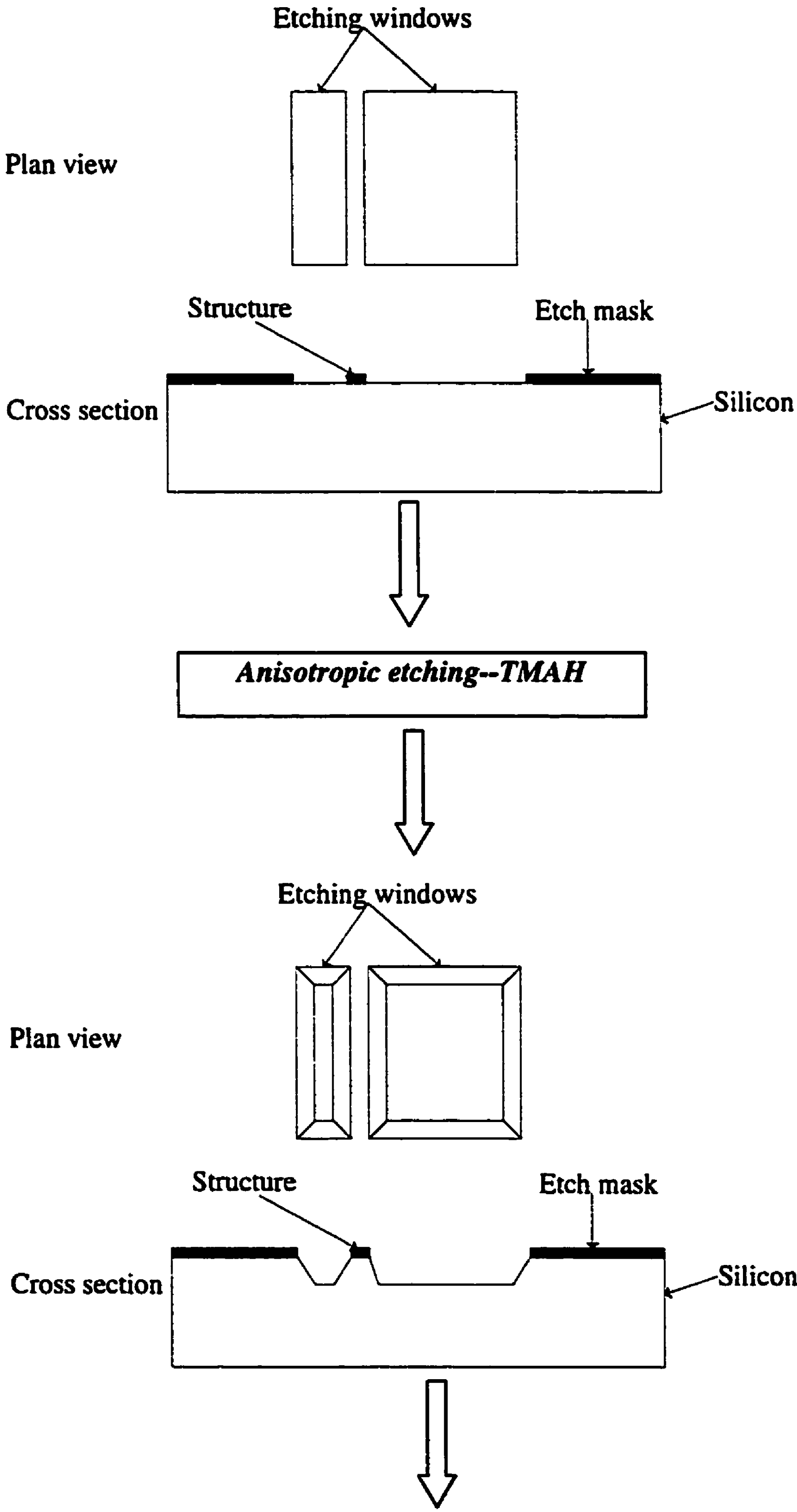

The die from CMOS process
Etching windows
Plan view
Structure
Etch mask
Cross section
Silicon
Anisotropic etching--TMAH
Etching windows
Plan view
Structure
Etch mask
Cross section
Silicon

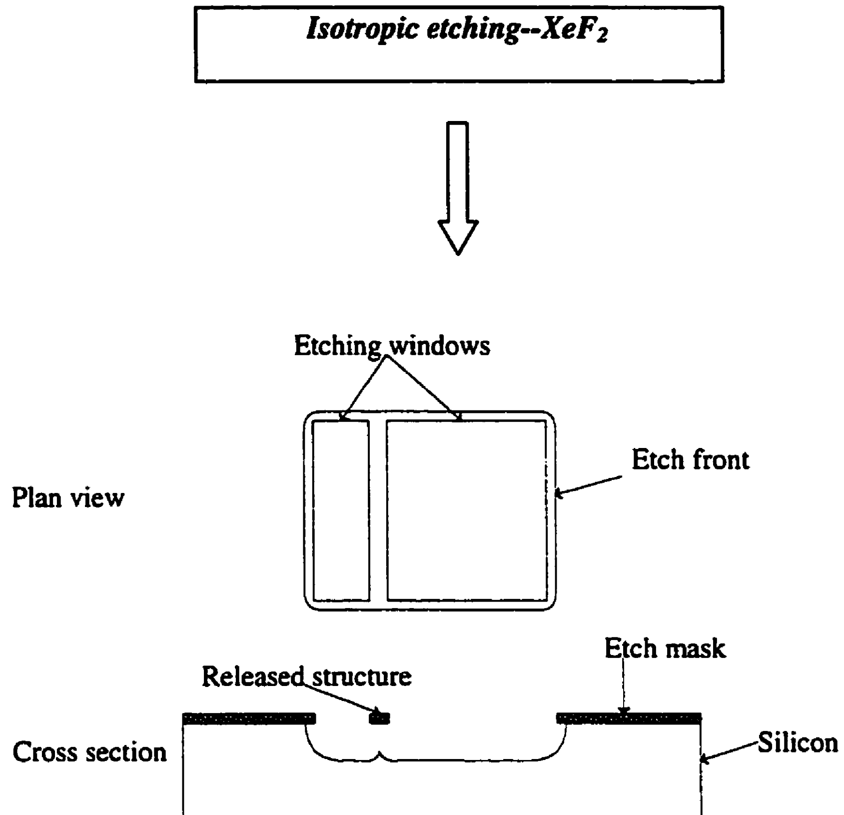

Figure 3.3 Combination of anisotropic etch and isotropic etch

3.2 TMAH Anisotropic Etching

3.2.1 Etching method

TMAH is a strong base, originally one of the photoresist developers in the semiconductor industry. TMAH can be purchased as a ready-to-use solution. Usually 25 wt. % solution is used for silicon etching. Its etch rates of the (100) silicon crystal plane, silicon dioxide and silicon nitride decrease with increasing concentration. One

significant problem with the TMAH is that aluminum pads are etched by TMAH making electrical connection impossible. Figure 3.4 shows the damaged bonding pad after being etched in 5 wt. % and 25 wt. % TMAH at 85 °C for 60 minutes. There is no aluminum left on the bonding pads, which makes the wiring bonding impossible.

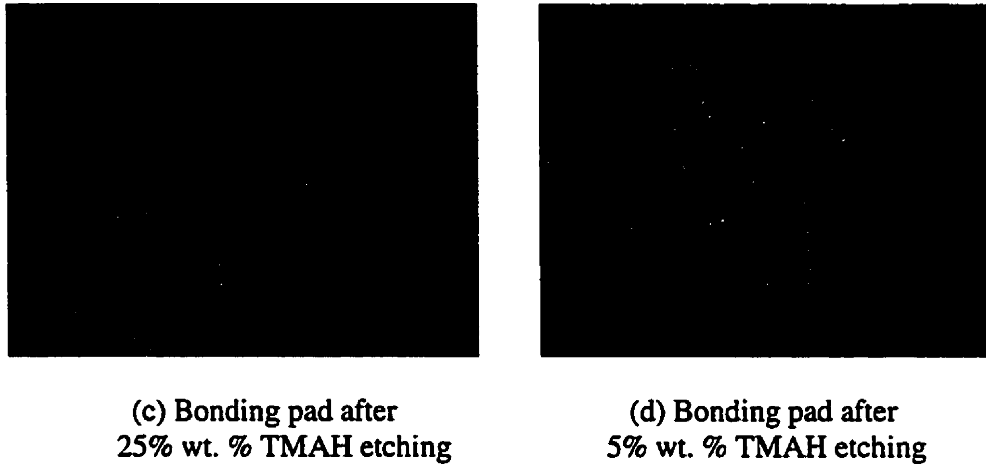

(c) Bonding pad after 25% wt. % TMAH etching

(d) Bonding pad after 5% wt. % TMAH etching

Figure 3.4. Etch results of bonding pad after being etched in 5 wt.% and 25 wt. % TMAH at 85 °C for 60 minutes

Recently, studies of the etching properties of TMAH [19,20,22,23,26,48,68,118], reported that the exposed aluminum pad can be protected from etching in TMAH by doping the solution with appropriate amounts of silicon in solutions with moderate pH. The dissolved silicon passivates aluminum bonding pads by forming a relatively insoluble layer of silicates. At the same time, the added silicon or other materials like $(NH_4)_2CO_3$ and $(NH_4)HPO_4$ lowers the pH value for the solution. The etching rates of Si and aluminum and the etched surface roughness are found to be related to the pH value. From our experiments, we found the pH value of aluminum passivation is 12.5 to 13 for

our CMOS cantilever etching. In reference [20], pH values below 12 for 22 wt. % TMAH and 11.5 for 10 wt. % TMAH were suggested for aluminum passivation.

A variety of materials can be used to dope the TMAH solution. Crushed silicon wafer is one silicon doping source. Crushed silicon wafers are pure, but complete dissolution of 60 grams silicon in 2 liters of 25 wt.% TMAH can take up to 2.5 days because of the large size of silicon and low etching rate. In our etching tests, we chose 5 wt.% TMAH as etchant to reduce this long doping time. Powdered silicon with much smaller particle size dissolves more rapidly than crushed silicon wafers. If the powdered silicon is dissolved at a higher temperature, (80 °C-95 °C), corresponding to a higher etch rate, the large amount of H_2 bubbling due to the etching reaction can cause the solution to foam over. Thus doping with powdered silicon can only be carried out at a lower temperature (45 °C). We found that the solution doped with powdered silicon is opaque and full of small particles. It did not display the expected etching properties, namely passivating the aluminum pads. This unwanted result may be caused by the purity of our powdered silicon.

Since dissolved silicon reacts to form silicic acid and various silicates in solution, some [118,26] have tried adding silicic acid directly to TMAH to provide the aluminum passivation. The passivation of 5 wt. % TMAH required 40 g/L of silicic acid. The silicon etch rate at 85 °C drops from about 1 μm/min for undoped 5 wt.% TMAH to under 0.1 μm/min with the required amount of silicic acid.

However, there is a roughness problem with the lower concentration TMAH solutions. Hillocks are usually reported as being pyramidal or near-pyramidal protrusions from the {100} surfaces, bounded by convex edges, and {111} or near-

{111} planes [22]. Figure 3.5 shows the etched (100) surface after 20 minutes of etching in silicic-acid-doped 5 wt.% TMAH at 80 °C. Our test results showed that the etch rate of the (100) plane is virtually zero once the (100) etched surface was covered with these hillocks [70].

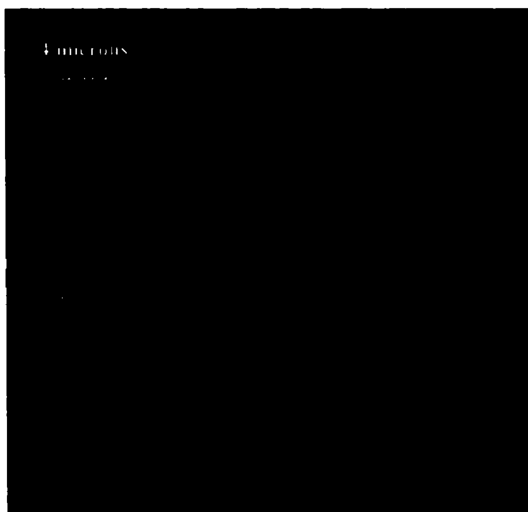

Figure 3.5 Etched (100) surface after 20 minutes of etching in 5 wt.% TMAH with 44 g/L silicic acid doping at 80 °C

The cause of the hillocks is believed to be a result of the surface attachment of hydrogen bubbles produced during the dissolution reaction (see Figure 3.6) and deposition of insoluble material [22]. Campbell's [70] work show that when the H_2 was reduced or eliminated by etching in the presence of oxygen at high pressure, smooth and pyramid-free surfaces were produced. It was proposed that the increase in the quality of the surface finish was a consequence of direct reaction of oxygen with the hydrogen produced.

Therefore, oxidizers can be added to 5 wt.% TMAH to eliminate hillocks. When a suitable amount of oxidizer is added to the TMAH solution, the hillocks are almost

eliminated and the etch rate of the (100) plane is increased, depending on the oxidizer added. Basically, any chemical that oxidizes silicon more strongly than water, does not produce gaseous reaction by-products or insoluble compounds, or excessively lowers the pH of the solution, would function as a useful additive.

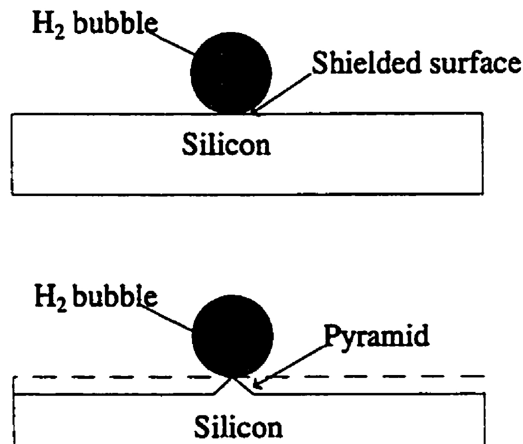

Figure 3.6 Schematic diagram to show the initiation of hillock formation

We chose persulfate $K_2S_2O_8$ (potassium persulfate) as the oxidizer for the etch of CMOS cantilever devices. Potassium persulfate is one of the strongest known oxidizers and has a white crystalline form with 99.99% purity (Aldrich Chemical). $K_2S_2O_8$ effectively eliminates hydrogen gas evolution in TMAH since only aqueous products are formed in the oxidation and dissolution reactions. When 3 g/L potassium persulfate was added to 5 wt.% TMAH with 44 g/L silicic acid doping, the etch rate of (100) at 80 °C is about 0.9 μm/min. There was no visible gas formation on the exposed silicon, and the etched (100) surface is fairly smooth (see Figure 3.7).

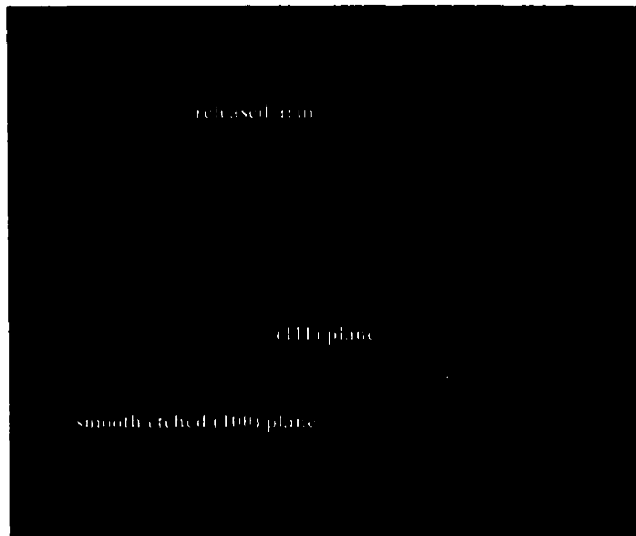

Figure 3.7 Etched (100) surface after 20 minutes etching at 80 °C in 5 wt.% TMAH with 44 g/L silicic acid and 3 g/L potassium persulfate added

The silicic-acid-doped 5 wt.% TMAH with addition of potassium persulfate passivated the aluminum. We conducted bonding and epoxy tests for the evaluation of the aluminum protection in this modified TMAH solution. The bonding test consists of a wire bond to check how easily the pad can be bonded. For the epoxy test, we etched a partially epoxy-covered bond pad for 15 minutes, and then inspect the surface difference between the covered and uncovered area. If the epoxy is very thin, the surface of the bonding pad can be clearly seen through the epoxy layer under a microscope. We used Lepage epoxy for our test. Figure 3.8 shows the surface of the bonding pad before the etch. Figure 3.9 shows the protection of the bonding pad by the epoxy.

Figure 3.8 The surface of the bonding pad before the etch

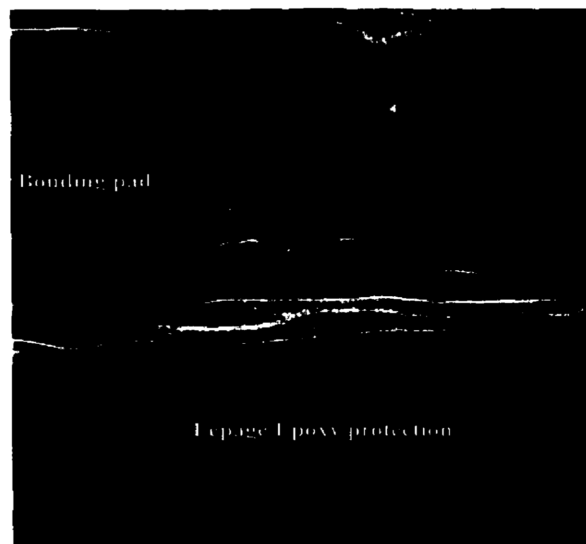

Figure 3.9 The protection of the bonding pad by Lepage epoxy

Figure 3.10 shows the surface of the bonding pad after 15 min of etching at 80 °C in 5 wt.% TMAH without silicic acid and $K_2S_2O_8$. We can see that the unprotected area was attacked by the TMAH. The top aluminum layer was removed by TMAH in the

unprotected area, which makes wire bonding difficult there. Figure 3.11 shows the surface of the bonding pad after 15 min etching at 80 °C in 5 wt.% TMAH with 44 g/L silicic acid and 3 g/L $K_2S_2O_8$. There is not any difference in the appearance of the unprotected and protected areas of the bonding pad. The wire bonding is also as easy on the uncovered area of the pad as the covered area.

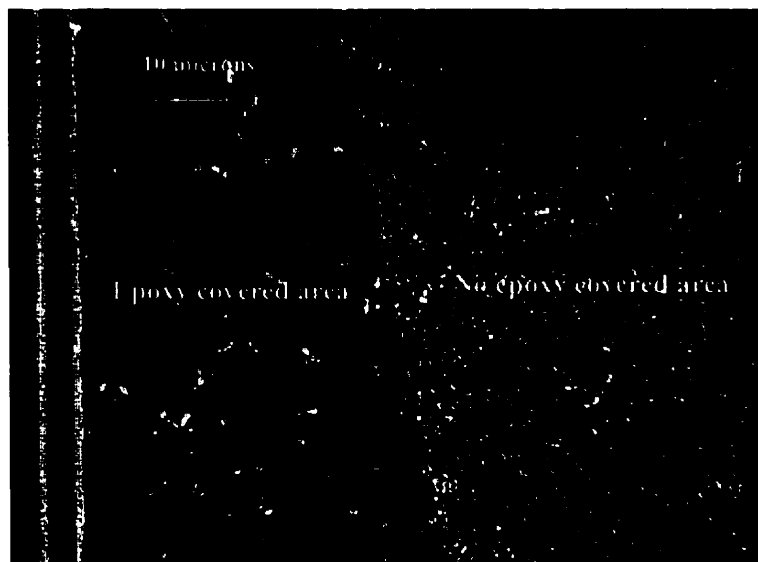

Figure 3.10 The surface of bonding pad after 15 min etching at 80 °C in 5 wt.% TMAH without silicic acid and oxidizer $K_2S_2O_8$ added

For the combinational etching, TMAH anisotropic etching only takes 30–50 minutes to release the four supporting arms of our cantilever device. But longer etching times may be needed for some devices or several etching runs. In that case, we have to consider depletion effects. From the above discussion, when the TMAH was significantly doped with silicic acid, it etches silicon slowly. The pH value is around 12.5. In fact, the solution is in some kind of balanced state, a "window" state. After 50

minutes, due to depletion of the TMAH and oxidizer from the solution, the solution begins to exhibit a lower (100) etch rate with rough etched surfaces and bubble formation.

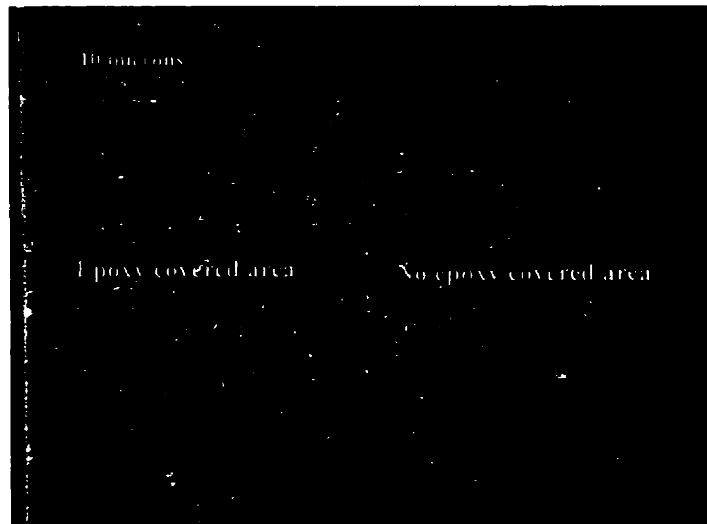

Figure 3.11 The surface of bonding pad after 15 min etching at 80 °C in 5 wt.% TMAH with 44g/L silicic acid and 3g/L $K_2S_2O_8$ added

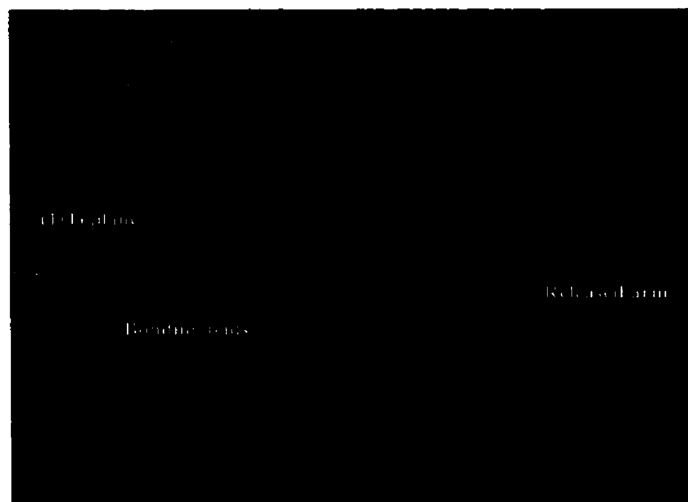

(a)

(b)

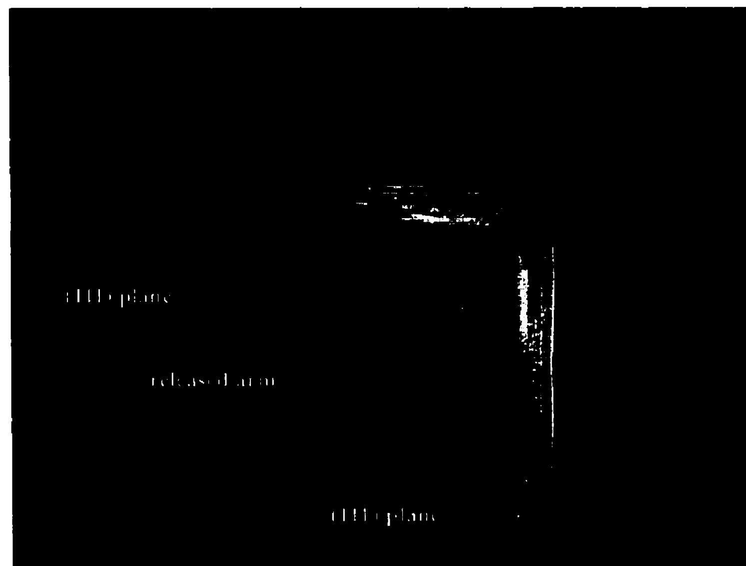

(c)

Figure 3.12 The cantilever device after 40 min etching at 80 °C in 5 wt.% TMAH with 44 g/L silicic acid and 3 g/L $K_2S_2O_8$ added

To maintain the (100) etch rate and smooth etched surface, 5 ml/L 25 wt.% TMAH and 3 g/L potassium persulfate should be add into the solution every 30 minutes to compensate for the depletion.

Figure 3.12 shows the cantilever device after 40 min etching at 80 °C in 5 wt.% TMAH solution with 44 g/L silicic acid and 3g/L $K_2S_2O_8$. The etching results proved that our modified 5 wt. % TMAH is an aluminum-passivated anisotropic solution with smooth etched (100) surfaces.

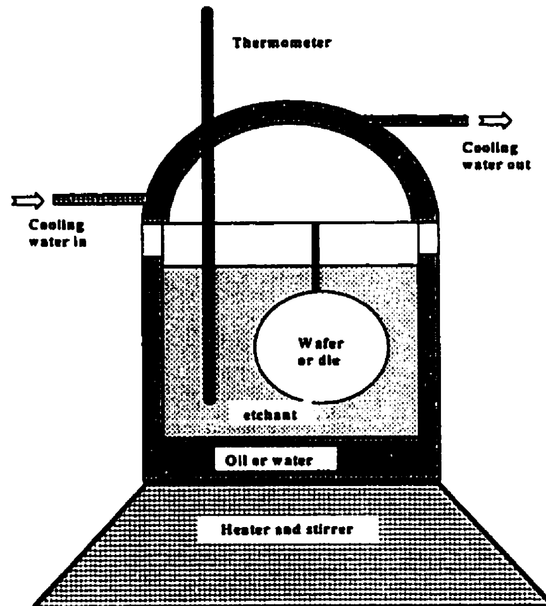

Figure 3.13 The setup for 5 wt.% TMAH etch

3.2.2 Etching procedure

The TMAH etching was conducted in the setup showed in Figure 3.13. The cooling water prevents the evaporation of water from the TMAH causing a concentration change. During etching, a magnetic bar has to be used to stir the solution to help etching uniformity. It was found that vigorous stirring is very important for obtaining a smooth

etched surface in 5 wt.% TMAH. To avoid trapping H_2 bubbles in the etched pits, the etched surface should face upwards. Before loading into the TMAH solution, the chip has to be ultrasonically cleaned in acetone for 15 minutes. After rinsed in DI water, the die was put into 20:1 BOE for 5 to10 seconds to remove native oxide. After another rinse in DI (de-ionized) water, the chip is ready for the TMAH etch.

3.3 XeF_2 Isotropic Etch

It is relatively easy and inexpensive to set up a XeF_2 etch system. The XeF_2 isotropic etch is a dry etching process that operates at room temperature, and makes it an ideal etchant for releasing extremely compliant structures. XeF_2 is a white crystalline solid with a vapor pressure of about 600 Pa (4.5 Torr) at room temperature. It is fully compatible with materials used in a commercial CMOS processes, namely, no noticeable attack of silicon dioxide, silicon nitride, and aluminum. The reaction equation for XeF_2 and silicon is given by

$$2XeF_2 + Si \rightarrow 2Xe + SiF_4 \qquad (3.1)$$

The reaction is exothermic and does not require heat or a catalyst to activate. The main product, SiF_4, is volatile at room temperature. Other byproducts of the reaction are small amounts of SiF, SiF_2, SiF_3 and Si_2F_6.

The XeF_2 etching system used in our laboratory is outlined in Figure 3.14. The XeF_2 chamber contains the XeF_2 crystals. The expansion chamber has a volume of 200 mL. The XeF_2 vapor is expanded into this chamber for a fixed pressure. The etching chamber is where the CMOS MEMS device is place for etching. It has a volume of 400

mL. A mercury pressure gauge is used to monitor the pressure in the etching chamber and expansion chamber. The pump is a standard mechanical pump.

A XeF_2 etch is performed by a pulse method. First, the expansion chamber is filled from the sublimating crystals in the XeF_2 chamber until a target pressure of 3 Torr is reached, while the etch chamber is pumped down. This may take up to 60 seconds.

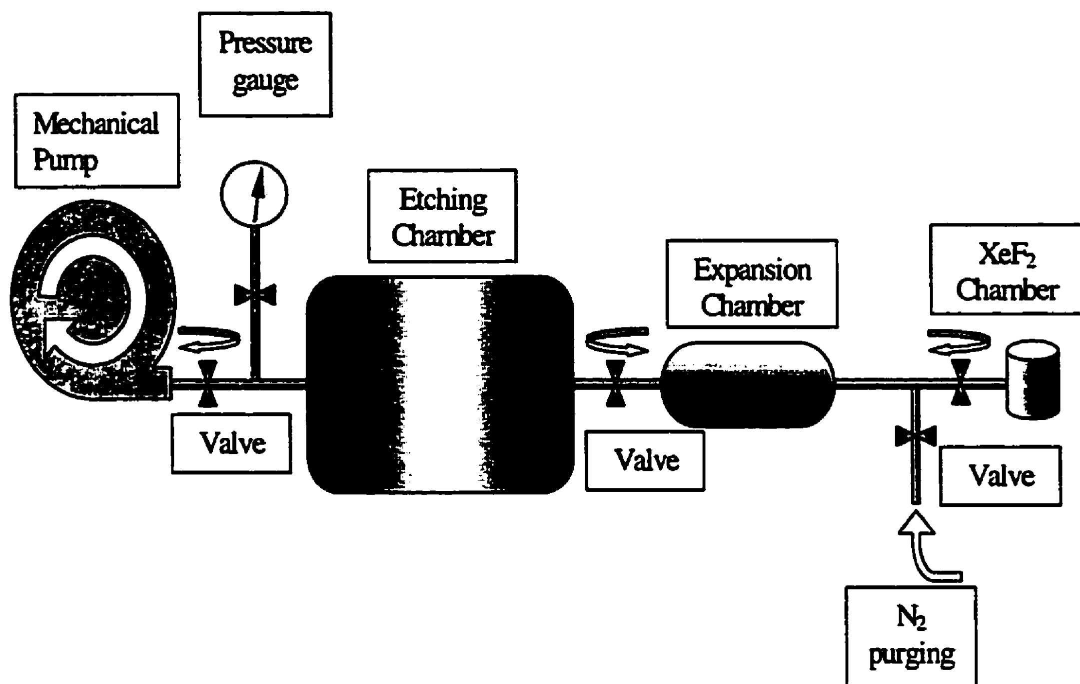

Figure 3.14 Schematic drawing of XeF_2 etching system

Once the target pressure is reached, the expansion chamber is isolated from the XeF_2 chamber, the etch chamber is isolated from the pump, and the valve between the expansion and etch chambers is opened. The pressures (typical target pressure in the etching chamber is 1 Torr) equilibrate in less than a couple of seconds and a waiting

time of about 20 seconds occurs before the etch starts. Silicon does not start etching instantaneously upon exposure to XeF_2 because it first requires the formation of a few fluorosilyl layers. The actual etch rate of silicon varies depending on the amount of exposed silicon and other parameters such as temperature and pressure. The etch rate is not a linear function of time. In general, silicon etching rates are much higher in the initial 20 seconds and drop off dramatically after 5 minutes. Thus, the etching duration normally takes about 20-60 seconds. For the cantilever device, the etch rate is about 1 μm/min, for an etching duration of 60 seconds.

After every fourth pulse, both the etch and expansion chambers are then backfilled with nitrogen gas and byproducts (the dominant volatile byproduct is SiF_4) are pumped from the etching chamber before the next cycle begins.

The system is equipped with an optical microscope, which provides visual monitoring of the etching process through an optical window on the top of the etching chamber. With the help of this microscope, the etching termination time can be determined. Since XeF_2 reacts with moisture to form highly corrosive hydrofluoric acid, the entire system is located in a fume hood for safety reasons.

XeF_2 is extremely selective to silicon and, thus, is an ideal CMOS post-processing etchant. Therefore, etching with XeF_2 is applicable to packaged as well as unpackaged chips. For unpackaged chips, photoresist can be used to protect the backside and peripheries of the chip because XeF_2 will etch any exposed silicon, resulting in significant thinning of the chip. We etched the packaged cantilever device in this study.

We first wire bonded the chip in the 40 pin DIP package, then protected the bonding wires, bonding pads and sides of the chip by using Norland UV optical glue

(Figure 3.15). Norland glue was chosen for its good wetting ability and rapid curing under strong UV light. A syringe with a needle of 250 µm ID was used to dispense the glue. Excellent filling in the package occurs because of the wetting ability of the glue. Fast curing under UV guarantees that the glue covers the chip bonding pads and also leaves the opening for XeF_2 etching.

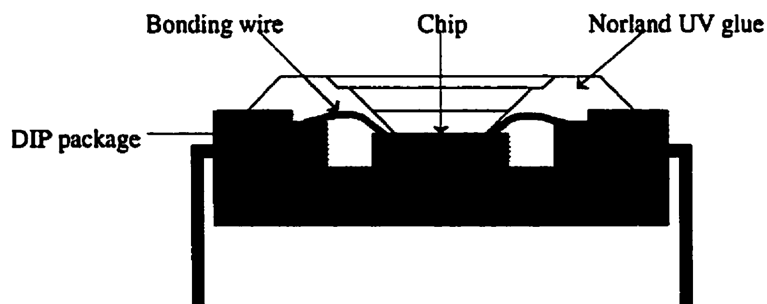

Figure 3.15 Packaged cantilever device for XeF_2 etching

To assure etching of the desired areas, a 10 sec etch in 20:1 BOE was carried out to remove the thin layer of native oxide. Also, since moisture reacts with XeF_2 to form hydrofluoric acid which attacks SiO_2, the chips are baked at 80 °C prior to etching.

The etch rate of silicon is more linear [65] at pressures over the range 0.5 Torr – 10 Torr [109,110]. The higher pressures correspond to a higher etch rate with a rougher etched surface and non-uniform undercutting around the etching window. In order to have dimensional control with high precision, a lower pressure and shorter pulse duration should be used. Figure 3.16 shows the released cantilever device, and Figure

3.17 shows the smooth etched surface. For Figure 3.17, the microscope is focused on the bottom of the etched pit.

Figure 3.16 Released cantilever device by XeF_2 etching

Figure 3.17 The smooth etched surface

After releasing in XeF_2, the devices are cut by a leaser cutting system. By cutting the connection bars at different positions, each cantilever device will have a different length and mass, and therefore, a different resonant frequency. Figure 3.18 shows one example of laser cutting. In the picture, we can see light shining on the bars, due to light reflection by using the dark field illumination mode of the microscope. This is an indication of upward bending caused by residual/internal stress in the structure.

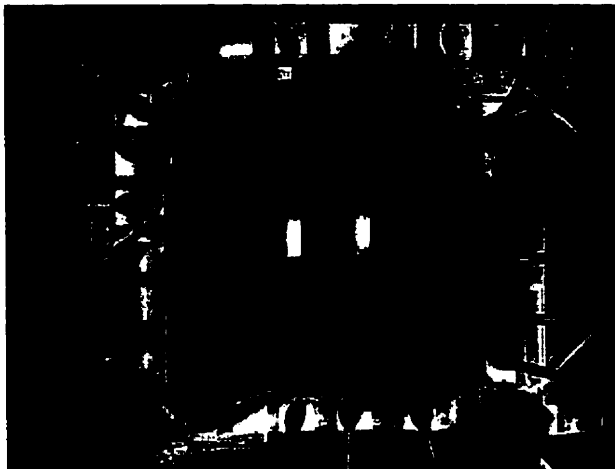

Figure 3.18 Connection bars cut by laser beam to separate two cantilevers. The cut was near the tip of the bottom cantilever

CHAPTER 4

DEVICE CHARACTERIZATION

4.1 Experimental Set-up

The actuation of the cantilever device is the result of the Lorentz force produced by the interaction of a time-varying current with a magnetic field. The experimental layout for the investigation of the dynamic behavior of a cantilever device is shown in Figure 4.1.

A chip containing the cantilever device was packaged on the 40 pin dual inline package (DIP) which was placed into a zero insertion force (ZIF) socket. A horseshoe magnet was placed on the top of the chip (Figure 4.1 (a)). The magnet was oriented so that the Lorentz forces on the cantilever arms and tip bar were maximum. Two horseshoe magnets were used, with magnetic fields of 750 G and 1500 G respectively, as measured with a model 511 Gaussmeter (LDJ Electronics Inc.). A computer-controlled data acquisition system was used to measure the piezoresistor signal [74]. The waveform generator and digital multimeter were controlled through the computer via the computer's communication ports. Twelve samples at each frequency were averaged to improve the signal quality and reduce noise effects.

The signal conditioning circuit used to measure the piezoresistor response is shown in Figure 4.2. A constant DC current of 1 mA was provided by a Wilson current mirror; the constant DC current flowing through the piezoresistor is independent of the piezoresistive load. The resistance of the piezoresistor in the cantilever arm is approximately 9.4 kΩ.

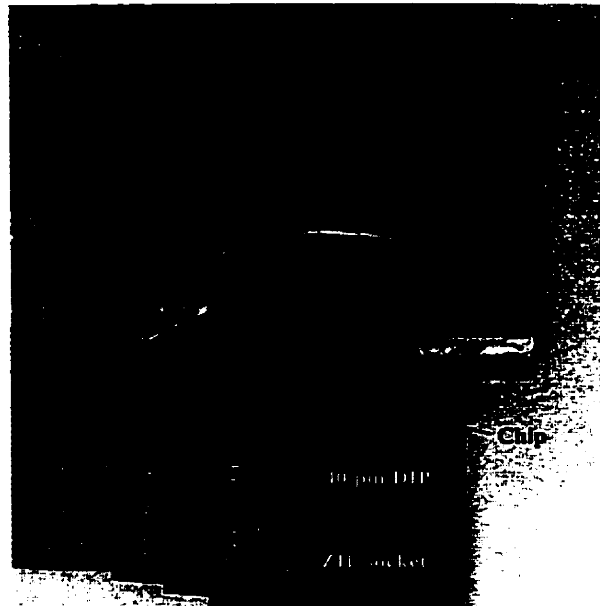

(a)

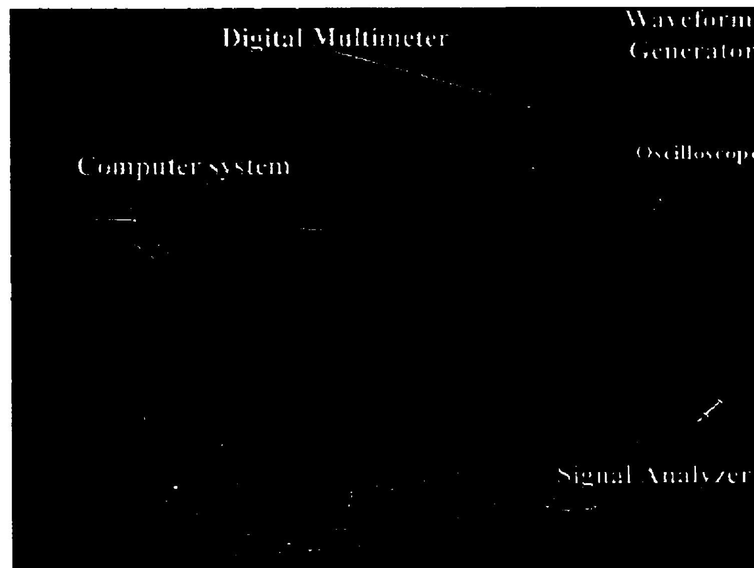

(b)

Figure 4.1 Experimental setup

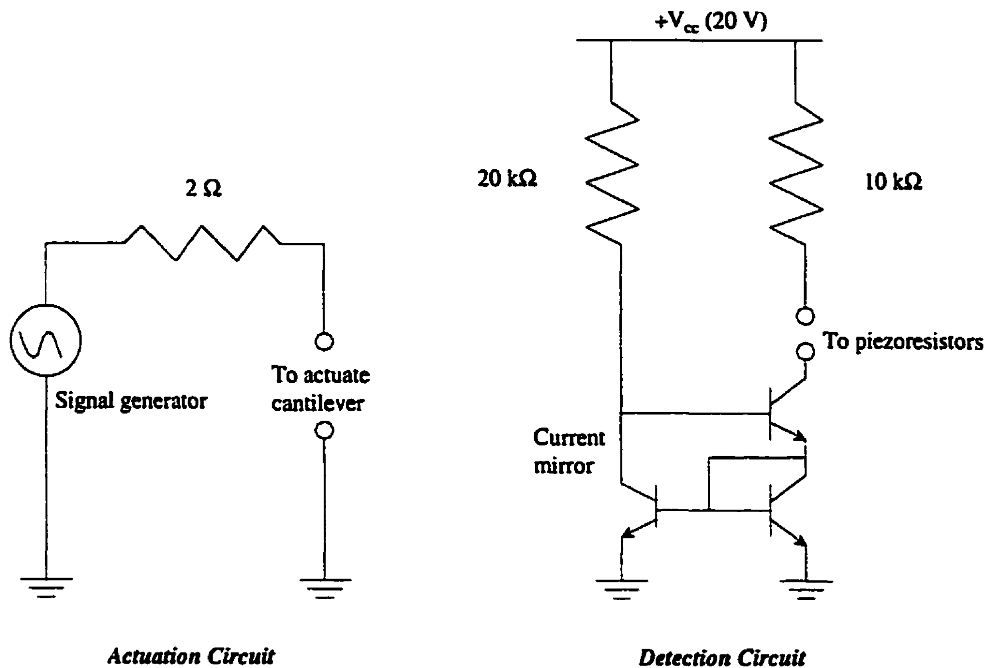

Figure 4.2 Signal conditioning circuit

4.2 Cantilever in Air

Using the experimental set-up described above, experimental results were obtained for a series of cantilevers with different lengths of remaining bar segments or stubs. Figure 4.3 shows the response of the cantilever with almost 200 μm long stubs (see Figure 3.18), while Figure 4.4 shows the response of the cantilever with almost 0 μm long stubs (see Figure 3.18). As we can see from Figure 4.3 and Figure 4.4, the longer the stubs, the lower the first resonant frequency. This is true according to equation (2.10) because longer stubs increases the mass m, and the larger the mass, the lower the resonant frequency.

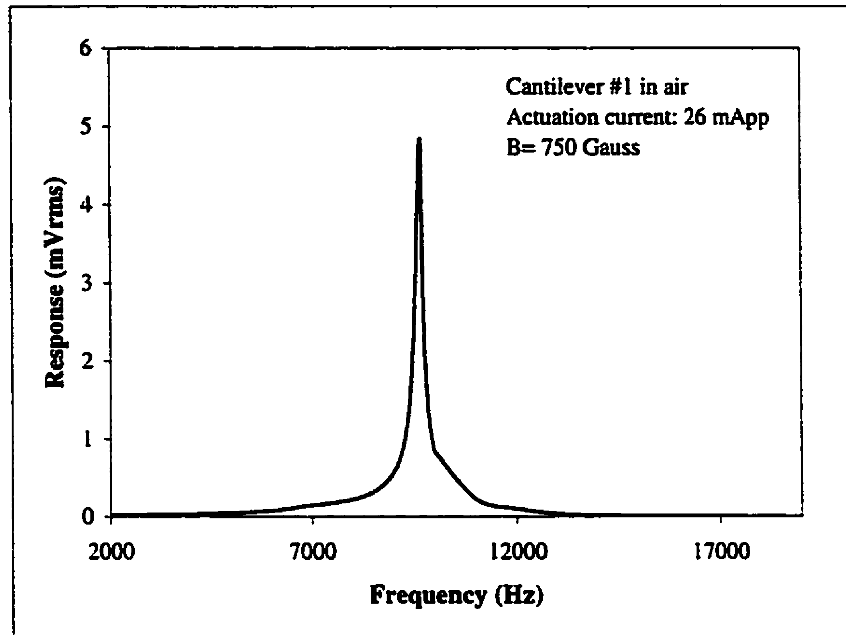

Figure 4.3 Frequency response of cantilever device with 200-μm-long stubs

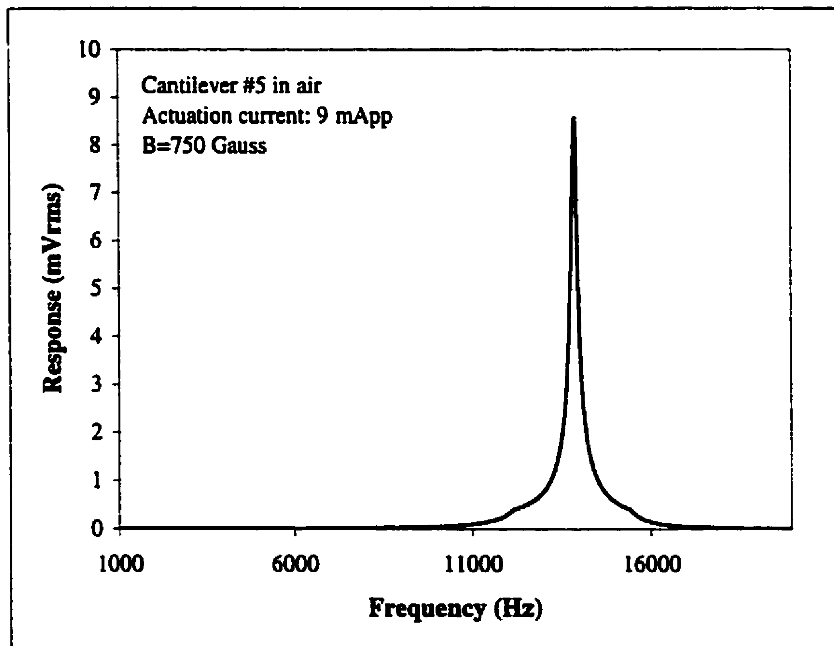

Figure 4.4 Frequency response of cantilever device with no stubs

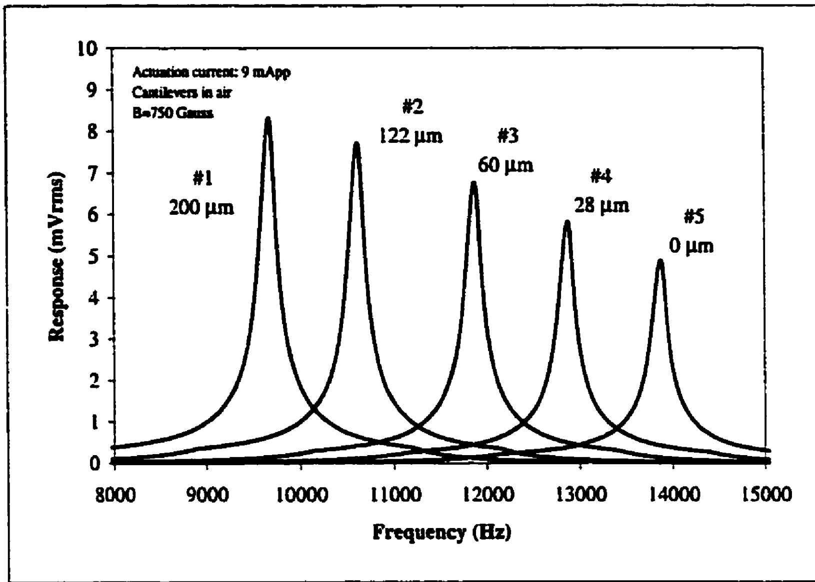

(a)

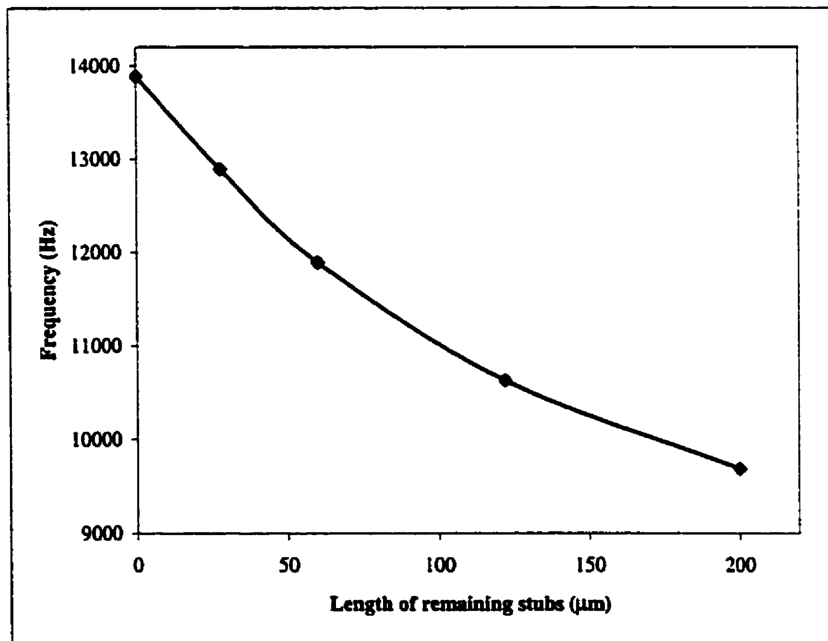

(b)

Figure 4.5 Frequency responses of cantilever devices with different lengths of stubs

Figure 4.5 shows the frequency responses of cantilever devices with different lengths of stubs. According to Equations (2.10) and (2.11), the larger the mass, the larger the response magnitude and the lower the resonant frequency. It is evident that the first resonant frequency of the cantilever device can be modulated by cutting the connection bar at different locations. From our experimental result, the first resonant frequency of the cantilever device can be easily modulated between 9.2 kHz to 14.5 kHz by simple laser cutting.

In other words, the relation between mass and resonant frequency shift can be applied for some practical applications. For example, the cantilever device can be used as a mass/humidity detector by sensing its resonant frequency shift [4,10,67,94,121].

The relationship between response and magnetic field was also carried out using the set-up indicated in Figure 4.6. The cantilever device was placed a distance d from the permanent magnet. The magnetic field at the position of cantilever device was carefully measured using a gauss meter. The response of the cantilever at the 60 mm position is shown in Figure 4.7. Figure 4.8 shows the relationship between response and distance. As well, the relationship between magnetic field and response was obtained and shown in Figure 4.9.

It can be seen from (2.4) that larger response relates to larger actuation force. The magnetic field is an important part of the actuation source. Within the range we tested, the response is proportional to the magnetic field, as a near linear relationship was observed, as shown in Figure 4.9. The mismatch between the linear relationship and experimented data is believed to be due to the inaccurate measurement of the magnetic

field. This linear relationship implies that the cantilever device might be used as magnetic field sensor by monitoring its response at constant current input.

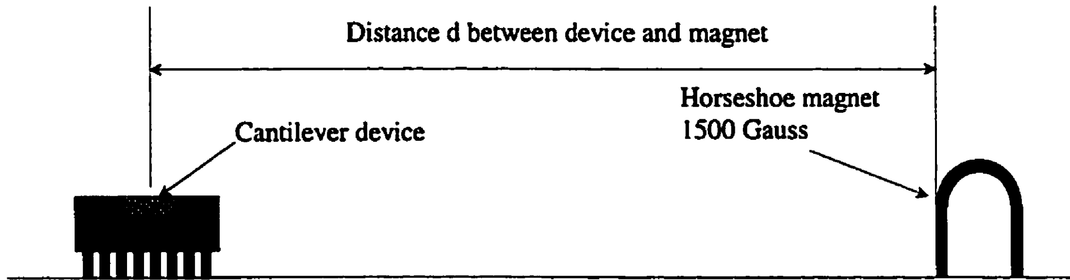

Figure 4.6 Measurement set-up for the relationship between response and magnetic field

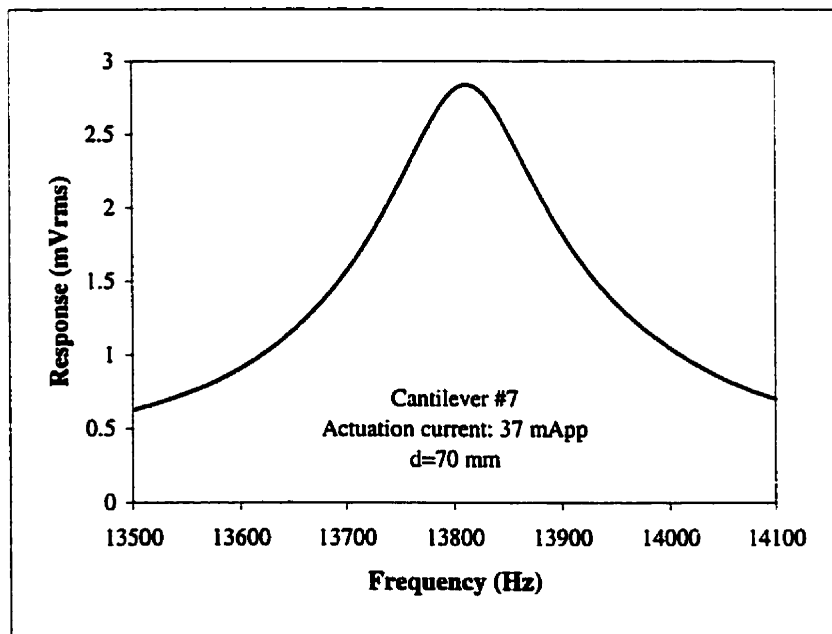

Figure 4.7 The frequency response of cantilever at a distance of 60 mm

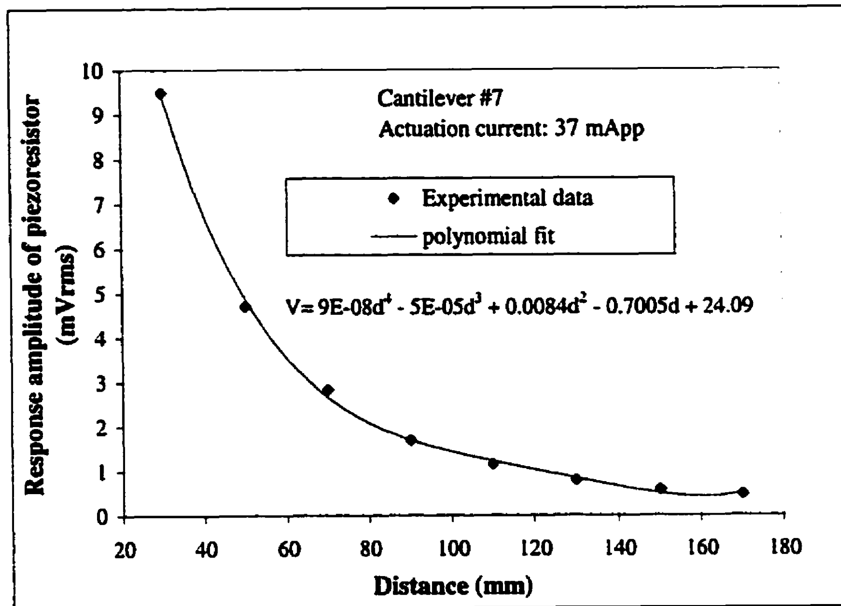

Figure 4.8 The relationship between response and distance

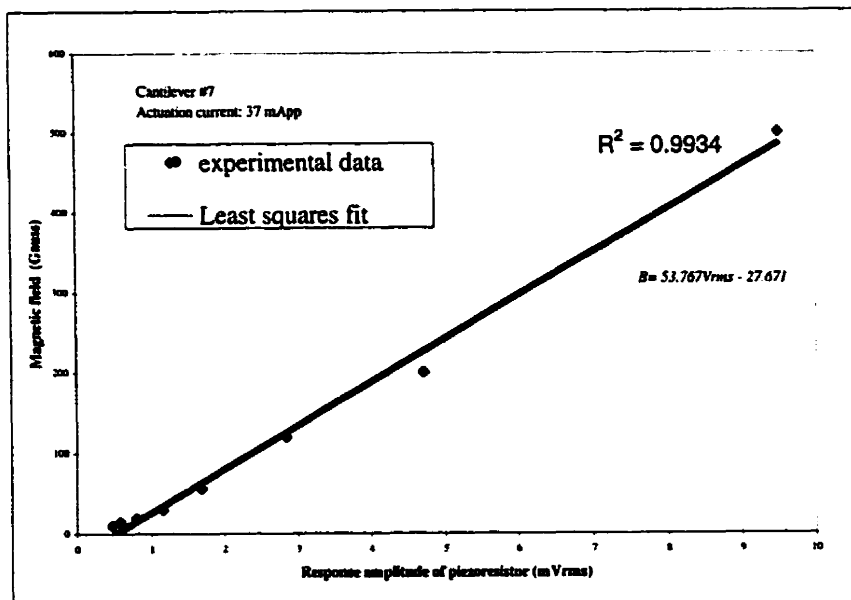

Figure 4.9 The relationship between magnetic field and response

4.3 Cantilever in Vacuum

The dynamic behavior of the cantilever device was characterized in vacuum. The vacuum system consisted of a bell jar and a mechanical pump. Pressures between 20 Torr and atmospheric pressure were obtained with this system. The cantilever device and magnet were placed inside the bell jar. An illustration of this set-up is shown in Figure 4.10.

Figure 4.10 Bell jar experimental set-up

Using the experiment setup described, experimental results were obtained as pressures were varied from 18 Torr to atmospheric pressure with constant actuation realized by using same magnet and same amount of actuation current. Figure 4.11 shows the response of the cantilever device at pressures of 100 Torr and 300 Torr. As shown in the figure, the response, frequency shift and quality factor depended on the pressure. The

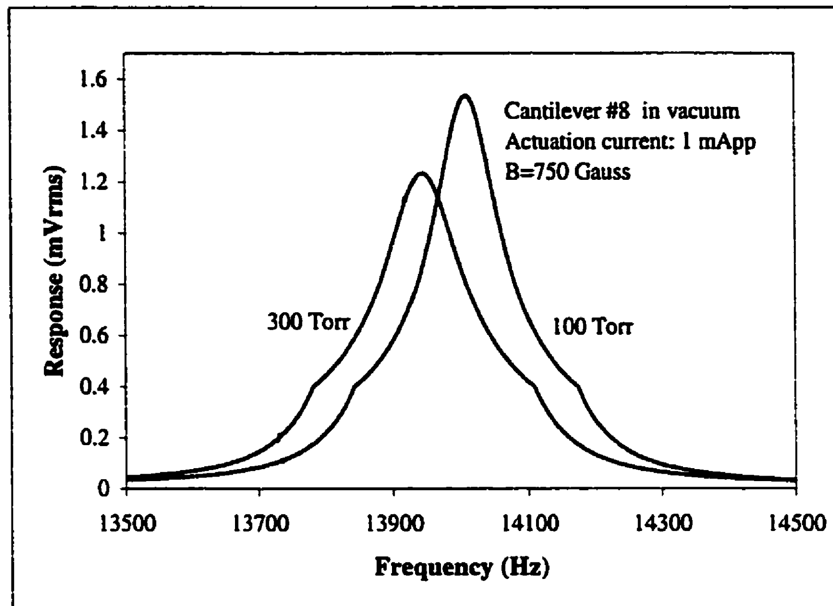

Figure 4.11 Frequency response of one cantilever device at pressures of 100 Torr and 300 Torr at constant actuation

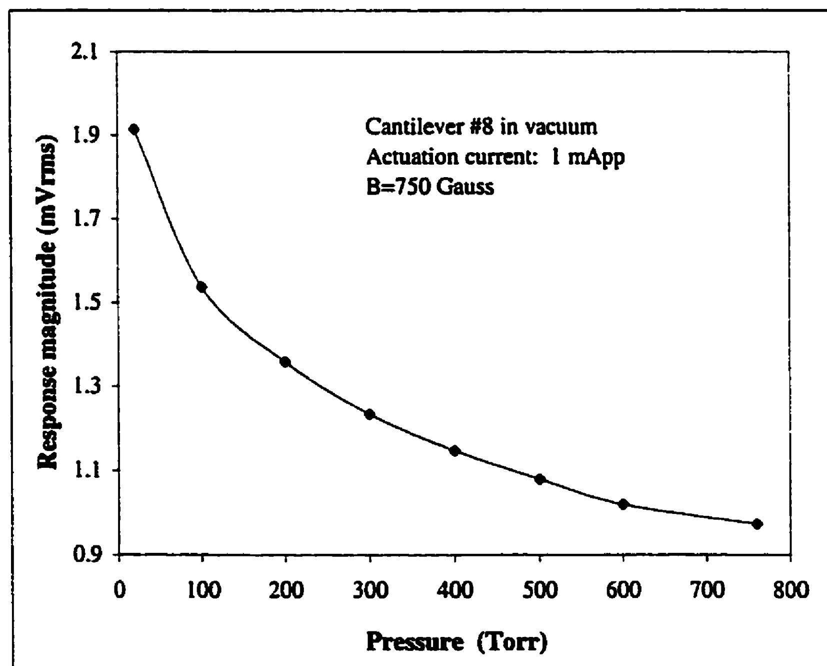

Figure 4.12 The response versus pressure for cantilever device at constant actuation

small peaks of about 0.4 mV on the either side of piezoresistive response peak presented in Figure 4.11 and next figures of this chapter are caused by the measurement scale change of the digital multimeter.

Under different pressures, the cantilever device experiences different damping, with higher pressure producing higher damping. According to (2.4), (2.10) and Figure 2.3, the larger damping results in smaller response, quality factor and resonant frequency. A plot of response versus pressure for the cantilever device is shown in Figure 4.12. Figure 4.13 shows the first resonant frequency versus pressure for the cantilever device at constant actuation. As shown in Figure 4.13, the relationship between the resonant frequency and pressure is close to linear from 20 Torr to 500 Torr. In this pressure range, the best fit equation shown in Figure 4.12 is linear.

The quality factor Q is an important characterization parameter for damped vibration. It is defined as:

$$Q = \frac{f_0}{\Delta f} \tag{4.1}$$

Where f_0 is the resonant frequency, and Δf is the width of the half power point, that is, the width of the response peak where the square of the amplitude has half its maximum value. As damping increases due to increased ambient pressure, the quality factor decreases with increasing pressure. Figure 4.14 shows the quality factor versus pressure for the cantilever device at constant actuation.

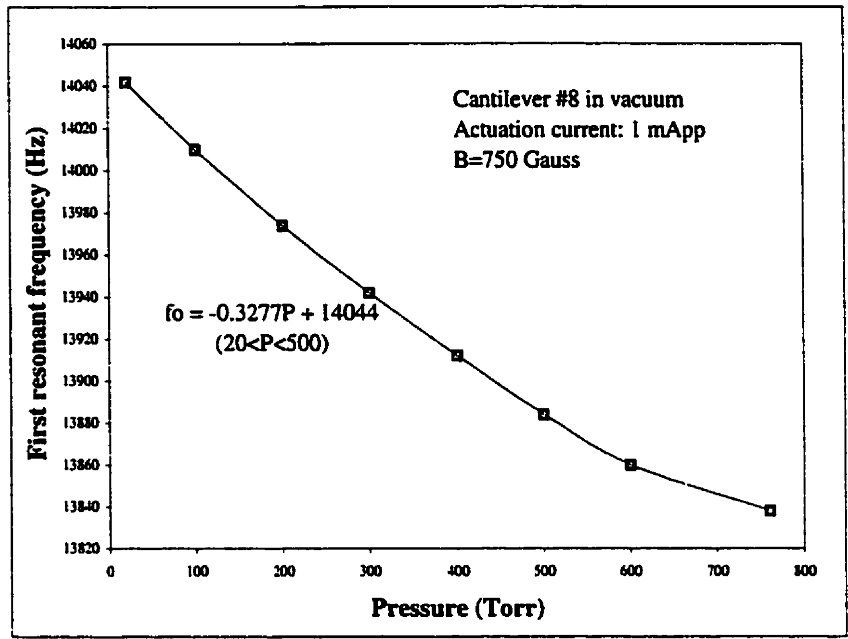

Figure 4.13 The first resonant frequency versus pressure for cantilever device at constant actuation

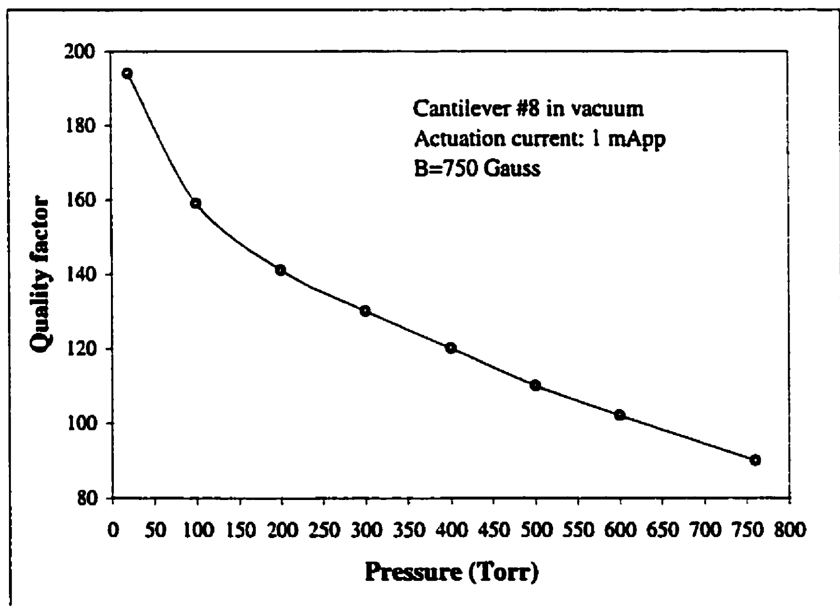

Figure 4.14 The quality factor versus pressure for cantilever device at constant actuation

4.4 Fine Tuning of the Resonant Frequency

We discussed coarse tuning of the resonant frequency by changing the laser cutting location. In this section, we discuss how to realize fine tuning of the resonant frequency. After releasing the cantilever device by post processing and laser cutting, a small amount of upward bending occurred on the supporting arms. The upward deflection on the tip bar was measured with the optical measurement system. This permanent bending is caused by residual stress, which will be discussed in Chapter 5.

It is the residual stress that stiffens the cantilever structure. Such stiffness will cause a resonant frequency increase. On the other hand, softening the structure tends to cause a resonant frequency decrease. Thus, if we can increase or decrease the residual stress, the manipulation of the resonant frequency can be achieved.

Table 4.1 Measurement results of DC current on the resonant frequency at a pressure of 18 Torr

Resonant Frequency (Hz)	**Actuation DC current (mA_{pp})**								
	+30	+16	+8	+4	0	-4	-8	-16	-30
Measurement	14031	14013	14003	13997	13990	13989	13988	13987	13986

Since the cantilever device has two metal loops, one of them can be used for actuation by AC current, the other one can be used to input DC current. In the magnetic field, the DC current will interact with magnetic field and produce either an upward or downward force depending on its polarity. Correspondingly, the DC current either increases or decreases the residual stress. Therefore, the resonant frequency can be

varied about its original frequency, which is determined by the structure and residual stress. Table 4.1 and Figure 5.10 show some test results. Different loadings nonlinearly change the residual stress in the cantilever device, and the residual stress in turn changes the effect stiffness of the device. The resultant small frequency change is therefore neither symmetrical nor linear. It can be seen from the table that the DC effect on the resonant frequency not only depends on the DC current magnitude but also the current direction.

4.5 Band Pass Filter

As we discussed in the previous sections, the resonant frequency can be coarsely and finely tuned. If we consider the cantilever device as a filter, the input signal is the signal flowing through the metal loop as an actuation current, and the output signal is the response signal picked up by the piezoresistor. For a specific cantilever device with a certain resonant frequency, the input signal can be picked up by the piezoresistor and "pass through" the cantilever only when the input signal causes the cantilever to vibrate at or near resonance. On the other hand, if the input signal does not cause the cantilever to vibrate, then the signal is blocked by the cantilever. In general, a single cantilever only passes the input signal whose frequency is near the cantilever's resonant frequency. As a filter, a single cantilever device has a narrow bandwidth.

If we connect two suitably tuned cantilevers in series, they will have wider bandwidth. An illustration of this idea is shown in Figure 4.15. It is clear that both cantilevers must have close resonant frequencies for the purpose of signal superposition. Figure 4.16 and Figure 4.17 show the responses of cantilevers #11 and #14,

respectively. Both were actuated by 2 mA current in a 750 gauss magnetic field. Figure 4.18 shows the response of the cantilevers connected in series under the same current and magnetic field.

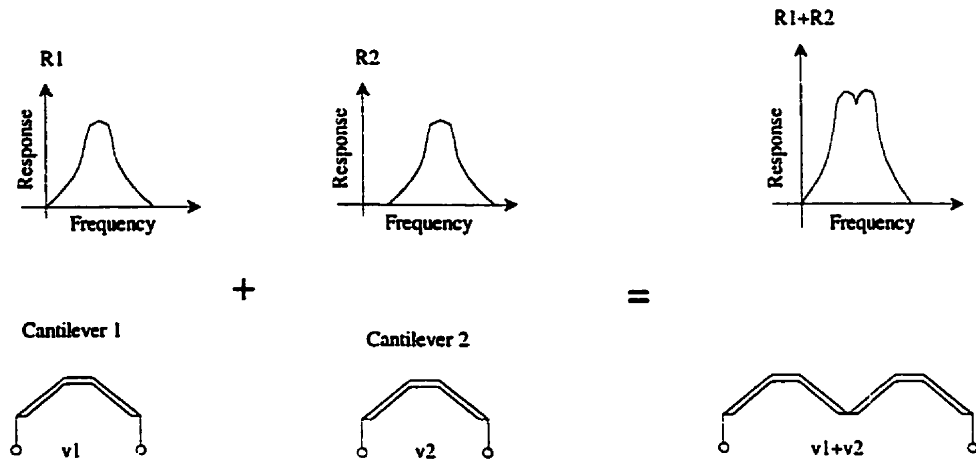

Figure 4.15 An illustration of realization of band pass filter

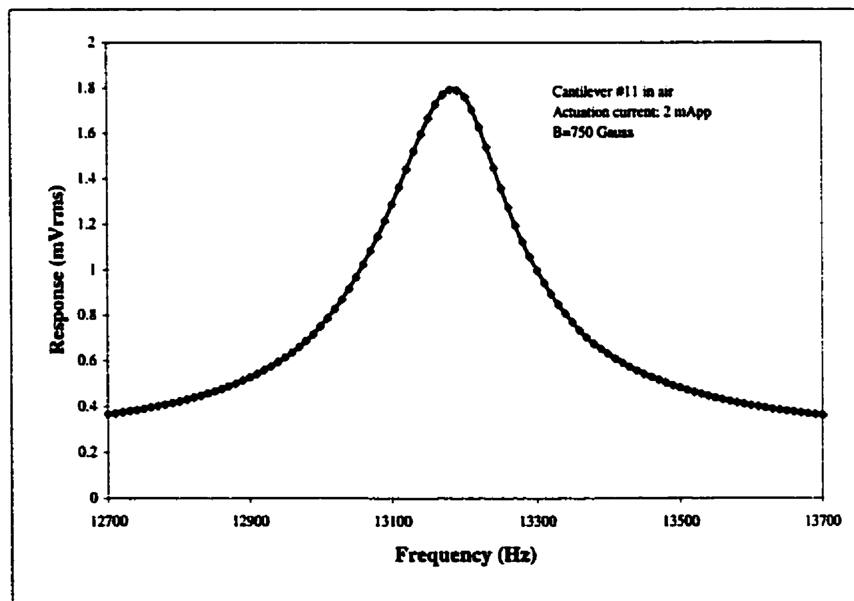

Figure 4.16 The response of the cantilever #11 under 2 mA current actuation

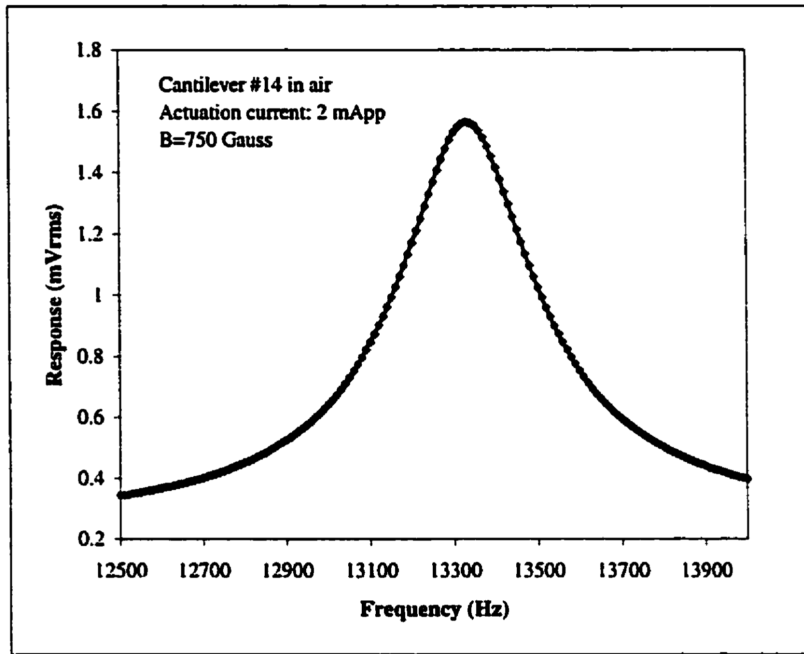

Figure 4.17 The response of the cantilever #14 under 2 mA current actuation

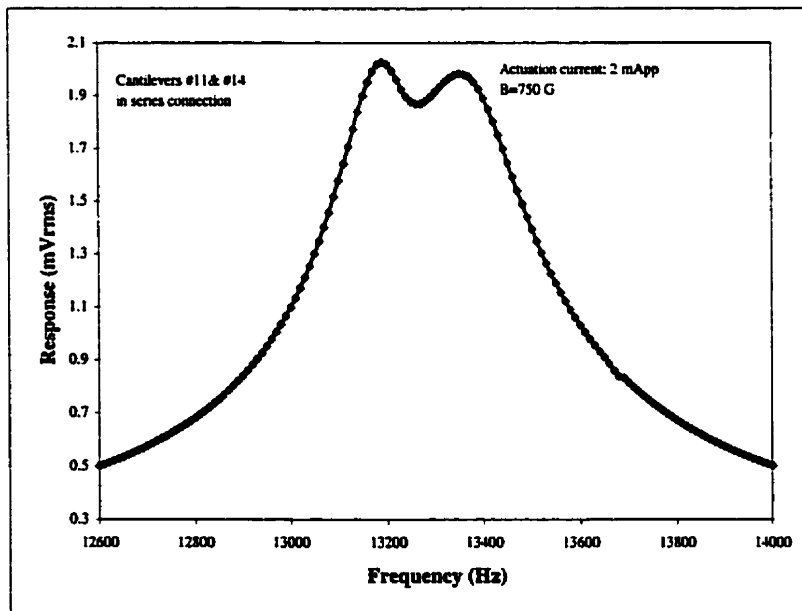

Figure 4.18 The response of cantilevers #11 and #14 in series connection under 2 mA current actuation

4.6 Cantilever in Liquids

When a fluid is subjected to external forces, it resists flow due to internal friction. Viscosity is a measure of this internal friction. Kinematic viscosity is a measure of the resistive flow of a fluid under the influence of gravity. When two fluids of equal volume are placed in identical capillary viscometers and allowed to flow by gravity, a viscous fluid takes longer than a less viscous fluid to flow through the capillary. If one fluid takes 200 seconds to complete its flow and another fluid takes 400 seconds, the second fluid is twice as viscous as the first on a kinematic viscosity scale. Absolute viscosity, sometimes called dynamic or simple viscosity, is the product of kinematic viscosity and fluid density. The SI unit of kinematic viscosity is mm^2/s. Absolute viscosity is expressed in units of centipoise (cP). The SI unit of absolute viscosity is the milliPascal-second (mPa-s), where 1 cP = 1 mPa-s.

There are a variety of techniques to measure liquid viscosity. Capillary viscometers and rotary viscometers are commonly used instruments. In this section, we discuss the possibility of using a cantilever structure to measure the liquid viscosity.

Two kinds of liquids were used in this study. One is deionized (DI) water; the other is isopropyl alcohol (IPA). They were loaded onto the chip using a syringe with a 250-micron ID needle. During the test, the cantilever device was totally submerged in the liquid. All the electrical connections were sealed with dielectric materials and UV epoxy glue to prevent any electrical interference.

As we expected, the liquids produce heavy damping. This can be seen in Figure 4.19 and Figure 4.20. Cantilever #1 was actuated by 75 mA_{pp} AC current in the 750 gauss magnetic field. The resonant frequency dropped from 9.25 kHz in vacuum to 4.44

kHz in DI water and 3.74 kHz in IPA. The response magnitudes were small even though the actuation current was much larger compared to that in air and vacuum. The quality factors were 2.0 in the DI water and 1.1 in IPA as estimated from the data curves.

Table 4.2 shows the summary of the results. According to the CRC handbook, the absolute viscosity of water at 30 ^{0}C is 0.7975 cP, while the IPA has a viscosity of 1.77 cP at the same temperature. From the measurement results, it is evident that the more viscous IPA produces more damping on the cantilever device than the less viscous DI water. The resonant frequency decreases with increasing liquid viscosity. By monitoring the resonant frequency shift, we can measure the liquid viscosity. Calibration will be required, and temperature effects must also be considered.

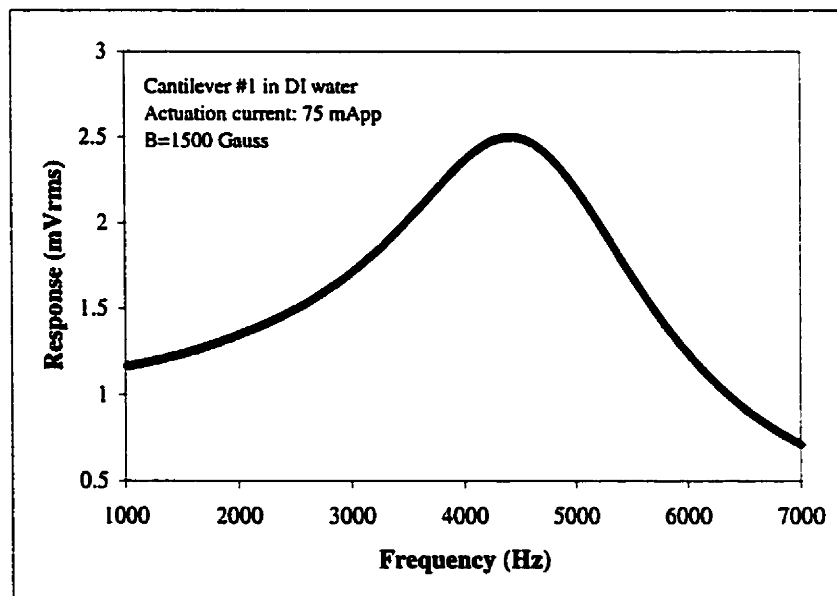

Figure 4.19 The response of cantilever #1 in DI water

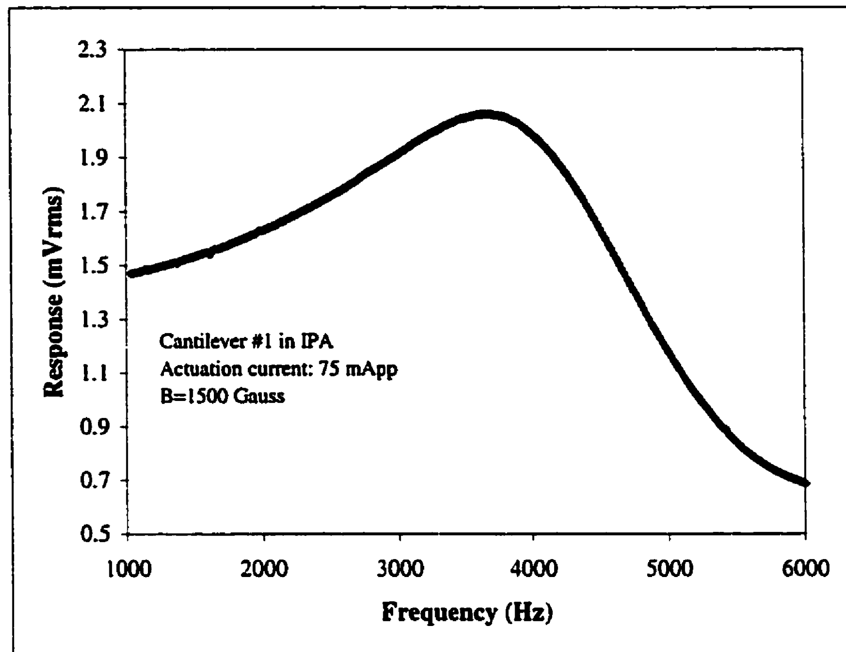

Figure 4.20 The response of cantilever #1 in IPA

Table 4.2 Measurement results of cantilever in liquids

Liquids	Density* (g/cm^3)	Viscosity* (cP)	Frequency (Hz)	Q	Response (mVrms)
IPA	0.78	2.88 @ 15^{0}C 1.77 @ 30^{0}C	3740	1.1	2.1
DI water	1	1.139 @ 15^{0}C 1.002 @ 20^{0}C 0.797 @ 30^{0}C	4440	2.0	2.5

* *Viscosity data come from CRC Handbook of Chemistry and Physics*

Because of its small size and small amount of liquid sample needed, a MEMS cantilever viscometer could be very useful in some areas. One practical application is

real-time monitoring of blood viscosity. The cantilever device can be placed inside the patient's blood vein for the real time viscosity measurement instead of drawing the blood out of the body. It is very important to monitor the blood viscosity for some patients who suffer from diabetes. For these patients, when their blood sugar becomes high, their blood will thicken and produce higher viscosity. The viscosity can be related to the blood sugar level.

Another application for the cantilever viscometer is in combinational materials science [119]. In this field, people use combinational techniques which create vast numbers of compounds by reacting a set of components in all possible combinations at once. It also referred to as "combinatorial chemistry." The underlying principles of the combinatorial approach are to synthesize *microscale* quantities of a compound, and then to test thousands of these compounds quickly and reliably. Combinatorial technologies accelerate the speed of research, maximize the opportunity for breakthroughs of discovering new materials. The cantilever viscometer is a perfect candidate to measure the viscosity in this field because it only needs *microscale* quantities of a synthesized compound.

4.7 Hysteresis

An hysteresis phenomenon was observed in our measurements. Hysteresis is a non-linear effect, and occurs when there is a large deflection of the cantilever. The large deflections happen at lower pressure with constant actuation or with larger actuation at constant pressure. One obvious manifestation of hysteresis is the response curve losing its symmetry (Figure 4.21). The frequency at which the response peak occurs is

dependent on the whether the actuating signal is increasing or decreasing in frequency. Figure 4.22 shows the response of cantilever #5 in the air with 36 mApp of actuation current. The frequency was swept from 13 kHz to 15 kHz and then backs down to 13 kHz. Figure 4.23 shows the same device in air at 300 Torr with a smaller actuation current. Hysteresis results in the response where the curve is dependent on the direction of frequency sweeping.

Larger deflection changes the stiffness of the structure; therefore the resonant frequency is changed. The response curve of the cantilever bends to the right (Figures 4.21, 4.22 and 4.23). According to Duffing's equation for non-linear spring vibration, the cantilever device demonstrates the hard spring effect [85,86,107], while Brown [74] observed a soft spring effect with a CIC structure.

To most sensors and actuators, many useful applications are often in their linear domain. For our cantilever devices, non-linear hysteresis can be eliminated by avoiding large response/deflection. That is, small actuation should be applied.

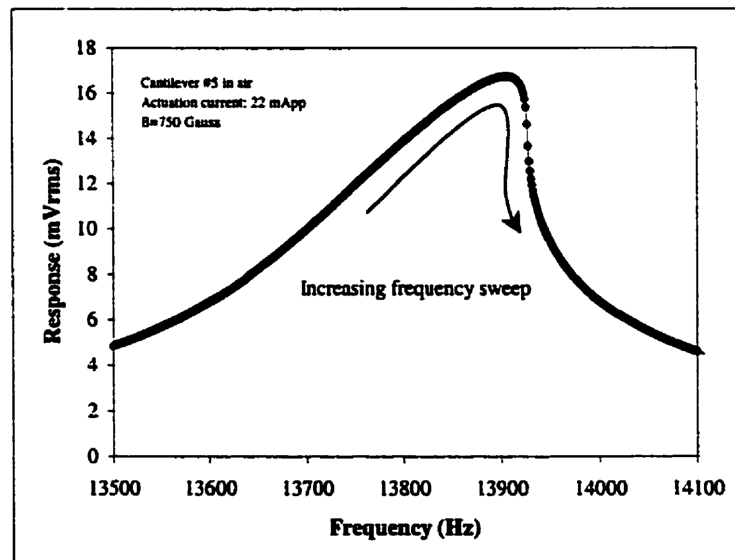

Figure 4.21 Response of cantilever #5 in air with 22 mA of actuation current

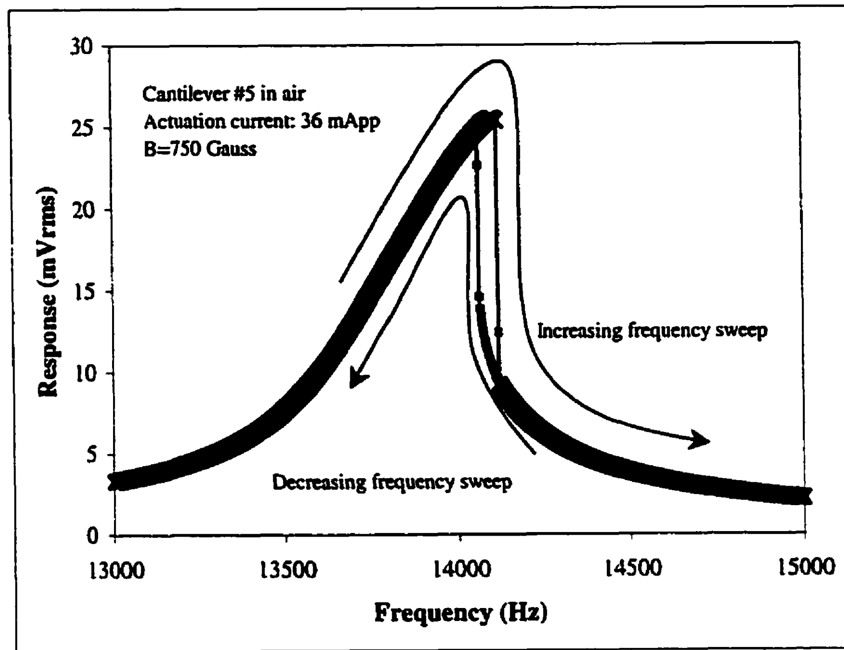

Figure 4.22 Response of cantilever #5 in air with 36 mA of actuation current

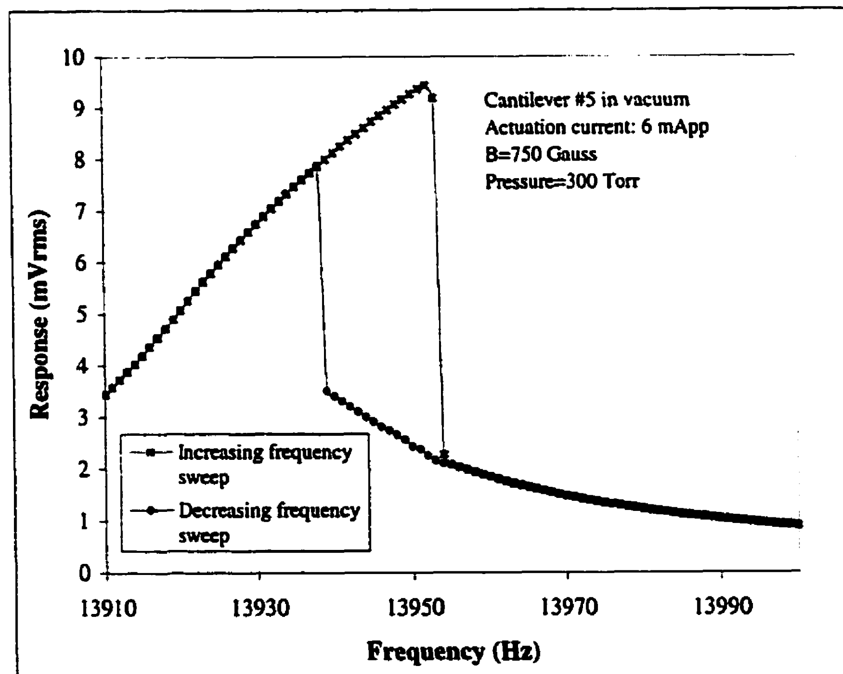

Figure 4.23 Response of cantilever #5 in 300 Torr vacuum with 6 mA of actuation current

CHAPTER 5

DEVICE MODELING

5.1 Cantilever Deflection Caused by Thermal Stress

Thermal effects produce important contributions to film residual stress [11,14,15,16,17]. Films prepared at elevated temperatures and then cooled to room temperature will be thermally stressed, as will films that are thermally cycled or cooled from ambient or cryogenic temperatures. The model of temperature-dependent bending for cantilever devices described in this section is based on references [11,15,17]. Devon described a model for predicting the static behavior of a piezoelectric cantilever actuator with an arbitrary configuration of elastic and piezoelectric layers [15]. Lakdawala and Fedder extended Timoshenko's treatment of thermal bimorphs [14] and set up the model for temperature-dependent curl of CMOS micromachined beams. They did not consider biaxial modulii in their paper. We consider biaxial modulii in the next discussion.

The basic geometry of an n-layer cantilever is shown in Figure 5.1. The residual stress effects in each layer are represented by a reference temperature at which the cantilever is completely flat. Each layer, j, has a thickness t_j, width w_j, coefficient of thermal expansion α_j, Young's modulus E_j and Poisson ratio γ_j. The out-of-plane bending due to residual stress gradients in the cantilever produces a tip deflection, δ. The material properties for each layer are assumed to be uniform throughout the layer and independent of temperature.

With the above assumptions, a model describing the deflection from thermal residual stress can be obtained based on the basic principles of the mechanical static equilibrium and strain compatibility between successive layers in the cantilever. At any

cross section of the n-layer cantilever shown in Figure 5.1, axial forces must sum to zero at equilibrium since there is no external force acting on the cantilever. The total moment within the beam is calculated using point A (see Figure 5.1) as reference point.

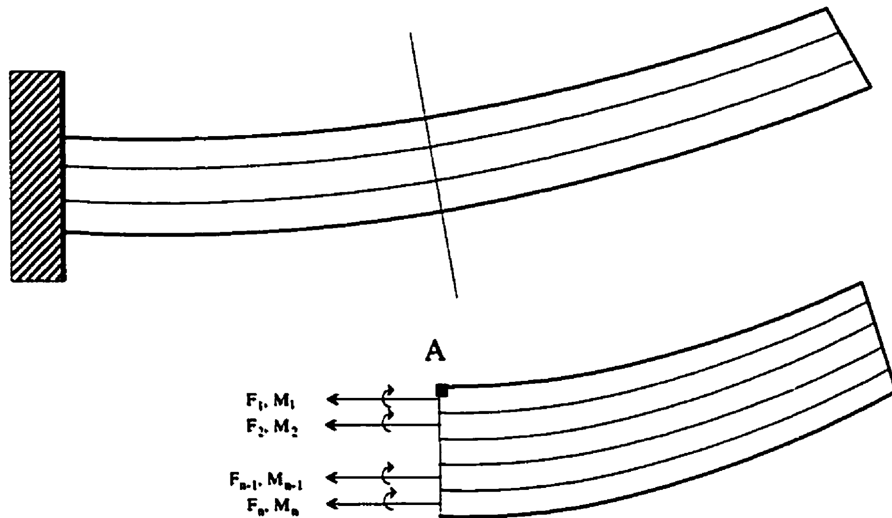

Figure 5.1 A CMOS cantilever beam

$$\sum_{i=1}^{n} F_i = 0 \tag{5.1}$$

$$\sum_{i=1}^{n} M_i = F_1(\frac{t_1}{2}) + F_2(t_1 + \frac{t_2}{2}) + ... + F_n(\sum_{j=1}^{n-1} t_j + \frac{t_n}{2}) = H^T F \tag{5.2}$$

$$F = \begin{bmatrix} F_1 \\ F_2 \\ ... \\ F_n \end{bmatrix}, \quad \text{and} \quad H = \begin{bmatrix} \frac{t_1}{2} \\ t_1 + \frac{t_2}{2} \\ ... \\ \sum_{j=1}^{n} t_j + \frac{t_n}{2} \end{bmatrix} \tag{5.3}$$

where F denotes the force column vector and H is the moment arm vector. The curvature $\frac{1}{r}$ is approximately equal for each layer in the structure since it is assumed that the cantilever thickness is much less than the overall radius of curvature, r. Thus:

$$\frac{1}{r}=\frac{M_j}{E_j^{*}I_j} \qquad \text{or} \qquad M_j=\frac{E_j^{*}I_j}{r} \tag{5.4}$$

where

$$I_j=\frac{1}{12}w_jt_j^3$$

$$E_j^{*}=\frac{E_j}{1-\gamma_j}$$

I_j is the moment of inertia of each layer having width w_j.

E_j^{*} is the biaxial modulus, as this is a case of plane stress.

Therefore, equation (5.2) becomes

$$H^TF=\frac{1}{r}\sum_{j=1}^{n}E_j^{*}I_j=\frac{X}{r} \tag{5.5}$$

where, $X=H^TFr=\sum_{j=1}^{n}E_j^{*}I_j$ represents the total flexural rigidity of the cantilever.

The total strain at the surface of each layer is given by superposition of the strain due to the axial force, thermal expansion and bending. The axial strain in the bottom half of the j-th layer is equal to that of the top half of the adjacent $(j+1)$-th layer. If T is the temperature, the strain in the bottom half of the upper layer is

$$\varepsilon_j=\varepsilon_{axial}+\varepsilon_{thermal}+\varepsilon_{bend}=\frac{F_j}{w_jt_jE_j^{*}}+\alpha_j(T-T_0)+\frac{t_j}{2r} \tag{5.6}$$

The strain in the top half of the lower layer is,

$$\varepsilon_{j+1} = \varepsilon_{axial} + \varepsilon_{thermal} + \varepsilon_{bend} = \frac{F_{j+1}}{w_{j+1} t_{j+1} E'_{j+1}} + \alpha_{j+1}(T - T_0) - \frac{t_{j+1}}{2r} \tag{5.7}$$

where T_0 denotes the reference temperature at which the cantilever has zero deflection.

Combining equations (5.6) and (5.7) results in the strain compatibility equation between successive layers in the cantilever:

$$\frac{F_{j+1}}{w_{j+1} t_{j+1} E'_{j+1}} - \frac{F_j}{w_j t_j E'_j} + (\alpha_{j+1} - \alpha_j)(T - T_0) - \frac{t_{j+1} + t_j}{2r} = 0 \tag{5.8}$$

where $j = 1,2 \ldots n-1$

Combining the equation (5.1) and (5.8), the matrix form can be written as:

$$MF + A(T - T_0) - \frac{1}{2r} W = 0 \tag{5.9}$$

where,

$$M = \begin{bmatrix} -\frac{1}{w_1 t_1 E'_1} & \frac{1}{w_2 t_2 E'_2} & 0 & \ldots & 0 \\ 0 & -\frac{1}{w_2 t_2 E'_2} & \frac{1}{w_3 t_3 E'_3} & \ldots & 0 \\ \ldots & \ldots & \ldots & \ldots & \ldots \\ 0 & 0 & 0 & \ldots & \frac{1}{w_j t_j E'_j} \\ 1 & 1 & 1 & \ldots & 1 \end{bmatrix}, \quad A = \begin{bmatrix} \alpha_2 - \alpha_1 \\ \alpha_3 - \alpha_2 \\ \ldots \\ \alpha_n - \alpha_{n-1} \\ 0 \end{bmatrix}$$

and $$W = \begin{bmatrix} t_2 + t_1 \\ t_3 + t_2 \\ \ldots \\ t_n + t_{n-1} \\ 0 \end{bmatrix}$$

By combining (5.5) and (5.9), the reference temperature is calculated as

$$T_0 = T - \frac{1}{2r}\left(\frac{2X - H^T M^{-1} W}{H^T M^{-1} A}\right) \tag{5.10}$$

For small deflection, the radius of the curvature is

$$r = \frac{L^2}{2\delta} \tag{5.11}$$

where L is the length of the cantilever.

The tip deflection of the cantilever is,

$$\delta = L^2 (T - T_0)\left(\frac{H^T M^{-1}}{2X - H^T M^{-1} W}\right) A \tag{5.12}$$

The stress vector in each layer is,

$$F = \frac{M^{-1} W}{2r} - M^{-1} A (T - T_0) \tag{5.13}$$

For the simple structure like a cantilever beam (Figure 5.1), the reference temperature in each layer can be calculated if the material properties of each layer and initial tip deflection are available. On the other hand, tip deflection and layer stress can be predicted at a certain temperature if we know the reference temperature and material properties. Furthermore, residual-stress-dependent bending in an arbitrary device can be predicted with the help of finite element analysis (FEA) based on the reference temperature and material properties.

In reference [11], a parameter extraction method based on measurement of tip deflection with temperature is proposed to extract reference temperature and material properties. Simple beam test structures composed of all metal-dielectric combinations possible in the Hewlett Packard 3-metal 0.5 μm n-well CMOS process were

experimentally characterized. The thermal coefficient of expansion (TCE) for each layer was extracted using the rate of change of tip deflection with temperature.

$$\frac{\partial \delta}{\partial T} = L^2 \left(\frac{H^T M^{-1}}{2X - H^T M^{-1} W} \right) A \tag{5.14}$$

We submitted a simple cantilever beam design with 9 possible combinations of metal1, metal2, passivation and poly1 (see Table 5.1). The cantilever is 50 microns wide and 250 microns long. To date, the chips have not been fabricated and returned for testing. As a part of future work, a series of experiments including the temperature test will be conducted to extract the reference temperature and material properties.

Table 5.1 Cantilever combinations for parameter extraction

Layers	Thickness (μm)	#1	#2	#3	#4	#5	#6	#7	#8	#9
Nitride	0.5	√					√	√	√	
SiO_2	0.5	√					√	√	√	
Metal1	0.8		√			√		√	√	
SiO_2	0.8					√			√	
Metal2	0.8			√		√	√		√	
SiO_2	0.8					√	√	√	√	
Poly2	0.3				√	√	√	√	√	
Oxide	1.0					√	√	√	√	√

5.2 Finite Element Model for Cantilever Device

When the cantilever was released by post processing, the cantilever tip had upward bending. The 37 μm of deflection on the cantilever tip was measured optically. The optical measurement system had an accuracy of +/- 0.5 μm. The first resonant frequency of the cantilever without any connection bar was measured as 13995 Hz as described in Chapter 4.

At this point, we haven't received our chip from CMC to extract cantilever material properties. Fortunately, with the help of references [12] and [104], we had rough range of material properties for metal, polysilicon and dielectric materials. However, the specific material properties and reference temperature for our cantilever were not available, so fine parameter tuning had to be performed with the help of an ANSYS analysis.

By doing the static thermal stress analysis and modal analysis with ANSYS, we obtained estimates for material properties and reference temperature for the cantilever. It was a procedure of optimization in ANSYS. The design parameters were the material properties and reference temperature. First, we selected a set of material properties and reference temperature based on the references [12] and [104], then we calculated the tip deflection and resonant frequency at room temperature with ANSYS. If both calculated deflection and resonant frequency were very close to their measured counterparts, within 3 percent, the calculation was stopped and the material properties and reference temperature used in the ANSYS analysis would be accepted as the best fit. Otherwise, we kept modifying these parameters and performing the ANSYS calculation again. The

reference temperature of 460 K and material properties were obtained after 17 ANSYS runs. The analysis results are shown in Table 5.2.

Table 5.2 (a) Cantilever tip bending and first resonant frequency

	Deflection (μm)	**Resonant frequency** (Hz)
Measurement	37.0	13995
ANSYS	37.58	13990

Table 5.2 (b) Material properties of the cantilever device

Layer	Thickness *(μm)*	Young's Modulus *(GPa)*	Poisson Ratio	TCE *(10^{-6}/K)*	Density *(kg/m^3)*
Nitride	0.5 (0.5*)	140 (110)	0.3 (0.3)	3.66 (3.66)	3187 (3187)
Oxide	0.5 (0.5*)	46 (50)	0.17 (0.17)	0.4 (0.35)	2200 (2200)
Metal1	0.8 (0.8*)	60 (60)	0.33 (0.33)	33 (26)	2700 (2700)
Oxide	0.8 (0.8*)	46 (50)	0.17 (0.17)	0.4 (0.35)	2200 (2200)
Metal2	0.8 (0.8*)	60 (60)	0.33 (0.33)	33 (26)	2700 (2700)
Oxide	0.8 (0.8*)	46 (50)	0.17 (0.17)	0.4 (0.35)	2200 (2200)
Poly2	0.3 (0.3*)	150 (161)	0.23 (0.23)	2.4 (2.4)	2320 (2320)
Field oxide	1.0 (1.0*)	46 (60)	0.17 (0.17)	0.4 (0.35)	2200 (2200)

Note:

*The data in the brackets are initial values of the material properties in ANSYS calculation. The data with mark * are provided by the Mitel. The remaining initial data are based on references [12,104]*

In the ANSYS calculation, the finite element SHELL 99 was used. SHELL99 may be used for layered applications of a structural shell model. It usually has a smaller element formulation time. SHELL99 allows up to 250 layers. The element has six

degrees of freedom at each node: translations in the nodal x, y, and z directions and rotations about the nodal x, y, and z-axes. SHELL 99 is very effective for surface micromachined layered devices because it can significantly reduce the number of elements, and therefore save precious computer resources such as memory size and CPU time. The ANSYS finite element model is shown in Figure 5.2. It has 150 SHELL 99 elements and 553 nodes.

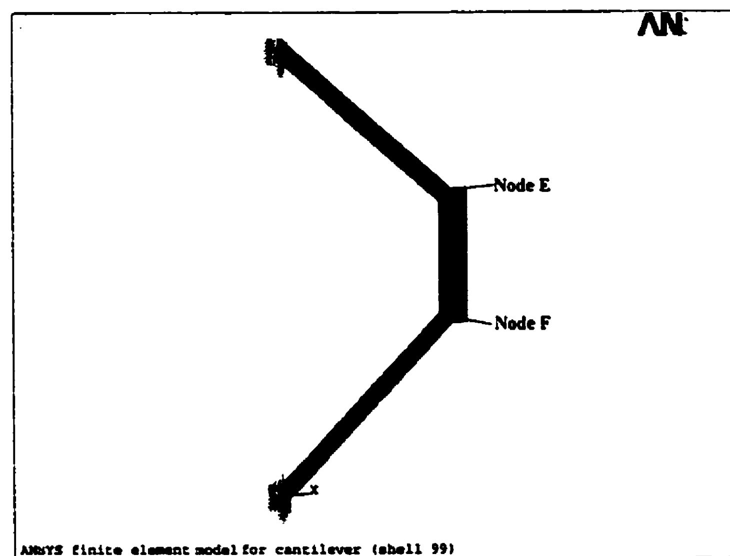

Figure 5.2 ANSYS finite element model for cantilever

Figure 5.3 shows the static analysis of the cantilever at room temperature. The results show the bending of the cantilever because of residual stress. Figure 5.4 shows the modal analysis of the cantilever at room temperature. The above two analyses considered the thermal residual stress. That is, the reference temperature of 460 K was used for the model. If the thermal residual stress was neglected, the modal analysis results are shown in Figure 5.5. Comparing results in Figure 5.4 and 5.5, we can see

there is almost 1 kHz difference for the first resonant frequency. The summary of ANSYS simulation is in Table 5.3.

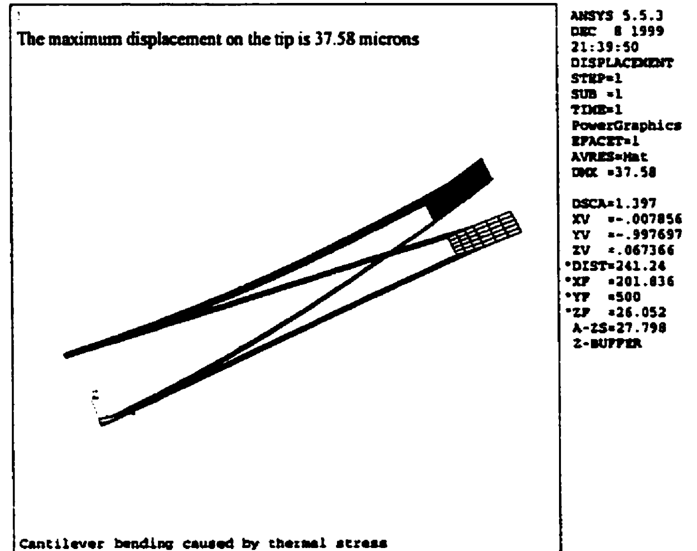

5.3 (a)

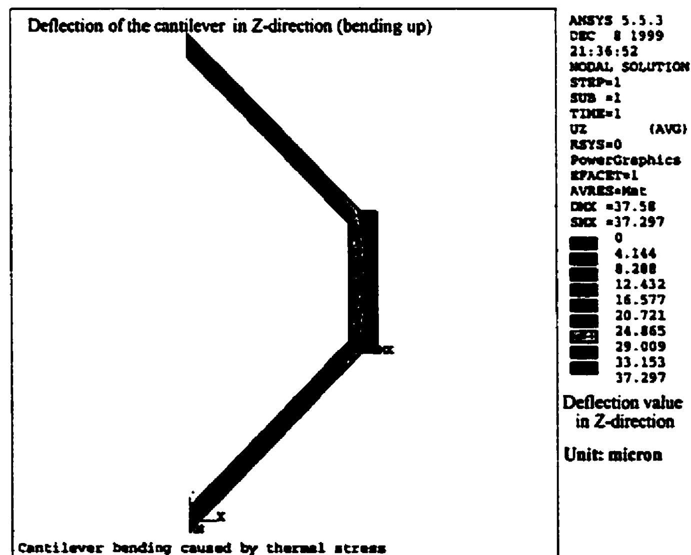

5.3 (b)

Figure 5.3 ANSYS analysis of the cantilever at room temperature due to residual stress

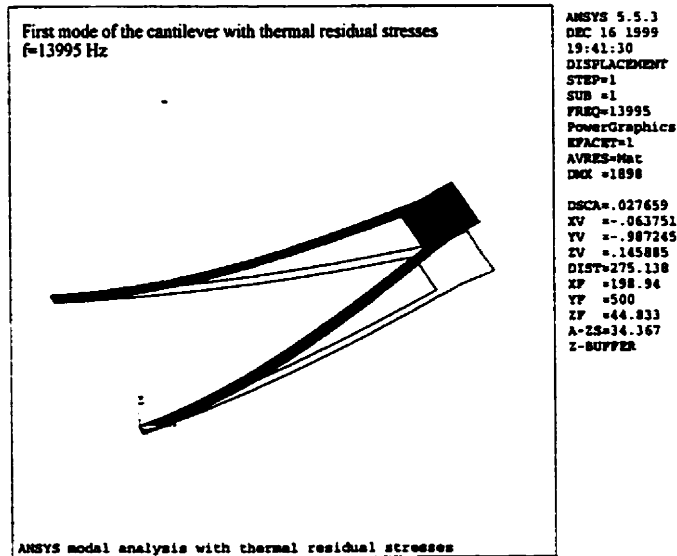

5.4 (a) The first mode of the cantilever with thermal residual stress

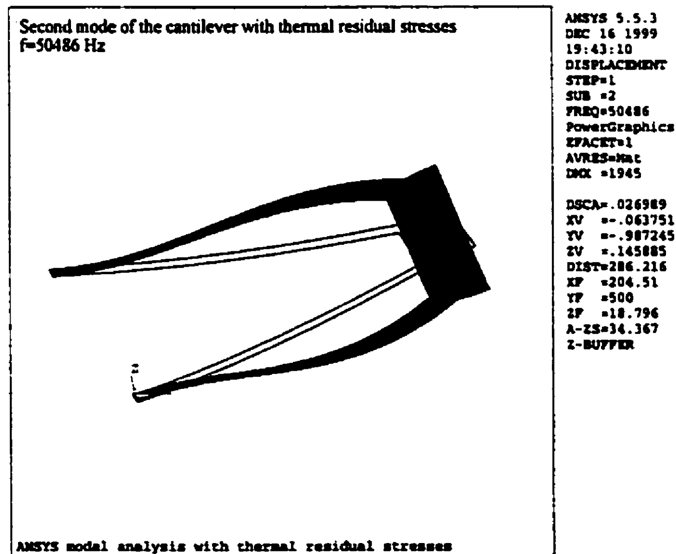

5.4 (b) The second mode of the cantilever with thermal residual stress

Figure 5.4 ANSYS modal analysis of cantilever at room temperature (considering thermal residual stresses)

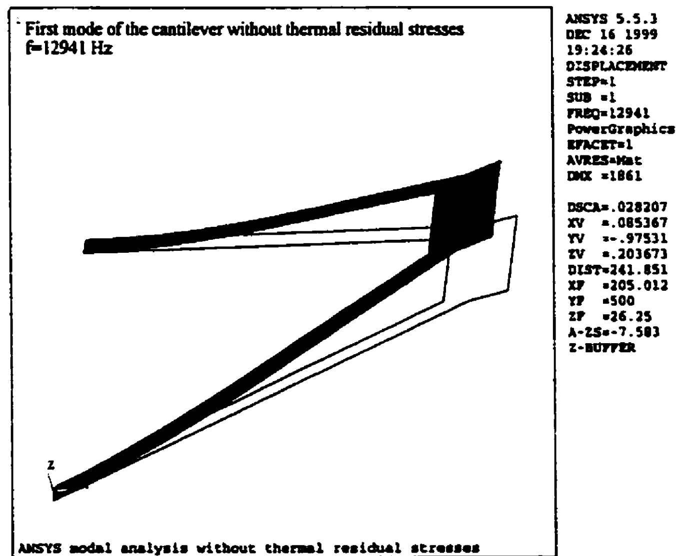

5.5 (a) The first mode of the cantilever without thermal residual stress

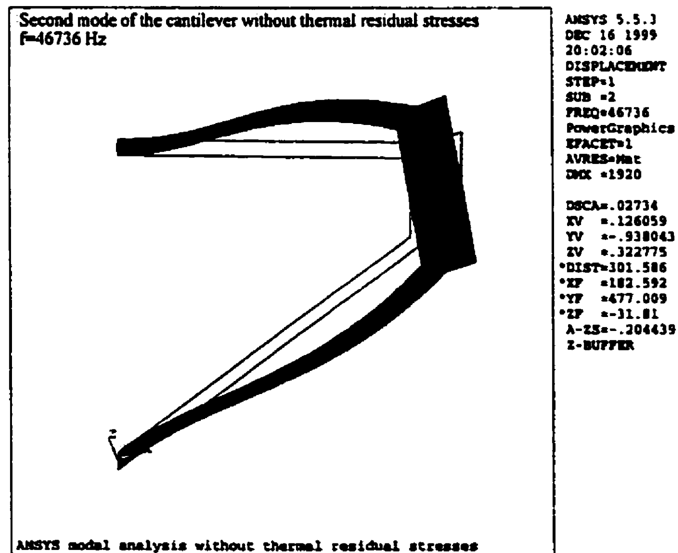

5.5 (b) The second mode of the cantilever without thermal residual stress

Figure 5.5 ANSYS modal analysis of cantilever at room temperature (without thermal residual stresses)

We observed the movement of the cantilever in its second resonant frequency (see Figure 5.4(b)). However, the deflection was so weak that we could not quantitatively record it with our data acquisition system.

Table 5.3 Summary of ANSYS simulations

	Tip deflection (μm)	First resonant frequency (Hz)	Second resonant frequency (Hz)
With thermal stress	37.58	13995	50486
Without thermal stress	0	12941	46736

5.3 The Effect of Geometry on Bending

Since we obtained the material properties and reference temperature from the previous section by means of best fit, geometry effects on the residual deflection could be studied. This modeling would show how the device geometry affected the bending/deflection after the device was released. From our measurement results, the device bending was in the tens of microns range. This is a typical case of large deflection for a CMOS cantilever. If a structure experiences large deformations, its changing geometric configuration can cause the structure to respond nonlinearly. An example would be the fishing rod. Geometric non-linearity is characterized by "large" displacements and/or rotations. The out-of-plane stiffness of a structure can be

significantly affected by the state of in-plane stress in that structure. This coupling between in-plane stress and transverse stiffness, known as stress stiffening, is most pronounced in thin, highly stressed structures, such as cables or membranes. A drumhead, which gains lateral stiffness as it is tightened, would be a common example of a stress-stiffened structure.

In ANSYS, the analysis residual cantilever deflection caused by residual stress is a non-linear thermal stress analysis. The load is the temperature difference. At room temperature, the load on the cantilever was 460 K. We issued the large deflection option to activate nonlinear effects for our cantilever analysis.

ANSYS employs the "Newton-Raphson" method to solve nonlinear problems. In this approach, the load is subdivided into a series of load increments. The load increments can be applied over several load steps.

Before each solution, the Newton-Raphson method evaluates the out-of-balance load vector, which is the difference between the restoring forces (the loads corresponding to the element stresses) and the applied loads. The program then performs a linear solution, using the out-of-balance loads, and checks for convergence. If convergence criteria are not satisfied, the out-of-balance load vector is re-evaluated, the stiffness matrix is updated, and a new solution is obtained. This iterative procedure continues until the problem converges. The program will continue to do equilibrium iterations until the convergence criteria are satisfied or until the maximum number of equilibrium equations is reached.

Our convergence criteria use L2-norm of force (and moment) tolerance of 0.5%, a setting that is appropriate for most cases [124]. An L2-norm check on displacement

with tolerance of 5 % is also used in addition to the force norm check. The check that the displacements are loosely set serves as a double-check on convergence [124]. In order to improve the convergence performance of our analysis, techniques such as tracking convergence graphically, automatic time stepping and line searching were used [124].

The analysis results of geometry effects are shown in Figure 2.7. Three different devices were studied. Each one had a different structure. They consisted of the same material layers as our cantilever. It is shown that the different configurations could produce different residual bending, and the cantilever with 45 degree supporting arms had the smallest tip deflection.

So far, we realized that the residual stress could severely change the cantilever dynamic and static behavior, such as resonant frequency and residual bending. Residual stress effects are common to most surface micromaching devices. Most often, it is very critical to predict these residual stress effects during device design. If we consider the thermal stress is the major part in residual stress, one feasible way to estimate the residual stress effect was discussed in this and the previous sections. The strategy is to use a device with simple geometry to extract material properties and a finite element method to predict the residual stress effect for a device of arbitrary geometry.

5.4 The Effect of Mass on the Resonant Frequency

In order to simulate the possibility of using a cantilever device as a mass/humidity sensor, ANSYS analysis of mass effects on the resonant frequency was conducted. The mass was modeled by the element MASS 21. MASS 21 is a point element having up to six degrees of freedom: translations in the nodal x, y, and z

directions and rotations about the nodal x, y, and z-axes. A different mass and rotational inertia may be assigned to each coordinate direction. The different mass on the cantilever model was realized by changing the real constant of MASS 21. The MASS 21 was placed on the nodes E and F of the cantilever tip to simulate the effect of the connection bars (see Figure 5.2).

Because of the large residual deflection, a prestressed modal analysis following a large-deflection, static, nonlinear and thermal stress analysis was performed in order to calculate the frequencies and mode shapes of a deformed cantilever device. The calculation results are shown in Figure 5.6 and Table 5.4. A mass of 2 ng could cause a 25 Hz frequency shift. In reference [74], the ratio of resonant frequency shift to change in distributed mass is 21.3 Hz/ng for a single CIC (cantilever-in-cantilever) and 8.55 Hz/ng for a double CIC.

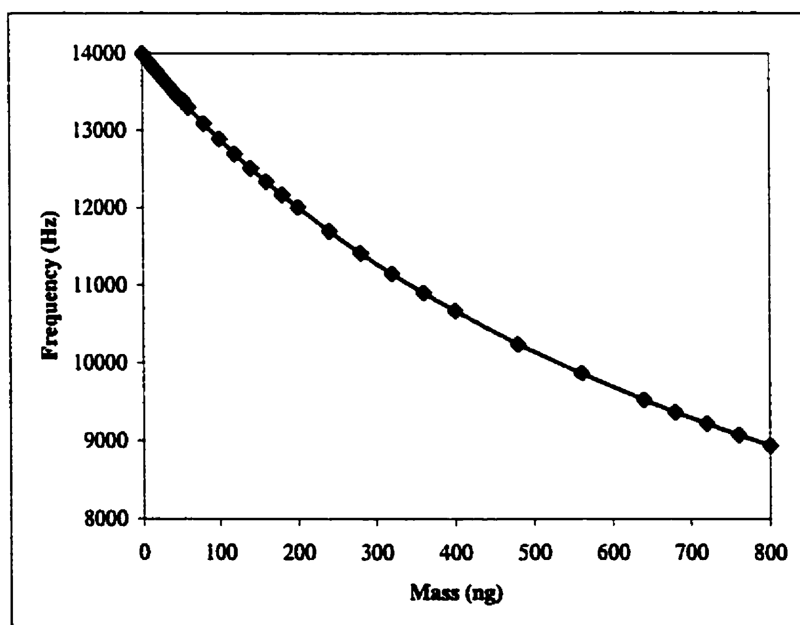

Figure 5.6 ANSYS results of mass effects on resonant frequency

Table 5.4 ANSYS results of mass effects on resonant frequency

Mass *(ng)*	0	0.2	2	10	12	14	16	18	20
Frequency *(Hz)*	13995	13992	13970	13872	13847	13823	13799	13775	13751

5.5 ANSYS Simulation of Band Pass Filter

The band pass filter consisted of two cantilever devices. Their resonant frequencies could be changed by adding element MASS 21 on their tips. Figure 5.7 shows the finite element model for the band pass filter.

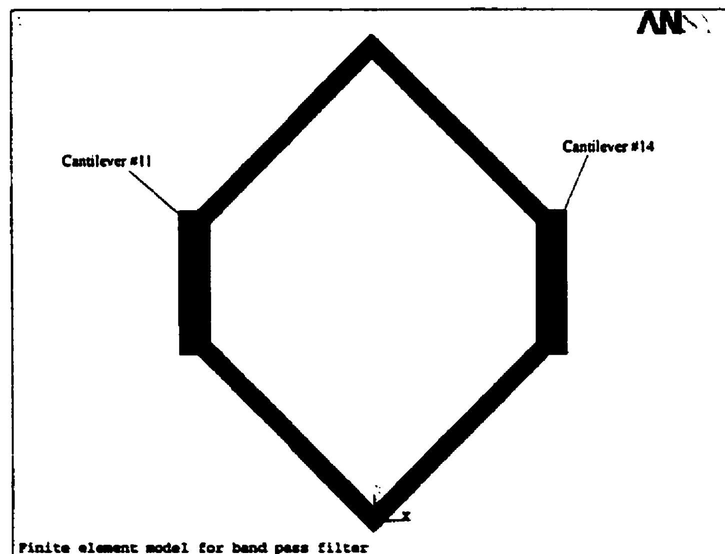

Figure 5.7 Finite element model for the band pass filter

Harmonic response analysis was conducted to model the behavior of the filter. Harmonic response analysis is a technique used to determine the steady-state response of

a linear structure to loads that vary sinusoidally (harmonically) with time. The idea is to calculate the structure's response at several frequencies and obtain a graph of some response quantity (usually displacements) versus frequency. This analysis technique calculates only the steady state, forced vibrations of a structure. The transient vibrations, which occur at the beginning of the excitation, are not accounted for in a harmonic response analysis.

Three harmonic response analysis methods are available: full, reduced, and mode superposition. The reduced method enables you to condense the problem size by using master degrees of freedom (DOF) and reduced matrices [124]. After the displacements at the master DOF have been calculated, the solution can be expanded to the original full DOF set. It is faster and less expensive compared to the full method when you are using the frontal solver [124]. And more important, the prestressing (residual stresses) effects can be included.

Figure 5.8 and Figure 5.9 show the analysis results. Figure 5.8 is the amplitude response of the node on the cantilever tip. Figure 5.9 is the phase response of the same node on the cantilever tip. Table 5.5 shows the simulation results of band pass filter.

Table 5.5 The simulation results of band pass filter

	Cantilever #11	**Cantilever #14**
Measured Resonant Frequency (Hz)	13190	13340
ANSYS Resonant Frequency (Hz)	13200	13420

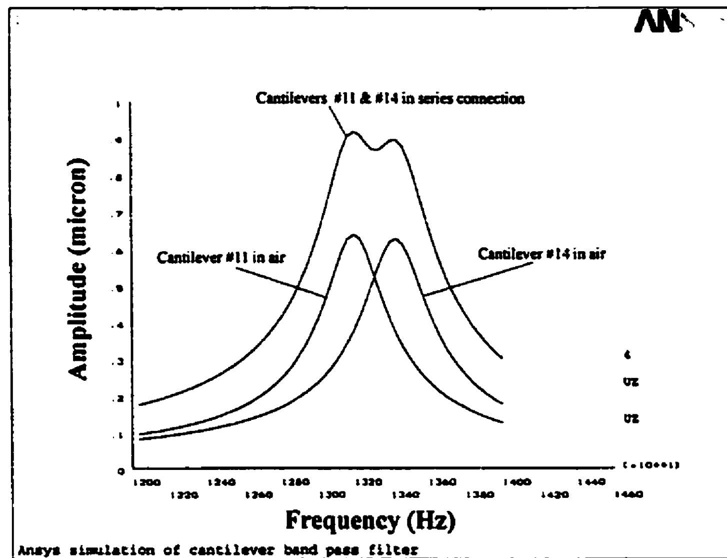

Figure 5.8 The amplitude response of the filter

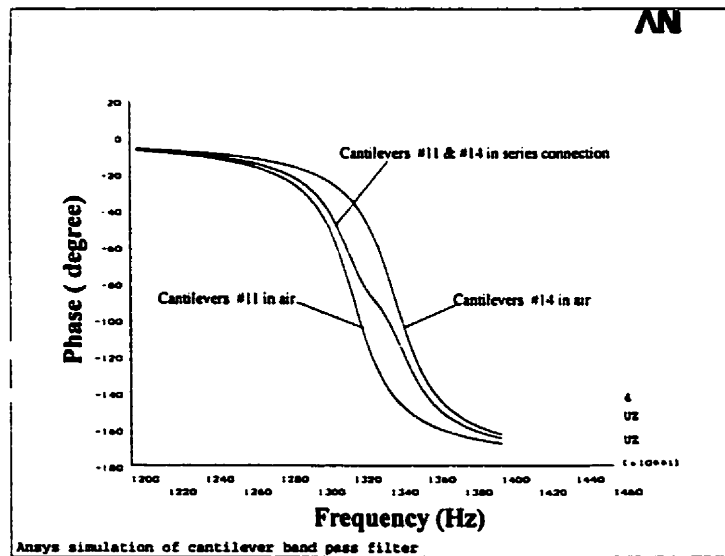

Figure 5.9 The phase response of the filter

5.6 ANSYS Simulation of DC Current Tuning of Resonant Frequency

A DC current produces a force on the cantilever because of its interaction with the magnetic field. Changing the current direction changes the force direction. In our specific ANSYS model, the force created by the DC current is in the z direction. Its magnitude depends on the DC current and magnetic field.

Prestressed modal analysis of a large deflection was carried out to simulate the DC current effects on the resonant frequency. Before doing the modal analysis, a non-linear static analysis of residual thermal stress and the DC force was conducted. In order to improve the convergence performance of our analysis, techniques such as tracking the convergence graphically, automatic time stepping and line search were used, as before.

Figure 5.10 shows the analysis results. The simulation condition is identical with the experiments description in Table 4.1 of Chapter 4. When the DC current is equal to zero, the cantilever bends upwards because of the initial residual (thermal) stress. This bending increases the stiffness of the cantilever. Therefore, the first and second resonant frequencies are increased (see Table 5.3).

In general, DC current tuning of the resonant frequency is due to the initial residual stress and different forces resulted from the different DC currents. In our ANSYS simulation, DC current tuning of the resonant frequency is a typical prestressed non-linear problem [124].

Like the measurement data, the calculated data was non-linear. The resonant frequency is not proportional to the DC current. And also from the simulated and measured results, it is shown that the resonant frequency of the cantilever is easier to be shifting higher than lower for the same amount of DC current.

The difference between them is probably due to the errors in the best-fitted material properties in Table 5.2 (b) for the ANSYS calculation.

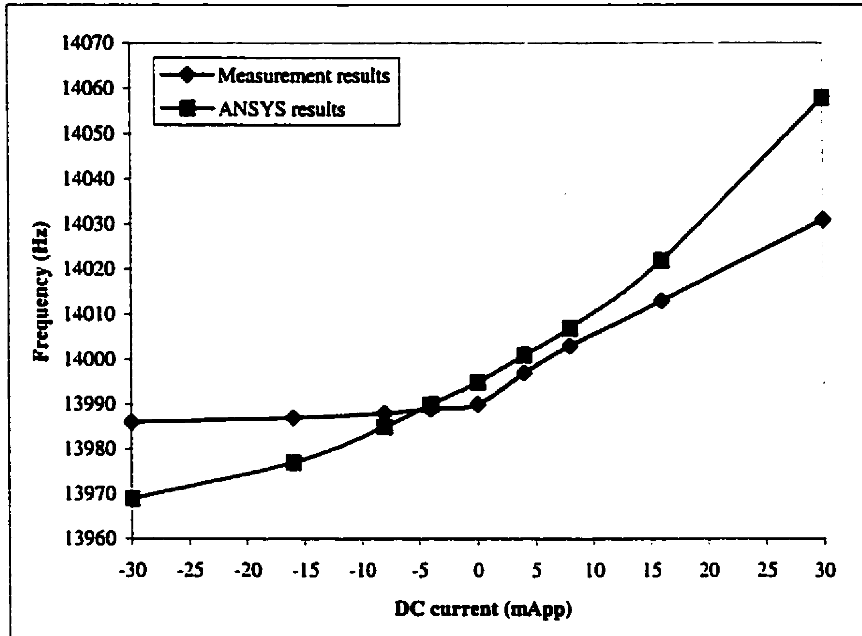

Figure 5.10 ANSYS simulation results of DC current tuning of the resonant frequency in air at 18 Torr

5.7 ANSYS Simulation of Cantilever in Water

The mixing of two or more liquid chemicals in the micro-channels is important for some applications [116,117]. For thin microchannels of 100 μm width or less, the liquids in the microchannel transport under laminar flow. This implies that mixing of two fluids is only possible by diffusion. Researchers in the biochip field have tried different methods to achieve good mixing. Most of the mixer designs are not efficient. Figure 5.11 shows one mixer design from the Stanford University [117]. The liquids from inlets 1 and 2 have to travel a long distance before being properly mixed.

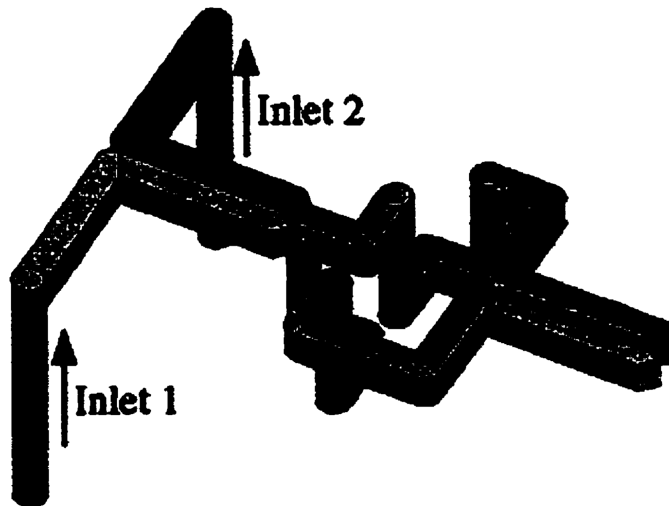

Figure 5.11 Multi-lever laminating mixer

When we characterized the cantilever device in liquids, we found the cantilever had a strong direct stirring/mixing effect of the liquid. It could be a very efficient micromixer. In our test, we found the cantilever could significantly reduce the dye

mixing time in the DI water. However, we lacked sufficient facility to characterize it and to obtain quantitative experiment data.

By means of an ANSYS simulation, we can understand the interaction of the cantilever and liquids. The way the cantilever moves in the water cannot be simply explained by damping. In addition to damping there is an "added mass" effect, because the moving cantilever carries fluid along with it as it moves, effectively increasing the system mass. The result is a lower natural frequency [24].

Acoustics is the study of the generation, propagation, absorption, and reflection of sound pressure waves in a fluid medium. We used the acoustics analysis in ANSYS to simulate the cantilever behavior in water.

An acoustic analysis, available in ANSYS, usually involves modeling the fluid medium and the surrounding structure. Typical quantities of interest are the pressure distribution in the fluid at different frequencies, pressure gradient, particle velocity, the sound pressure level, as well as scattering, diffraction, transmission, radiation, attenuation, and dispersion of acoustic waves. A coupled acoustic analysis takes the fluid-structure interaction into account. The ANSYS program assumes that the fluid is compressible, but allows only relatively small pressure changes with respect to the mean pressure. Also, the fluid is assumed to be non-flowing and inviscid (that is, viscosity causes no dissipative effects). Uniform mean density and mean pressure are assumed, with the pressure solution being the deviation from the mean pressure, not the absolute pressure. All of these assumptions, especially the invisicid assumption, will create some analysis errors. Considering element compatibility between structure element and liquid element, the element SOLID45 was used for modeling the cantilever (Figure 5.12).

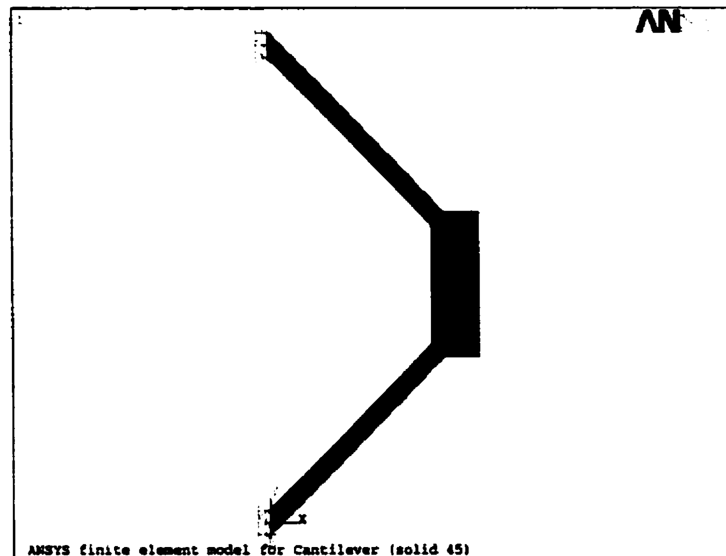

Figure 5.12 ANSYS finite element model for cantilever

SOLID45 is used for the three-dimensional modeling of solid structures. The element is defined by eight nodes having three degrees of freedom at each node, namely, translation in the nodal x, y, and z directions. The element has plasticity, creep, swelling, stress stiffening, large deflection, and large strain capabilities.

FLUID30 is used for modeling the fluid medium and the interface in fluid/structure interaction problems. The element can be used with other 3-D structural elements to perform unsymmetric or damped modal, full harmonic response and full transient method analyses. The element interacting with the structure is interface element FLUID30, otherwise it is non-interface FLUID30. KEYOPT(2) is used to specify the absence or presence of a structure at the interface for FLUID30. The whole model for acoustics analysis is shown in Figure 5.13. The cantilever in this model cannot be seen because the cantilever elements are surrounded the water elements. There are 3297 elements and 51500 nodes in this model.

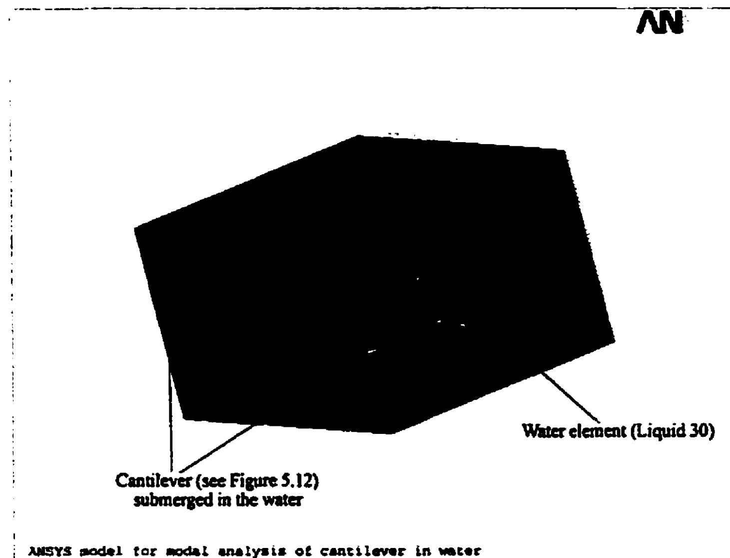

Figure 5.13 ANSYS model for acoustics analysis of cantilever in water

Modal analyses were conducted for the cantilever in vacuum and in water. The results are shown in Figure 5.14 and Table 5.6. The difference of the measured and ANSYS calculated resonant frequency in water and vacuum is mainly caused by the assumption of invisicid for ANSYS acoustics analysis.

In order to easily display the ANSYS results for acoustics analysis, we chose part of the acoustic analysis model (see Figure 5.15). The water elements in the figure have a thickness of 76 μm. That is, the distance between node A and node B is 76 μm. After harmonic response analysis, the z direction displacement of node B on the cantilever tip is shown in Figure 3.16, and average pressure at node A in water is shown in Figure 5.17.

The sharpness of the displacement and pressure curves around 5100 Hz is due to the large frequency step of 50 Hz used in ANSYS simulation.

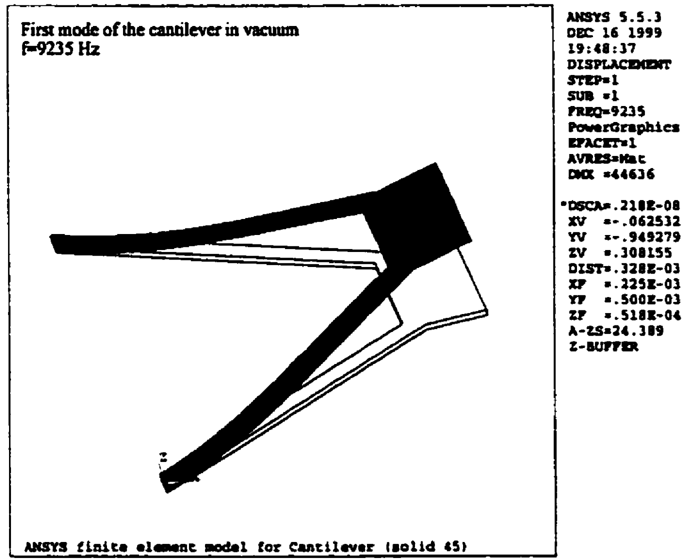

(a) The first mode of the cantilever in vacuum

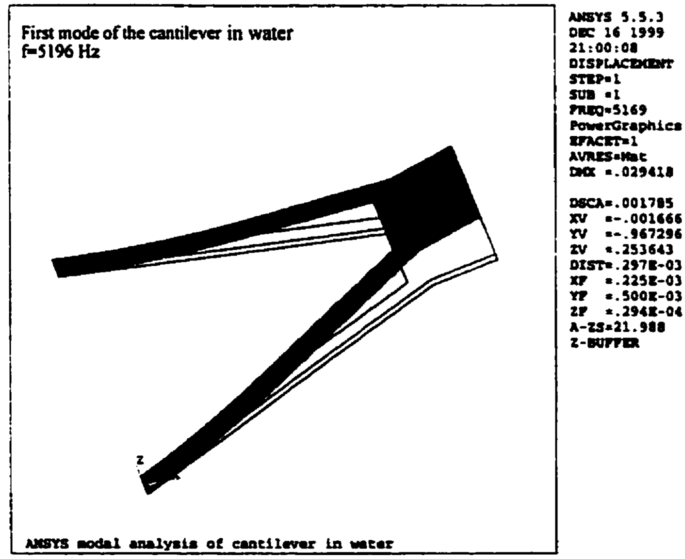

(b) The first mode of the cantilever in water

Figure 5.14 Modal analyses for cantilever in vacuum and in water

Table 5.6 Calculated and measured first resonant frequency for the cantilever in vacuum and in water

	First resonant frequency *(Hz)* *In Vacuum*	**First resonant frequency** *(Hz)* *In DI water*
Measurement	9250	4440
ANSYS	9235	5169

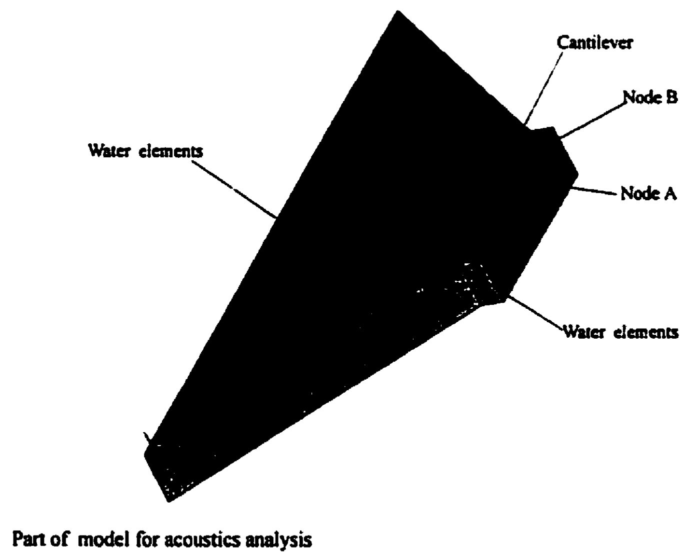

Figure 5.15 Part of acoustics analysis model

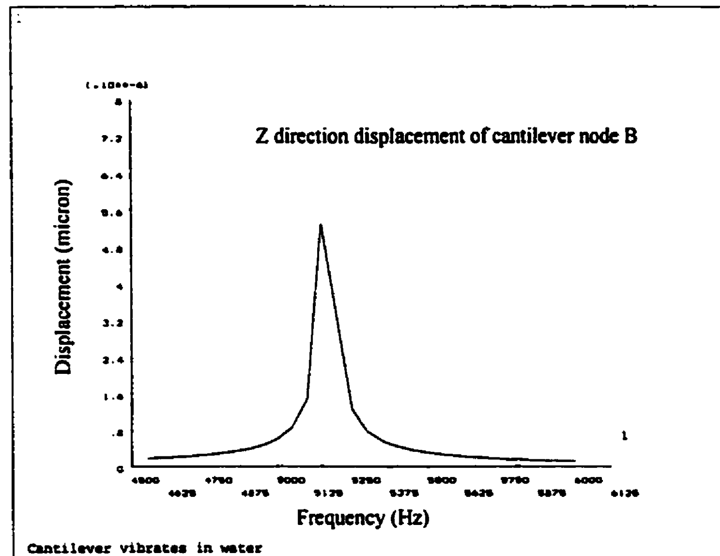

Figure 5.16 Displacement of node B of the cantilever tip in water

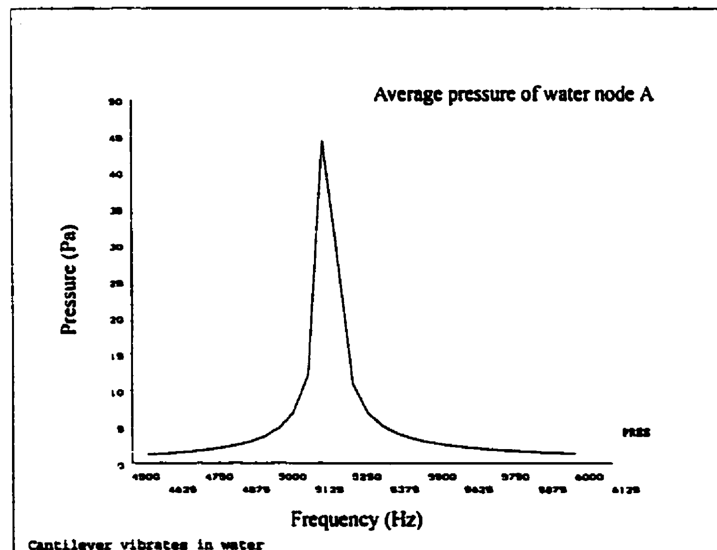

Figure 5.17 Average pressure at node A in water, 76 μm from the cantilever tip

At a frequency of 5150 Hz, close to the first resonant frequency of cantilevers determined by ANSYS, the average pressure distribution in the water is shown in Figure 5.18.

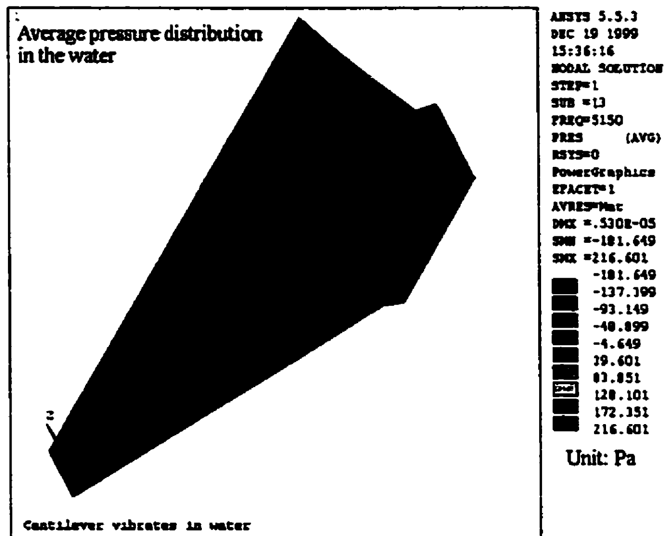

Figure 5.18 Average pressure distribution in water

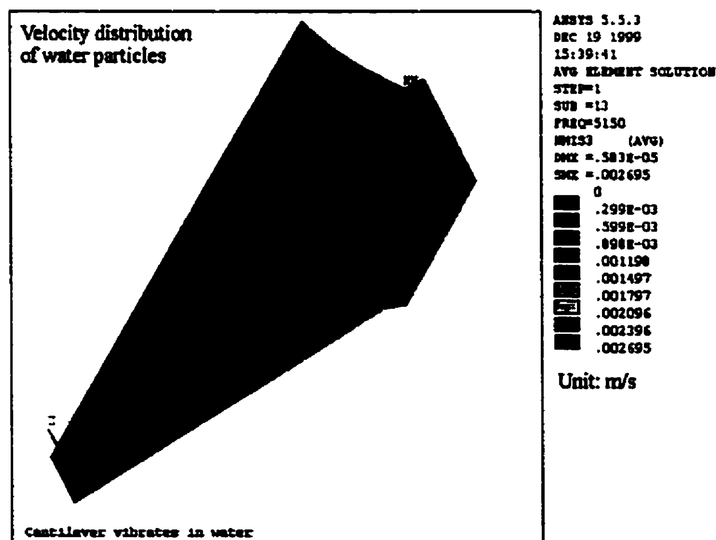

Figure 5.19 Velocity distribution of water particles at a frequency of 5150 Hz

The velocity and displacement distributions of water particles are shown in Figure 5.19 and 5.20 respectively. In the location of 76 μm away from the cantilever tip, the average pressure is about 84 Pa, and the velocity of water particles is about 1497 μm/s.

The ANSYS results show that the cantilever device has a strong mixing effect on water. It force water particles moving in the high speed. Its small size, strong and direct interaction with the liquid makes it an efficient micromixer in the micro-fluidics system.

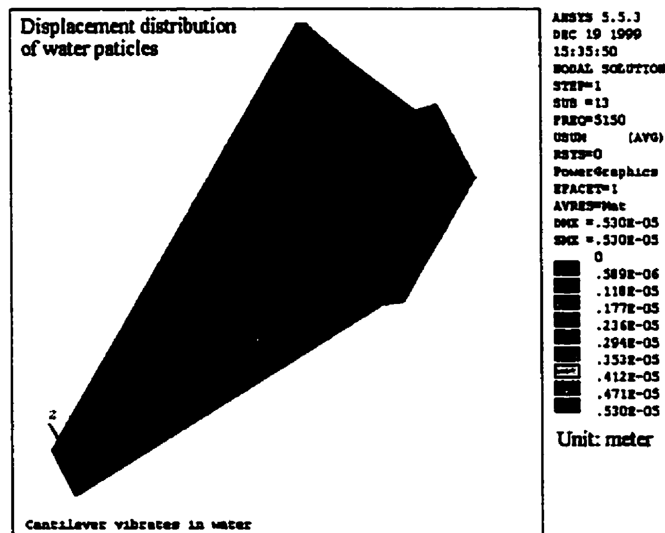

Figure 5.20 Displacement distribution of water particles at a frequency of 5150 Hz

CHAPTER 6

CONCLUSIONS AND FUTURE WORK

A simple CMOS resonant cantilever is designed and fabricated. Design principles and considerations about cantilever arms, releasing the structure, piezoresistors, bonding pads and etch opening are given. The resultant piezoresistor has very large response amplitude.

Combinational silicon etching, which combines the advantages of TMAH anisotropic etching and XeF_2 isotropic etching and significantly reduces the underetching, is proposed and developed. The silicon-doped TMAH anisotropic etching produces excellent results.

Dynamic properties of resonant cantilevers in air, vacuum and liquids are investigated. The changes in the first resonant frequency and response amplitude with pressure, mass, magnetic field, and different viscous liquids are successfully characterized. Possible applications such as liquid viscosity detection, band pass filters, and biochip mixers are demonstrated.

The effects of temperature-dependent residual stress on the device dynamic and static performances are studied. Nonlinear ANSYS simulation results have good agreement with the experimental data. The interaction between water and the cantilever structure is also simulated.

There are a number of things that should be done for future work.

1) Material properties extraction for solving residual bending caused by residual stress. Although we obtained good ANSYS simulation results by using

optimization procedures based on the material data from references [12,104], more specific and accurate material properties of the Mitel 1.5 μm process is still needed for detailed research. As mentioned in Chapter 5, a large number of thermal tests should be done to extract material properties such as reference temperatures and thermal expansion coefficients.

2) Further study of cantilever operation in liquids, which includes more liquid samples test and viscosity calibration. We only studied two liquids at room temperature and found that the resonant frequency of the cantilever decreases with increasing liquid viscosity in this thesis. In order to use a microcantilever as a viscometer, more liquid samples with different viscosities have to be studied at different temperatures to fully understand the relationship between resonant frequency shift and liquid viscosity. Also an easy and reliable calibration technique has to be investigated and developed.

3) Further study of bandpass filters, which includes the design and fabrication of higher frequency filter and/or bandpass filter arrays. In this thesis, we only connected two microcantilevers in series to expand the bandwidth. As part of future work, an array of microcantilevers whose resonant frequencies cover a certain range shall be studied to achieve even wider bandwidth. Furthermore, special design considerations have to be taken to move the microcantilevers into higher frequency domains (GHz) where MEMS bandpass filters (switches) have important applications in modern telecommunications [123].

4) On-chip signal conditioning circuit. The on-chip signal conditioning circuit would consist of a current mirror using the Mitel 1.5 μm process. Other circuits

include an oscillator to produce the actuating current of 5-100 mA, analog-to digital converter for measuring the piezoresistor voltage and resonant frequency detector.

5) On-package actuating magnetic field. The magnetic field of the cantilever is provided by an external magnet, which is bulky compared to the cantilever. Further development of the device should include the development of the magnetic field generator such as electroplating a metal loop or polymer magnet [89].

REFERENCES

[1] H. Baltes, A. Koll and D. Lange, "CMOS MEMS nose - fact or fiction?," *IEEE International Symposium on Industrial Electronics*, vol. 1, Piscataway, NJ, USA, pp. SS152-SS157, 1997.

[2] D. Westberg, O. Paul, G. Andersson and H. Baltes, "CMOS-compatible fluid density sensor," *Journal of Micromechanics and Microengineering*, vol. 7, pp. 253-255, Sept. 1997.

[3] B. Eyre, K. Pister, "Micromechanical resonant magnetic sensor in standard CMOS," *International Conference on Solid State Sensors and Actuators*, vol. 1, Piscataway, NJ, USA, pp. 405-408, 1997.

[4] B. Ghodsian, J. M. Chen, M. Parameswaran, M. Syrzycki, "Towards an integrated sub-nanogram mass measurement system, " *International Conference on Solid State Sensors and Actuators*, vol. 1, Piscataway, NJ, USA, pp. 71-80, 1997.

[5] O. Brand; G. Lenggenhager, H. Baltes, "Influence of air pressure on resonating and thermoelectric microstructures realized with standard IC technologies," *International Electron Devices Meeting*, Piscataway, NJ, USA. pp.195-198, 1993.

[6] T. Boltshauser, M. Schonholzer, O. Brand, H. Baltes, " Resonant humidity sensors using industrial CMOS-technology combined with postprocessing," *Journal of Micromechanics and Microengineering*, vol. 2, pp. 205-207, Sept. 1992.

[7] S. Baglio, L. Latorre, P. Nouet, "Resonant magnetic field microsensors in standard CMOS technology," *IEEE Instrumentation and Measurement Technology Conference*, vol. 1, pp. 452-457, 1999.

[8] O. Brand, M. Hornung, L. Dirk and H. Baltes, "CMOS resonant microsensors, *Proceedings of SPIE The International Society for Optical Engineering,* vol. 3514, Bellingham, WA, USA, pp. 238-250, 1998.

[9] R. T. We and R. S. Muller, "Resonant-microbridge vapor sensor," *IEEE Transaction Electron Devices*, vol. Ed-33, pp.4999-506, April 1986.

[10] R. T. Howe, "Resonant Microsensors," *4th International Conference on Solid-State Sensors and Actuators*, pp. 843-848, 1987.

[11] H. Lakdawala and G. K. Fedder, "Analysis of temperature-dependent residual stress gradients in CMOS micromachined structures," *10th International Conference on Solid State Sensors and Actuators*, Sendai, Japan, pp.345-349, June 1999.

[12] MEMS material database, http://mems.isi.edu/mems/,materials/index.html

[13] G. Zhang, "A lateral capacitive CMOS accelerometer with structural curl compensation," *IEEE International Micro Electro Mechanical Systems Conference*, Orlando, FL, pp.234-236, Jan. 1999.

[14] S. Timoshenko, "Analysis of Bi-metal thermostats," *Journal of Optical Society of America*, vol.11, pp. 233-255, 1925.

[15] D. L. DeVoe, "Modeling and optimal design of piezoelectric cantilever microactuators," *Journal of Microelectromechanical Systems*, vol.6, pp. 24-29, 1997.

[16] M. T. Wu and A. M. Manittatty, "Modeling thermal stresses in thin metallic films and patterned lines," *IEEE International Micro Electro Mechanical Systems Conference*, Vol. 66, pp. 553-558, 1998.

[17] M. Ohring, "The materials science of thin films," Boston : Academic Press,1992.

[18] R. J. Read, E. H. Klaassen and G. T.A. Kovacs, "Thermally and electrically isolated single crystal silicon structures in CMOS technology," *IEEE Electron Device Letters*, vol.15, pp. 399-401, October 1994.

[19] J. T. L Thong, W. K. Choi and C.W. Chong, "TMAH etching of silicon and the interaction of etching parameters," *Senors and Actuators A*, vol.63, pp. 243-249, 1997.

[20] O. Tabata, "pH-controlled TMAH etchants for silicon micromachining," *8th international conference on Solid Sensors and Actuators*, Stockholm, Sweden, pp. 84-86, June 1995.

[21] J. L. Andujar, J. Kasaneva, J. Serra, A. Canillas, C. Roch, J. L. Morenza and E. Bertran, "Effects of r.f. power on optical and electrical properties of plasma-deposited hydrogenated amorphous silicon thin films," *Sensors and Actuators A*, vol. 37-38, pp. 733-736, 1993.

[22] L. M. Landsberger, S. Naseh, M. Kahrizi and M. Paranjape, "On hillocks generated during anisotropic etching of Si in TMAH," *Journal of Microelectromechanical Systems*, Vol.5, pp. 106-116, June 1996

[23] O. Tabata, R.Asahi, H. Funabashi, K. Shimaoka and S. Sugiyama, "Anisotropic etching of silicon in TMAH solutions, " *Sensors and Actuators A*, vol. 34, pp. 51-57, 1993.

[24] R.J. Fritz, "The effect of liquids on the dynamic motions of immersed solids," *Journal of Engineering for Industry*, vol. 81, pp. 167-173, Feb. 1972.

[25] S. Naseh, L.M. Landsberg, M. Paranjape, B. Nikpour, M. Kahrizi, "Release-control structure for post-process release of a micromachined cantilever, " *IEEE Cananadian Conference on Electrical and Computer Engineering*, pp .80-83, 1996.

[26] N. H. Tea, V. Milanovic, C. A. Zincke, J. S. Suehle, M. Gaitan, M. E. Zaghloul and J. Geist, "Hybrid postprocessing etching for CMOS-compatible MEMS," *Journal of Microelectromechanical Systems*, vol. 6, pp. 363-372, Dec. 1997.

[27] K. E. Petersen, "Silicon as a Mechanical Material," *Proceedings of the IEEE*, vol. 70, pp. 420-457, 1982.

[28] S.T. Picraux and P.J. McWhorter, "The Broad Sweep of Integrated Microsystems," *IEEE Spectrum*, vol. 35, no. 12, pp. 24-33, December 1998.

[29] B. Shen, W. Allegretto, Y. Ma, B. Yu, M. Hu, and A.M. Robinson, "Cantilever Micromachined Structures in CMOS Technology with Magnetic Actuation," *Sensors and Materials*, vol. 9, no. 6, pp. 347-362, 1997.

[30] B. Shen, W. Allegretto, M. Hu, and A.M. Robinson, "CMOS Micromachined Cantilever-in-Cantilever Devices with Magnetic Actuation," *IEEE Electron Device Lett*er, vol. 17, no. 7, pp. 372-374, July 1996.

[31] B. Shen, A.M. Robinson, W. Allegretto, Y. Ma, B. Yu, and M. Hu, "Magnetically Actuated CMOS Micromachined Cantilever-in-Cantilever Devices," *IEEE Canadian Conference Electrical and Computer Engineering.*, pp. 84-87, Calgary, May 1996.

[32] A. Gieles, "Subminiature silicon pressure transducer," *IEEE International Solid State Circuits Conference*, Philadelphia, pp. 108-109, 1969.

[33] L. Roylance, J. Angell, "A batch-fabricated silicon accelerometer," *IEEE Trans. on Electron Devices*, vol. 26, pp. 1911-1914, 1979.

[34] K. Gabriel, W. Trimmer, M. Mehregany, "Micro gears and turbines etched from silicon," *International Conference on Solid-State Sensors and Actuators*, Tokyo, pp. 853-856, 1987.

[35] L. Fan, Y. Tai, R. Muller, "Integrated movable micromechanical structures for sensors and actuators," *IEEE Transaction on Electron Devices*, vol. 35, no. 6, pp. 724-730, 1980.

[36] R. Howe, R. Muller, "Stress in polycrystalline and amorphous silicon thin films," *Journal of Applied. Physics*, vol. 54, pp. 4674-4675, 1983.

[37] K. Bean, "Anisotropic etching of silicon," *IEEE Transaction on Electron Devices*, vol. 25, pp. 1185-1193, 1978.

[38] H. Waggener, "Electrochemically controlled thinning of silicon," *Bell Systems Technical Journal*, vol. 49, no. 3, p. 473, 1970.

[39] M. Parameswaran, H. Baltes, L. Ristic, A. Dhaded, A. Robinson, "A new approach for the fabrication of micromechanical structures," *Sensors and Actuators A*, vol. 19, pp. 289-307, 1989.

[40] R. Cavicchi, J. Suehle, P. Chaparala, K. Kreider, M. Gaitan, S. Semancik, "Micro-hotplate gas sensor," *Solid State Sensor and Actuator Workshop*, Hilton Head, pp. 53-56, 1994.

[41] E. Yoon, K. Wise, "An integrated mass flow sensor with on-chip CMOS interface circuitry," *IEEE Transaction on Electron Devices*, pp. 1376-1386, 1992.

[42] D. Moser, R. Lenggenhager, H. Baltes, "Silicon gas flow sensors using industrial CMOS and bipolar IC technology," *Sensors and Actuators A*, vol. 25-27, pp. 577-581, 1991.

[43] H. Kim and K. Chun, "Integrated MEMS for Pressure Transponder," *Ninth International Conference on Solid-State Sensors and Actuators*, Chicago, pp. 1011-1014, June 1997.

[44] M.F. Miller, M.G. Allen, E. Arkilic, K.S. Breuer, and M.A. Schmidt, "Fabry-Perot Pressure Sensor Arrays for Imaging Surface Pressure Distributions," *Ninth International Conference on Solid-State Sensors and Actuators*, Chicago, pp. 1469-1472, June 1997.

[45] J.M. Rabaey, *Digital Integrated Circuits: A Design Perspective*, Prentice-Hall, New Jersey, pp. 2-4, 1996.

[46] A. Reismann, M. Berkenblit, S.A. Chan, F.B. Kaufman, and D.C. Green, "The controlled etching of silicon in catalyzed ethylenediamine-pyrocatechol-water solutions," *Journal of Electrochemical Society*, vol. 126, pp. 1406-1415, 1979.

[47] M. Paranjape, "Vertical Hall Magnetic Field Microsensor Development and Implementation in CMOS Technology," PhD Thesis, University of Alberta, Canada, 1993.

[48] R. Lenggenhager, D. Jaeggi, P. Malcovati, H. Duran, H. Baltes, E. Doering, "CMOS membrane infrared sensors and improved TMAHW etchant," *International Electron Devices Meeting*, San Francisco, pp. 531-534, 1994.

[49] D. Moser, R. Lenggenhager, G. Wachutka, H. Baltes, "Fabrication and modeling of CMOS microbridge gas flow sensors," *Sensors and Actuators B*, vol. 6, pp. 165-169, 1992.

[50] D. Jaeggi, H. Baltes, D. Moser, "Thermoelectric AC power sensor by CMOS technology," *IEEE Electron Device Letters*, vol. 13, pp. 366-368, 1992.

[51] D. Moser, O. Brand, H. Baltes, "A CMOS compatible thermally excited silicon oxide beam resonator with aluminum mirror," *Sixth International Conference on Solid-State Sensors and Actuators*, San Francisco, pp. 547-550, 1991.

[52] R. Reay, E. Klaassen, G. Kovacs, "Thermally and electrically isolated single crystal silicon structures in CMOS technology," *IEEE Electron Device Letters*, no. 15, pp. 399-401, 1994.

[53] W.D. Callister, *Materials Science and Engineering*, John Wiley & Sons, pp. 27-49, 1984.

[54] E.D. Palik, V.M. Bermudez, O.J. Glembocki, "Ellipsometric study of orientation-dependent etching of silicon in aqueous KOH," *Journal of the Electrochemical Society*. vol. 132, no 4, pp. 871-884, 1985.

[55] H Seidel, L. Csepregi, A. Heuberger, H. Baumgaertel, "Anisotropic etching of crystalline silicon in alkaline solutions," *Journal of the Electrochemical Society*, vol. 137, no. 11, pp. 3612-3626, 1990.

[56] ANSYS on line manuals release 5.5, Swanson Analysis System, Inc., 1998.

[57] C. Oezdemir, J. Smith, "Micromachining of silicon," *Sixth International Conference on Solid-State Sensors and Actuators*, San Francisco, San Francisco, pp. 132-135, 1991.

[58] A. Bard, L. Faulkner, *Electrochemical Methods: Fundamentals and Applications*, John Wiley, New York, pp. 633-636, 1980.

[59] B. Kloeck, S. Collins, N. de Rooij, R. Smith, "Study of electrochemical etch-stop for high-precision thickness control of silicon membranes," *IEEE Transactions on Electron Devices*, vol. 36, no. 4, pp. 663-669, 1989.

[60] K.J. Gabriel, "Scanning the Technology," *Proceeding of IEEE*, vol. 86, no. 8, pp. 1534-1535, August 1998.

[61] U. Schnakenberg, W. Benecke, B. Loechel, S. Ullerich, and P. Lange, "NH_4OH based etchants for silicon micromachining: influence of additives and stability of passivation layers," *Sensors and Actuators A*, vol. 25-27, pp. 1-7, 1991.

[62] M. Gajda, H. Ahmed, J. Shaw, A. Putnis, "Anisotropic etching of silicon in hydrazine," *Sensors and Actuators A*, vol. 40, pp. 227-236, 1994.

[63] R. Finne, D. Klein "A water-amine complexing agent system for etching silicon," *Journal of the Electrochemical Society.*, vol. 14, pp. 965-970, 1967.

[64] Y. Ma, A.M. Robinson, W. Allegretto, R.P.W. Lawson and T. Zhou "Static and dynamic characterization of magnetically actuated CMOS-micromachined cantilever-in-cantilever devices," *Canadian Journal of Physics*, vol. 76, pp. 747-758, 1998.

[65] F.I. Chang, R. Yeh, G. Lin, P.B. Chu, E. Hoffman, E.J.J. Kruglick, and K.S.J. Pister, "Gas-phase Silicon Micromachining with Xenon Difluoride," *Symposium on Microelectronic structures and MEM devices*, pp. 117-128, October 1995.

[66] K.B. Brown, W. Allegretto, F. Vermeulen, and A.M. Robinson, "Cantilever-in-Cantilever Micro-Structures for Pressure and Magnetic Field Measurement," *Symposium on Microelectronics R&D Can. (TEXPO '98)*, Ottawa, Canada, June 25-26, 1998.

[67] M. Spacek, K.B. Brown, Y. Ma, A.M. Robinson, R.P.W. Lawson, and W.Allegretto, "CMOS Cantilever Microstructures As Thin Film Deposition Monitors," *IEEE Can. Conf. Electrical and Computer Engineering*, Edmonton, May 1999.

[68] U. Schakenberg, W. Benecke, P. Lange, "TMAHW etchants for silicon micromachining," *Sixth International Conference on Solid-State Sensors and Actuators*, San Francisco, San Francisco, pp. 815-818, 1991.

[69] E. Palik, O. Glembocki, I. Heard, P. Burno, L. Tenerz, "Etching roughness for (100) silicon surfaces in aqueous KOH," *Journal of Applied Physics*, vol. 70, no. 6, pp. 3291-3300, 1991.

[70] S. Campbell, K. Cooper, L. Dixon, R. Earwaker, S. Port, and D. Schiffrin, "Inhibition of pyramid formation in the etching of Si p(100) in aqueous potassium hydroxide isopropanol," *Journal of Micromechanics and Microengineering*, vol. 5, pp. 209-218, 1995.

[71] CRC Handbook of Chemistry and Physics, 66th edition, Chemical Rubber Co., Boca Raton, 1985.

[72] B. Shen, "CMOS Actuators," PhD Thesis, University of Alberta, Canada, 1996.

[73] Y. Ma, "Magnetically Actuated CMOS Micromachined CIC Devices," M.Sc. Thesis, University of Alberta, Canada, 1997.

[74] Keith Brown, " Gas pressure Measurements with cantilever-in cantilever microstructures," M.Sc. Thesis, University of Alberta, 1999

[75] G.T. Kovacs, N.I. Maluf, and K.E. Petersen, "Bulk Micromachining of Silicon," *Proceeding of IEEE*, vol. 86, no. 8, pp. 1536-1551, August 1998.

[76] J.M. Bustillo, R.T. Howe, and R.S. Muller, "Surface Micromachining for Microelectromechanical Systems," *Proceeding of IEEE*, vol. 86, no. 8, pp. 1552-1574, August 1998.

[77] S. Middelhoek, S. Audet, *Silicon Sensors*, Academic Press, San Diego, 1989.

[78] R. Jaeger, *Introduction to Microelectronic Fabrication*, Addison-Wesley, Reading, MA, pp.136-138, 1990.

[79] R.H. Grace, "Automotive Applications of Microelectromechanical Systems," *Proceeding of Sensors Exposition*, Boston, pp. 67-74, May 16-18, 1995.

[80] M. Esashi, S. Sugiyama, K. Ikeda, Y. Wang, and H. Miyashita, "Vacuum-Sealed Silicon Micromachined Pressure Sensors," *Proceeding of IEEE*, vol. 86, no. 8, pp. 1627-1639, August 1998.

[81] H. Baltes, O. Paul, and O. Brand, "Micromachined Thermally Based CMOS Microsensors," *Proceeding of IEEE*, vol. 86, no. 8, pp. 1660-1678, August 1998.

[82] D.S. Eddy and D.R. Sparks, "Application of MEMS Technology in Automotive Sensors and Actuators," *Proc. IEEE*, vol. 86, no. 8, pp. 1747-1755, August 1998.

[83] H. Baltes, D. Lange, and A. Koll, "The Electronic Nose of Lilliput," *IEEE Spectrum*, vol. 35, no. 9, pp. 35-38, September 1998.

[84] B. van Drieenhuizen, R Wolffenbuttel, "Integrated electrostatic RMS-to-DC converter using IC-compatible surface micromachining," *International Conference on Solid-State Sensors and Actuators*, Stockholm, pp. 130-133, 1995.

[85] A. Dimarogonas, *Vibration for Engineers*, 2nd ed., Prentice-Hall, New Jersey, 1996.

[86] C. Gui, R. Legtenberg, H.A.C. Tilmans, J.H.J. Fluitman, and M. Elmenspoek, "Nonlinearity and Hysteresis of Resonant Strain Gauges," *Journal of Microelectromechanical Systems*, vol. 7, no. 1, pp. 122-127, March 1998.

[87] H.A.C. Tilmans and R. Legtenberg, "Electrostatically driven vacuum-encapsulated polysilicon resonators. Part II. Theory and performance," *Sensors and Actuators A*, vol. 45, pp. 67-84, 1994.

[88] J. Fraden, *Handbook of Modern Sensors: Physics, Designs, and Applications*, 2nd ed., Springer-Verlag, New York, 1996.

[89] C.H. Ahn and M.G. Allen, "Micromachined Planar Inductors on Silicon Wafers for MEMS Applications, " *IEEE Transaction*, vol. 45, no. 6, pp. 866-876, December 1997

[90] A.V. Chavan and K.D. Wise, "A Batch-Processed Vacuum-Sealed Capacitive Pressure Sensor," *Ninth International Conference on Solid-State Sensors and Actuators*, Chicago, pp. 1449-1452, June 1997.

[91] A. Berman, *Total Pressure Measurements in Vacuum Technology*, Academic Press, Orlando, 1985.

[92] L. Carpenter, *Vacuum Technology, An Introduction*, American Elsevier, New York, pp. 49-55, 1970.

[93] J.C. Greenwood, "Etched silicon vibrating sensor," *Journal of Physics*, vol. 17, pp. 650-652, 1984.

[94] Y. Kawamura, K. Sato, T. Terasawa, S. Tanaka, "Si cantilever oscillator as a vacuum sensor," *International Conference on Solid-State Sensors and Actuators*, Tokyo, pp. 283-286, 1987.

[95] E. Popov, *Introduction to Mechanics of Solids*, Prentice Hall, Englewood Cliffs

[96] L. Ristic, *Sensor Technology and Devices*, Artech House, Boston, 1994.

[97] D. Teegarden, G. Lorenz, and R. Neul, "How to Model and Simulate Microgyroscope Systems," *IEEE Spectrum*, vol. 35, no. 7, pp. 67, July 1998.

[98] H. Fujita, "Microactuators and Micromachines," *Proceeding of IEEE*, vol. 86, no. 8, pp. 1721-1732, August 1998.

[99] H. Baltes, "Future of IC Microtransducers," *Sensors and Actuators A*, vol. 56, pp. 179-192, 1996.

[100] A. S. Saada, *Elasticity: Theory and Applications*, Pergamon Press, Inc, New York, 1974

[101] D.A. Koester, K.W. Markus, and M.D. Walters, "MEMS: Small Machines for the Microelectronics Age," *Computer*, vol. 29, pp. 93-94, January 1996.

[102] A. van Herwaarden, P. Sarro, H. Meijer, "Integrated Vacuum Sensor," *Sensors and Actuators A*, vol. 8, pp. 187-196, 1985.

[103] R. Rakoz, "Thermal Characterization of a Cantilever-in-Cantilever Microstructure," Internal Paper: Micromachining Applications and Development Lab, University of Alberta, Canada, 1998.

[104] Marc Madou, *Fundamentals of Microfabrication*, CRC press, New York, 1997

[105] B. Shen, A.M. Robinson, W. Allegretto, Y. Ma, B. Yu, and M. Hu, "A Magnetically Actuated Cantilever-in-Cantilever Micromachined Device," *Symposium on Microelectronics R & D (TEXPO '96)*, Ottawa, Canada, June 17-19, 1996.

[106] K.B. Brown, W. Allegretto, F.E. Vermeulen, R.P.W. Lawson, and A.M. Robinson, "Cantilever-in-Cantilever Micromachined Pressure Sensors Fabricated in CMOS Technology," *IEEE Canadian Conference on Electrical and Computer Engineering*, Edmonton, May 1999.

[107] S.G. Adams, F.M. Bertsch, K.A. Shaw, and N.C. MacDonald, "Independent Tuning of Linear and Nonlinear Stiffness Coefficients," *Journal of Microelectromechanical Systems*, vol. 7, no. 2, pp. 172-180, June 1998.

[108] Y. Onuma and K. Kamimura, "Piezoresistive Elements of Polycrystalline Semiconductor Thin Films," *Sensors and Actuators A*, vol. 13, pp. 71-77, 1988.

[109] P.B. Chu, J.T. Chen, R. Yeh, G. Lin, J.C. Huang, B.A. Warneke, and K.S.J. Pister, "Controlled Pulse-Etching with Xenon Difluoride," *Ninth International Conference on Solid-State Sensors and Actuators*, Chicago, pp. 665-668, June 1997.

[110] R. Toda, K. Minami, and M. Esashi, "Thin Beam Bulk Micromachining Based on RIE and Xenon Difluoride Silicon Etching," *Ninth International Conference on Solid-State Sensors and Actuators*, Chicago, pp. 671-674, June 1997.

[111] Canadian Microelectronics Corporation, An Introduction to Micromachining: Results of Projects Using Mitel's 1.5-micron CMOS Technology to Develop a Canadian MEMS Process, Report IC95-08, Queen's University, Canada, 1995.

[112] S. Timoshenko and S. Woinowsky-Krieger, *Theory of Plates and Shells*, McGraw-Hill, New York, 1959.

[113] D. J. Inman, *Engineering Vibration*, Prentice-Hall, New Jersey, pp. 378-381, 1996.

[114] M. Garbuny, *Optical Physics*, Academic Press, Inc., New York, pp. 270, 1965.

[115] I. W. T. Chan, K.B. Brown, R.P.W. Lawson, A.M. Robinson, Y. Ma, and D. Strembicke, "Gas Phase Pulse Etching of Silicon for MEMS with Xenon Difluoride," *IEEE Canadian Conference on ELectrical and Computer Engineering*, Edmonton, May 1999.

[116] J. Harrison and A. Berg, Micro Total Analysis Systems'98, Banff, Canada, 1998

[117] D. Jaeggi, N. Mourlas *et al.*, "Characterization and simulation of microfluidic devices," *http://tranceducers.stanford.edu/stl/projects/fluidic-charact.html*

[118] E. Klaassen, R. J. Reay and G. Kovacs, "Diode-based thermal r.m.s. converter with on-chip circuitry fabricated using CMOS technology," *Sensors and Actuators* A, vol. 52, pp.33-40, 1996.

[119] http://www.symyx.com/

[120] O. Brand, J. M. English, S. A. Bidstrup and M. G. Allen, "Micromachined viscosity sensor for real-time polymerization monitoring," *Ninth International Conference on Solid-State Sensors and Actuators,* Chicago, pp.121-124, June 16-19, 1997

[121] D. Strembick, A.M. Robinson, F.E.Vermeulen, M. Seto and K. Brown, "Humidity measurement using resonating CMOS microcantilever structures," *IEEE Canadian Conference on Electrical and Computer Engineering*, Edmonton, pp. 1658-1661, May 9-12, 1999

[122] Y. Ma A. M. Robinson, R. P. W. Lawson, K. Brown, D. Strembicke, W. Allegretto, and T. Zhou, "Measuring the Deflection of CMOS Micromachined Cantilever Devices using a Piezoresistive Sensor," *Canadian Journal of Electrical and Computer Engineering, Vol. 25, No.1, pp.3-7, January 2000.*

[123] J. J. Yao and M. F. Chang, "A surface micromachined miniature switch for telecommunications applications with signal frequencies from DC up to 4 GHz," *Eighth International Conference on Solid-State Sensors and Actuators,* Stockholm, Sweden, pp. 384-387, June 1995.

[124] G. Zhang," A lateral capacitive CMOS accelerometer with structural curl compensation," *IEEE International Micro Electro Mechanical Systems Conference*, Orlando, FL, pp.354-359, Jan. 1999.

Appendix A

The Preparation of the TMAH Etch Bath

1. Add 1600 mL deionized water with 400 mL of 25 wt.% TMAH to make 2 Liters of 5 wt.% TMAH solution.

2. Add 88 grams of silicic acid into the solution.

3. Pour the mixture into the beaker with a condenser (Figure 3.13), and heat to 80^0C under high stirring.

4. Keep the mixture at 80^0C for 3-4 hours, and measure the pH value of the solution. If the pH value is larger than 13, add 1 gram of silicic acid until the pH value is less than 13.

5. Turn the heater off. Leave the stirrer on. Keep the solution in the beaker overnight (12-24 hours).

6. Heat the solution to 80^0C. Turn on the stirrer. Add 6 grams of potassium persulfate into the solution. Make sure the mixture is clear.

7. Load the chip and etch it for 35 minutes, remove the chip and rinse it in DI water.

8. Inspect the chip. Normally 35 minutes is enough for cantilever arm release. If longer etching is needed, add 10 ml 25% TMAH and 3 grams potassium persulfate.

9. Repeat step 8 until complete etching is done.

Appendix B

Input File for Cantilever ANSYS Simulation

This is the input file for ANSYS simulation of DC current tuning of resonant frequency. The finite element model for the cantilever including element type, material properties and boundary conditions has been built. Other analyses can be realized by changing the analysis type and adding certain loading conditions.

```
/TITLE, THE EFFECTS OF DC
CURRENT ON THE CANTILEVER'S
NATURAL FREQUENCY
/PREP7

!Define Keypoints
K,3,0,25,,
K,4,350,375,,
K,5,375,350,,
K,6,0,975,,
K,8,350,625,,
K,9,375,650,,
K,10,410,650,,
K,7,410,350,,
K,1,0,1025,,
K,2,0,-25,,

!Define areas
FLST,2,4,3
FITEM,2,2
FITEM,2,5
FITEM,2,4

FITEM,2,3
A,P51X
FLST,2,6,3
FITEM,2,5
FITEM,2,7
FITEM,2,10
FITEM,2,9
FITEM,2,8
FITEM,2,4
A,P51X
FLST,2,4,3
FITEM,2,8
FITEM,2,9
FITEM,2,1
FITEM,2,6
A,P51X

!define elements and material properties
ET,1,SHELL99
R,1
RMODIF,1,1,8,0,0,0,0,
RMODIF,1,13,1,0,1,2,0,0.3,
RMODIF,1,19,1,0,0.8,3,0,0.8,
RMODIF,1,25,1,0,0.8,3,0,0.8,
RMODIF,1,31,1,0,0.5,4,0,0.5,
UIMP,1,EX, , ,0.460e8,
UIMP,1,DENS, , ,0.22e-11,
UIMP,1,ALPX, , ,0.4e-6,
UIMP,1,NUXY, , ,0.17,
UIMP,2,EX, , ,1.5e+8,
UIMP,2,DENS, , ,0.232e-11,
UIMP,2,ALPX, , ,2.4e-6,
UIMP,2,NUXY, , ,0.23,
UIMP,3,EX, , ,0.6e8,
UIMP,3,DENS, , ,0.27e-11,
UIMP,3,ALPX, , ,0.33e-4,
UIMP,3,NUXY, , ,0.33,
UIMP,4,EX, , ,0.13e9,  !0.14e9
UIMP,4,DENS, , ,0.3187e-11,
UIMP,4,ALPX, , ,0.366e-5,
UIMP,4,NUXY, , ,0.3,

!Define meshing condition
TYPE,1,
MAT,1,
REAL,1,
ESYS,0,
```

```
ESHAPE,2,0

FLST,2,2,4,ORDE,2
FITEM,2,3
FITEM,2,10
LESIZE,P51X, , ,20,0.5,

FLST,2,2,4,ORDE,2
FITEM,2,1
FITEM,2,12
LESIZE,P51X, , ,20,2,

FLST,2,6,4,ORDE,6
FITEM,2,2
FITEM,2,4
FITEM,2,-5
FITEM,2,7
FITEM,2,-8
FITEM,2,11
LESIZE,P51X, , ,3,1,

FLST,2,2,4,ORDE,2
FITEM,2,6
FITEM,2,9
LESIZE,P51X, , ,5,1,

!Meshing
FLST,5,2,5,ORDE,2
FITEM,5,1
FITEM,5,3
CM,_Y,AREA
ASEL, , , ,P51X
CM,_Y1,AREA
CHKMSH,'AREA'
CMSEL,S,_Y
AMESH,_Y1
CMDEL,_Y
CMDEL,_Y1
CMDEL,_Y2

FLST,2,2,4,ORDE,2
FITEM,2,7
FITEM,2,-8
LCCAT,P51X

FLST,2,2,4,ORDE,2
FITEM,2,2
FITEM,2,5
LCCAT,P51X
CM,_Y,AREA
ASEL, , , ,      2
CM,_Y1,AREA
CHKMSH,'AREA'
CMSEL,S,_Y
AMESH,_Y1
CMDEL,_Y
CMDEL,_Y1
CMDEL,_Y2

CM,_Y,LINE
*SET,_Z1,LSINQR(0,13)
LSEL,R,LCCA
*SET,_Z2,LSINQR(0,13)
LDEL,ALL
*SET,_Z3,_Z1-_Z2
*IF,_Z3,NE,0,THEN
CMSEL,S,_Y
CMDEL,_Y
*ENDIF

NUMMRG,ALL, , ,
NUMCMP,ALL

!Define boundary conditions
FLST,2,14,1,ORDE,7
FITEM,2,1
FITEM,2,48
FITEM,2,88
FITEM,2,-92
FITEM,2,235
FITEM,2,275
FITEM,2,-280
/GO
D,P51X, ,0, , , ,ALL, , , , ,
FINISH

!Apply reference temperature (nonlinear)
/SOLU
ANTYPE,0
NLGEOM,1
NROPT,AUTO, ,
LUMPM,0
EQSLV,SPAR, ,0,
PREC,0
PIVCHECK,1
PSTRES,ON
TOFFST,0,
FLST,2,150,2,ORDE,2
FITEM,2,1
FITEM,2,-150
BFE,P51X,TEMP,1,-460, , ,
TIME,1
```

```
AUTOTS,-1
DELTIM,0.1, , ,1
KBC,0
TSRES,ERASE
TIME,1
AUTOTS,1
NSUBST,10,20,5,1
KBC,0
TSRES,ERASE
LNSRCH,1
SOLVE
finish

!Apply DC current force (nonlinear)
/SOLU
ANTYPE,0
NLGEOM,1
NROPT,AUTO, ,OFF
LUMPM,0
EQSLV,SPAR, ,0,
PREC,0
PIVCHECK,1
PSTRES,ON
TOFFST,0,
FLST,2,2,5,ORDE,2
FITEM,2,1
FITEM,2,3
/GO
SFA,P51X,1,PRES,-0.01          !apply
pressure on the supporting arms

FLST,2,1,5,ORDE,1
FITEM,2,2
/GO
SFA,P51X,1,PRES,-0.14          !apply
pressure on tip
TIME,1
AUTOTS,1
DELTIM,0.1, , ,1
KBC,0
TSRES,ERASE
TIME,1
AUTOTS,1
NSUBST,10,20,5,1
KBC,0
TSRES,ERASE
LNSRCH,1
solve
finish

!Modal analysis
/SOLU
ANTYPE,MODAL
UPCOORD,1.0,ON
PSTRES,ON
MODOPT,SUBSP,3
MXPAND,3
PSOLVE,TRIANG
PSOLVE,EIGFULL
FINISH
/SOLU
EXPASS,ON
PSOLVE,EIGEXP
FINISH
```